Study of random porous morphologies by means of statistical analysis and computer simulations of fluid dynamics

Kumulative Dissertation
zur Erlangung
des Doktorgrades der Naturwissenschaften
(Dr. rer. nat.)
des Fachbereichs Chemie
der Philipps-Universität Marburg

vorgelegt von

Artur Svidrytski, M.Sc.
aus Minsk, Belarus

Marburg an der Lahn, 2020

Die vorliegende Dissertation wurde von September 2016 bis Oktober 2020 am Fachbereich Chemie unter Leitung von Prof. Dr. Ulrich Tallarek angefertigt.

Vom Fachbereich Chemie
der Philipps-Universität Marburg (Hochschulkennziffer: 1180)
als Dissertation angenommen am

Erstgutachter: Prof. Dr. Ulrich Tallarek
Zweitgutachter: Prof. Dr. Matthias Thommes

Tag der Disputation: 11.12.2020

Abstract

This thesis presents an investigation of porous media by means of simulation techniques and morphological analysis. As a basis for the investigation throughout this work, we use three-dimensional (3D) images of porous structures obtained by imaging techniques, in particular, focused ion beam scanning electron microscopy (FIB-SEM) and confocal laser scanning microscopy (CLSM) for macroporous space, and scanning transmission electron microscopy (STEM) to resolve mesopores. A set of different morphological methods (chord length distribution (CLD), medial axis analysis (MAA), estimations of geometric, branch and diffusive tortuosities) are applied to capture averaged descriptors of the reconstructed porous samples. Because fluid dynamics is inherent in many applications of porous media, several techniques are deployed to simulate the fluid dynamics in the reconstructions of porous media. This work includes four chapters that cover three different topics associated with the investigation of fluid dynamics in porous media. Each chapter also represents a separate journal publication.

In the first chapter, we perform hydrodynamic dispersion simulations to study the morphology-flow relationship in physical reconstructions of particulate beds as well as in computer-generated packings of monosized spheres. A combination of lattice-Boltzmann and random-walk particle tracking (RWPT) methods were utilized to simulate the flow and mass transport, respectively. Based on mean chord length μ and standard deviation σ estimated for CLD, we present a morphological descriptor, σ/μ, that can predict the longitudinal dispersion coefficient for any morphological configuration of packed beds.

In the second chapter, we introduce the overall hindrance factor expression, $H(\lambda)$, that describes transport limitations in mesoporous space of random silica monoliths in dependence of λ, the ratio of solute size to mean pore size. The presented $H(\lambda)$ is obtained through diffusion simulations of finite-size tracers applying the RWPT technique in three reconstructions of morphologically similar porous silica. The expression can also be utilized to assess the hindered diffusion coefficient for any material with similar morphology.

In the third chapter, we adopt the lattice-gas mean field density functional theory (MFDFT) to virtually reproduce adsorption/desorption processes in a mesopore network of one of the monoliths from the second chapter. We demonstrate a good qualitative agreement of simulated boundary curves with experimental isotherms with an H2 hysteresis loop obtained for nitrogen at 77 K. We also use 3D images of the phase distribution that can be provided by MFDFT for any relative pressure value in the range $0 < p/p_0 \leq 1$ to reveal the relation between hysteresis and phase distribution.

In the fourth chapter, we continue using the concept of exploration of phase distribution and perform MFDFT modeling in physically reconstructed geometrical models of two ordered (SBA-15, KIT-6) and one random mesoporous silicas. We conduct a short parametric study of the MFDFT model to find optimal agreement with experimental isotherms in the hysteresis region.

We also present simulated boundary curves for both ordered structures with a clear H1 hysteresis loop and for the disordered material with type H2(a) hysteresis. The phase distribution analysis as well as the shape of scanning curves reveal a highly heterogeneous morphology of the random silica. Hence, pore blocking and cavitation phenomena are identified and analyzed.

Zusammenfassung

Diese Arbeit stellt eine Untersuchung poröser Medien mit Hilfe von Simulationstechniken und morphologischer Analyse vor. Als Grundlage für die Untersuchungen in dieser Arbeit verwenden wir dreidimensionale (3D-)Bilder poröser Strukturen, die mit bildgebenden Verfahren, insbesondere der fokussierten Ionenstrahl-Rasterelektronenmikroskopie und der konfokalen Lasermikroskopie für den makroporösen Raum und der Elektronenthomographie zur Auflösung von Mikro-Mesoporen gewonnen wurden. Eine Reihe verschiedener morphologischer Methoden (Sehnenlängenverteilung, Mittelachsenanalyse, Schätzungen von geometrischen, verzweigten und diffusiven Tortuositäten) werden angewandt, um gemittelte Deskriptoren der rekonstruierten porösen Proben zu erfassen. Da die Fluiddynamik in vielen Anwendungen poröser Medien inhärent ist, werden mehrere Techniken zur Simulation der Fluiddynamik in den Rekonstruktionen poröser Medien eingesetzt. Diese Arbeit umfasst vier Kapitel, die drei verschiedene Themen im Zusammenhang mit der Untersuchung der Fluiddynamik in porösen Medien behandeln. Jedes Kapitel stellt auch eine separate Publikation in wissenschaftlichen Fachzeitschriften dar.

Im ersten Kapitel führen wir hydrodynamische Dispersionssimulationen durch, um die Morphologie-Strömungs-Beziehung bei physikalischen Rekonstruktionen von Partikelbetten sowie bei computergenerierten Packungen von monodispersen Kugeln zu untersuchen. Eine Kombination von Lattice-Boltzmann- und Random-Walk-Particle-Tracking-Methoden (RWPT) wurde verwendet, um die Strömung und den Massentransport entsprechend zu simulieren. Basierend auf der für CLD geschätzten mittleren Sehnenlänge μ und der Standardabweichung σ präsentieren wir einen morphologischen Deskriptor, σ/μ, der den longitudinalen Dispersionskoeffizienten für jede morphologische Konfiguration von gepackten Betten vorhersagen kann.

Im zweiten Kapitel stellen wir den Ausdruck des Gesamthindernisfaktors $H(\lambda)$ vor, der die Transportbeschränkungen im mesoporösen Raum von ungeordneten Silika-Monolithen in Abhängigkeit von λ, dem Verhältnis der Größe des gelösten Stoffes zur mittleren Porengröße, beschreibt. Das vorgestellte $H(\lambda)$ wird durch Diffusionssimulationen von Tracern endlicher Größe unter Anwendung der RWPT-Technik in drei Rekonstruktionen morphologisch ähnlicher poröser Silika-Monolithen erhalten. Der Ausdruck kann auch zur Abschätzung des gehinderten Diffusionskoeffizienten für jedes Material mit ähnlicher Morphologie verwendet werden.

Im dritten Kapitel wenden wir die Lattice-Gas Mittelwertfeld-Dichtefunktionaltheorie (MFDFT) an, um Adsorptions-Desorptionsprozesse in einem Mesoporennetzwerk eines der Monolithen aus dem zweiten Kapitel zu reproduzieren. Wir zeigen eine gute qualitative Übereinstimmung der simulierten Randkurven mit experimentellen Isothermen mit einer H2-Hystereseschleife, die für Stickstoff bei $77\,\mathrm{K}$ erhalten wurde. Wir verwenden auch 3D-Bilder der Phasenverteilung, die von MFDFT für jeden Relativdruckwert im Bereich von $0 < p/p_0 \leq 1$ geliefert werden können, um die Beziehung zwischen Hysterese und Phasenverteilung aufzuzeigen.

Im vierten Kapitel fahren wir mit dem Konzept der Erforschung der Phasenverteilung fort

und führen die MFDFT-Modellierung in physikalisch rekonstruierten geometrischen Modellen von zwei geordneten (SBA-15, KIT-6) und einem ungeorndeten mesoporösen Silika-Material durch. Wir führen eine kurze parametrische Studie des MFDFT-Modells durch, um die optimalste Übereinstimmung mit experimentellen Isothermen im Hysteresebereich zu finden. Wir präsentieren auch simulierte Randkurven für beide geordneten Strukturen mit klarem Hystereseschleifentyp H1 und für das ungeordnete Material mit Hysterese vom Typ H2(a). Sowohl die Phasenverteilungsanalyse als auch die Form der scannenden Kurven zeigen eine sehr heterogene Morphologie des ungeordneten Silika-Materials. Daher werden Poreblocking- und Kavitationsphänomene identifiziert und analysiert.

Acknowledgments

This thesis would have never been possible without the support of numerous people.

First of all, I am sincerely grateful to my supervisor Prof. Dr. Ulrich Tallarek for his guidance, scientific and life advice, fruitful discussions, financial support and a very comfortable working environment that enabled my scientific and personal achievements throughout my Ph.D.

I am very thankful to Dr. Mikalai Yatskou, my ex-supervisor and later my colleague from the Faculty of Radiophysics and Computer Technologies of the Belarusian State University, who always believed in me and encouraged my scientific interest. I am deeply indebted to Dr. Viktor Skakun, the Head of the Department of System Analysis and Computer Simulation at the Faculty of Radiophysics and Computer Technologies of the Belarusian State University, who facilitated the realization of the opportunity to do my doctoral work.

I express my gratitude to Dr. Vasili Baranau for his unfailing willingness to help and his kind initiative to share his valuable scientific experience. I thank my colleague and my permanent co-author Dr. Dzmitry Hlushkou for sharing his knowledge and expertise in analysis of porous media as well as for all his help and refinements of my work during the preparation of our joint manuscripts.

I thank my co-authors Prof. Dr. Matthias Thommes and Prof. Dr. Peter A. Monson for the valuable contribution to our joint work. I thank Dr. Ashutosh Rathi and Dr. Daniel Schneider for introducing me to simulations of physisorption and sharing their program code.

I am thankful to my friends Dr. Christian Haas and Stephan-Johannes Reich, who also worked in the group of Prof. Dr. Tallarek, for uncountable friendly conversations and ability to raise my spirit any time needed. I thank all my colleagues for making the relaxed and amicable atmosphere in our group.

I express my gratitude to all my friends from Belarus and Germany for their support and our time together. I thank Magdalena Latka for numerous adventures and her great contribution to my life-work balance during my life in Marburg.

I am deeply indebted to my grandparents, Ludmila Svidrytskaya and Viktar Svidrytski, who always supported and inspired me during my whole life.

List of publications

First author

1. S.-J. REICH[§], A. SVIDRYTSKI[§], D. HLUSHKOU, D. STOECKEL, C. KÜBEL, A. HÖLTZEL and U. TALLAREK. Hindrance factor expression for diffusion in random mesoporous adsorbents obtained from pore-scale simulations in physical reconstructions. *Industrial & Engineering Chemistry Research*, 57.8: 3031–3042, 2018.
   DOI: 10.1021/acs.iecr.7b04840
2. A. SVIDRYTSKI, A. RATHI, D. HLUSHKOU, D.M. FORD, P.A. MONSON and U. TALLAREK. Morphology of fluids confined in physically reconstructed mesoporous silica: experiment and mean field density functional theory. *Langmuir*, 34.34: 9936–9945, 2018.
   DOI: 10.1021/acs.langmuir.8b01971
3. A. SVIDRYTSKI, D. HLUSHKOU and U. TALLAREK. Relationship between bed heterogeneity, chord length distribution, and longitudinal dispersion in particulate beds. *Journal of Chromatography A*, 1600: 167–173, 2019.
   DOI: 10.1016/j.chroma.2019.04.044
4. A. SVIDRYTSKI, D. HLUSHKOU, M. THOMMES, P.A. MONSON and U. TALLAREK. Modelling the impact of mesoporous silica microstructure on the adsorption hysteresis loop. *The Journal of Physical Chemistry C*, 124:39 21646–21655, 2020.
   DOI: 10.1021/acs.jpcc.0c07571

[§] S.-J.R. and A.S. contributed equally to this work.

Co-author

1. D. HLUSHKOU, A. SVIDRYTSKI and U. TALLAREK. Tracer-size-dependent pore space accessibility and long-time diffusion coefficient in amorphous, mesoporous silica. *The Journal of Physical Chemistry C*, 121.15: 8416–8426, 2017.
   DOI: 10.1021/acs.jpcc.7b00264
2. S.-J. REICH, A. SVIDRYTSKI, A. HÖLTZEL, J. FLOREK, F. KLEITZ, W. WANG, C. KÜBEL, D. HLUSHKOU and U. TALLAREK. Hindered diffusion in ordered mesoporous silicas: insights from pore-scale simulations in physical reconstructions of SBA-15 and KIT-6 silica. *The Journal of Physical Chemistry C*, 122.23: 12350–12361, 2018.
   DOI: 10.1021/acs.jpcc.8b03630
3. S.-J. REICH, A. SVIDRYTSKI, A. HÖLTZEL, W. WANG, C. KÜBEL, D. HLUSHKOU, and U. TALLAREK. Transport under confinement: Hindrance factors for diffusion in core-shell and fully porous particles with different mesopore space morphologies. *Microporous and Mesoporous Materials*, 282: 188–196, 2019.
   DOI: 10.1016/j.micromeso.2019.02.036
4. W. WANG, A. SVIDRYTSKI, D. WANG, A. VILLA, H. HAHN, U. TALLAREK and C. KÜBEL. Quantifying morphology and diffusion properties of mesoporous carbon from high-fidelity 3D reconstructions. *Microscopy and Microanalysis*, 25.4: 891–902, 2019.
   DOI: 10.1017/S1431927619014600
5. F. GRITTI, J. HOCHSTRASSER, A. SVIDRYTSKI, D. HLUSHKOU and U. TALLAREK. Morphology-transport relationships in liquid chromatography: Application to method development in size exclusion chromatography. *Journal of Chromatography A*, 1620: 460991, 2020.
   DOI: 10.1016/j.chroma.2020.460991
6. J. HOCHSTRASSER, A. SVIDRYTSKI, A. HÖLTZEL, T. PRIAMUSHKO, F. KLEITZ, W. WANG, C. KÜBEL and U. TALLAREK. Morphology-transport relationships for SBA-15 and KIT-6 ordered mesoporous silicas. *Physical Chemistry Chemical Physics*, 22.20: 11314–11326, 2020.
   DOI: 10.1039/D0CP01861A

Contents

Introduction

Porous structures with their functional properties play an important role in nature. Many objects in our surrounding have a porous basis in their structures, e.g., wood and bones.[1] Useful properties of porous structures were noticed by humans and, nowadays, have various scientific and engineering applications such as groundwater pollution, oil recovery, chromatographic separations, fluid filtration, drug discovery, drug distribution, battery electrodes, diffusion in biological tissues, vibration suppression, heterogeneous catalysis, heat insulation, sound absorption and many others.[2]

Packed beds and continuous beds, or monoliths, represent two fundamental architectures of macro- and mesoporous media. Packed beds comprise discrete macrosized mesoporous particles, with interparticle space that forms flow-through pores. The morphology of macroporous space in fixed beds is strongly related to how liquid passage occurs in packings. Flow can be characterized by hydraulic permeability residence time distributions of solute molecules.[3] Highly dense and mechanically stable packings of spherical particles can only exist with a porosity in a range from around 0.36 to ca. 0.46. Another possible architecture for porous media, continuous beds, is represented by a monolithic skeleton with interstitial macropores and intraskeleton mesopores.[4] On all levels of pore hierarchy, monoliths enjoy more morphological variability than conventional packed beds, what, theoretically, brings more flexibility to their synthesis and enables to obtain a structure that will comply with the required specific surface area, heat and mass transfer characteristics, mobile phase velocity, separation selectivity and other parameters. But, practically, the relationships between synthesis parameters and output properties of porous media often remain vague.[5] Macroporosity of continuous beds is also usually higher than in particulate beds and can take on values from 0.5 to 0.75. However, deviation from this values to both lower and higher porosities is possible. Moreover, the size of macropores in continuous beds is independent from the skeleton thickness. This allows a precise adjustment of the internal surface area and mesopore volume, thus controlling the throughput or storage capacity of the porous system.[5]

Another property that porous materials can enjoy is a porous hierarchy. It provides a large surface area and thus hierarchically porous materials play an important role in chemical and physical processes related to mass storage, catalysis, chemical separation, energy applications, i.e., all processes that need a well connected pore network for molecule transport enabling an easy access to the active sites. The pore hierarchy comprises a network of larger macropores

[1] L. J. Gibson and M. F. Ashby. *Cellular Solids: Structure and Properties*. Cambridge University Press, July 22, 1999. 536 pp.
[2] P. S. Liu and K. M. Liang. *J. Mater. Sci.*, 36, 5059–5072, 2001.
[3] F. Gritti et al. *J. Chromatogr. A*, 1620, 460991, 2020.
[4] E. S. P. Bouvier. “Chromatography: Liquid | Monolithic Columns” in: *Encyclopedia of Separation Science* ed. by I. D. Wilson. Oxford: Academic Press, Jan. 1, 2007. 1–7
[5] D. Enke, R. Gläser, and U. Tallarek. *Chem.-Ing.-Tech.*, 88, 1561–1585, 2016.

with $\mu\mathrm{m}$ to mm pore size and a network of smaller meso-micropores ($2\,\mathrm{nm}-50\,\mathrm{nm}$ and < 2, respectively). The larger network comprises flow-through pores, in which flow, i.e., percolation of a mobile phase under an external force, serves as a main process. The meso- and microporous network makes an essential contribution to the surface area, thus improving performance of porous media for the corresponding applications. Importantly, an access to these pores for solute molecules is possible only via diffusion. Thus we see that a proper construction of porous systems with improved morphology that meets requirements of each concrete application is a challenging task for research groups that deal with material synthesis.[5]

Since efficient mass transfer has a strong dependency on the topological and surface shape peculiarities of the porous structure, morphology serves as a crucial factor when improving the performance of porous systems. Therefore, the discovery of proper descriptors that allow an accurate characterization of porous materials also facilitates the identification of morphology-transport relationships. And in its turn the understanding of these relationships can help to design optimized porous systems with desired transport properties tailored to a certain application.[5,6] Because a pore of less than mm length scale cannot be discerned by sight, straightforward characterization becomes problematic. Indirect methods, e.g., physical adsorption, mercury porosimetry and others, were developed to give us a generalized insight into the morphology of porous materials. Theses methods offer us an averaged representation of the structure and cannot always suggest an unequivocal answer regarding the pore network topology. Even indicating some transport limiting cases like numerous bottlenecks or clusters of dead-end pores can be challenging for such approaches as well.[7] Actually, these techniques work according to principles of a black box analysis. Analyzing interrelationships between input conditions and output results the scientist tries to guess the system arrangement. The downside of a black box analysis is that comprehension and discovery of new physical aspects can lead in the best case to a specification, and in the worst case to crucial changes of the analysis methodology. Indeed, e.g., physical adsorption analysis comes in use while it experiences continuous improvements and refinements[8–10] while new scientific results based on the method are being published.[11–13]

Emergence of physical reconstruction techniques is a major breakthrough for porous media analysis that has an enormous potential for material science in general. These techniques make it possible to represent a porous structure at a multipore level over hundreds and thousands

[6] K. Hormann et al. *New J. Chem.*, 40, 4187–4199, 2016.
[7] S.-J. Reich et al. *J. Phys. Chem. C*, 122, 12350–12361, 2018.
[8] R. Cimino et al. *Colloid Surface A*, 437, 76–89, 2013.
[9] D. Schneider, D. Kondrashova, and R. Valiullin. *Sci. Rep.*, 7, 7216, 2017.
[10] H. R.N. B. Enninful et al. *Micropor. Mesopor. Mat.*, 309, 110534, 2020.
[11] A. Svidrytski et al. *J. Phys. Chem. C*, 124, 21646–21655, 2020.
[12] G. Sdanghi et al. *J. Carbon Res.*, 6, 46, 2020.
[13] R. Guillet-Nicolas et al. *J. Colloid Interface Sci.*, 579, 489–507, 2020.

of pores as a three-dimensional (3D) virtual image.[14–19] Imaging techniques like focused ion beam scanning electron microscopy (FIB-SEM) and confocal laser scanning microscopy (CLSM) enable to resolve the macropore scale.[14,20–22] Another technique, scanning transmission electron microscopy (STEM), serves as a method to capture mesopores.[23]

Physical reconstruction of porous media enjoys three major advantages. The most straightforward one is direct depiction of morphology that handles the problem of indirect methods, i.e., the morphology can be assessed visually, what immediately answers the question if the synthesized structure meets initial morphological requirements and has any undesired and crucial visual imperfections.[7,21,24–27]

Second, the spatially resolved structural heterogeneity also gives the possibility not only to calculate basic measures of porous media like porosity or specific surface area, but also to introduce new methods, such as Voronoi tesselation, medial axis approach (MAA), geometric and branch tortuosities, chord length distribution (CLD) and others, that provide complementary structural descriptors and permit to distinguish visually similar structures, which show different mass transfer performance.[6,24,28–30]

Computer modeling in physical reconstructions is the third major advantage. Numerical simulations of diffusion, flow, physical adsorption and other physical and/or chemical processes in reconstructed porous structures can serve as a very powerful tool that helps the researcher to determine performance-limiting morphological properties of porous media. Computer modeling coupled with high-performance computational facilities makes it possible to easily vary experiment conditions to investigate outcomes of a studied porous system over a wide range of relevant parameters. Moreover, it is also possible to take snapshots at any time of the simulation process and compare the state of the mobile phase.[11,28,31,32]

This thesis addresses three different topics, but all of them are associated with the study of porous media employing simulations of fluid dynamics and morphological analysis. The study

[14] D. Stoeckel et al. *Langmuir*, 30, 9022–9027, 2014.
[15] S. Mitchell et al. *Nat. Commun.*, 6, 8633, 2015.
[16] J. Berthonneau et al. *Proc. Natl. Acad. Sci. U. S. A.*, 115, 12365–12370, 2018.
[17] Y. Yao et al. *Langmuir*, 22, 11148–11157, 2006.
[18] R. Leary, P. A. Midgley, and J. M. Thomas. *Acc. Chem. Res.*, 45, 1782–1791, 2012.
[19] J. Zečević, K. P. de Jong, and P. E. de Jongh. *Curr. Opin. Solid St. M.*, 17, 115–125, 2013.
[20] S. Bruns et al. *J. Chromatogr. A*, 1218, 5187–5194, 2011.
[21] S. Bruns et al. *J. Chromatogr. A*, 1268, 53–63, 2012.
[22] D. Stoeckel et al. *Langmuir*, 31, 7391–7400, 2015.
[23] W. Wang et al. *Microsc. Microanal.*, 25, 891–902, 2019.
[24] S.-J. Reich et al. *Ind. Eng. Chem. Res.*, 57, 3031–3042, 2018.
[25] S.-J. Reich et al. *Micropor. Mesopor. Mat.*, 282, 188–196, 2019.
[26] J. Hochstrasser et al. *Phys. Chem. Chem. Phys.*, 22, 11314–11326, 2020.
[27] A. E. Reising et al. *J. Chromatogr. A*, 1504, 71–82, 2017.
[28] T. Müllner, K. K. Unger, and U. Tallarek. *New J. Chem.*, 40, 3993–4015, 2016.
[29] H. Liasneuski et al. *J. Appl. Phys.*, 116, 034904, 2014.
[30] S. Khirevich et al. *J. Chromatogr. A*, 1217, 4713–4722, 2010.
[31] P. Levitz. *Cem. Concr. Res.*, 37, 351–359, 2007.
[32] B. Coasne. *New J. Chem.*, 40, 4078–4094, 2016.

encompasses

- research of the morphology-flow relationship in reconstructed and computer-generated macroporous space of particulate beds,
- investigation of hindered diffusion and morphology in reconstructed mesoporous networks of silica monoliths and
- analysis of the liquid distribution and physical phenomena related to capillary condensation in mesopores of silica materials during physical adsorption and desorption.

The whole research was based on the concept of numerical simulations of physical processes in physically reconstructed porous media. Essential advantage of this work consists in the usage of realistic structures instead of simplified models that, actually, cannot always sufficiently imitate important morphological peculiarities of real intricate porous networks.[11,33,34]

The following three sections of this introduction will briefly cover each of the above itemized topics in the corresponding order.

Morphology-flow relationship in macroporous space of particulate beds

Mass transfer is inseparable from processes such as adsorption, separation and catalysis. Therefore, the targeted performance optimization of porous materials requires also a detailed knowledge about relevant transport properties, e.g., longitudinal dispersion coefficient D_{L}, and transport limitations.[35,36] The morphology of the materials has a huge influence on transport and, therefore, the possibility to accurately characterize the structure can enable the assessment of transport capabilities of the studied materials. However, the discovery of proper morphological descriptors for porous media appears to be a challenge for material scientists and represents one of the major problems of this field.[37–39]

Successful results were obtained applying Voronoi tessellation to computer-generated bulk and cylindrically-confined packings of monosized hard spheres.[30,40,41] It has been shown that the tessellation approach can also be employed for polydisperse disks and spheres as well as

[33] D. Hlushkou, A. Svidrytski, and U. Tallarek. *J. Phys. Chem. C*, 121, 8416–8426, 2017.
[34] A. Svidrytski et al. *Langmuir*, 34, 9936–9945, 2018.
[35] F. Gritti and G. Guiochon. *J. Chromatogr. A*, 1221, 2–40, 2012.
[36] F. Gritti and G. Guiochon. *Anal. Chem.*, 85, 3017–3035, 2013.
[37] Torquato and Haslach. *Appl. Mech. Rev.*, 55, B62–B63, 2002.
[38] G. Guiochon, A. Felinger, and D. G. G. Shirazi. *Fundamentals of Preparative and Nonlinear Chromatography*. 2nd ed. Academic Press, 2006.
[39] J. Kärger, D. M. Ruthven, and D. N. Theodorou. *Diffusion in Nanoporous Materials, 2 Volume Set*. John Wiley & Sons, 2012. 932 pp.
[40] A. Okabe et al. "Spatial Tessellations: Concepts and Applications of Voronoi Diagrams" in: *Int. Encycl. Geogr. People, Earth, Environ. Technol.* Chichester, England: John Wiley & Sons Ltd., 2000. 1–11
[41] S. Khirevich et al. *J. Chromatogr. A*, 1262, 77–91, 2012.

for objects with irregular shapes .[42–45] However, the analysis of physically reconstructed chromatographic columns has revealed the existence of packing defects such as particle debris and oligomers, contaminations and large voids between particles.[21,27] Unpredictable irregular shapes, an unknown number as well as the spatial distribution of these defects in particulate beds cause a significant computational challenge for the application of tessellation approaches to such structural configurations.

This restriction on the spatial tessellation approach induced us to find another method that could relate both morphology and mass transfer, namely, effective longitudinal dispersion D_{L} in physical reconstructions of packed beds. This method had to be independent of any shape and size assumptions of the solid, liquid or gas phase. Chord length distribution (CLD) analysis that was already used earlier for morphological investigations of silica-based[20,22,46] and organic-polymer monoliths[47,48] enjoys these qualities.

To implement CLD analysis, a chosen phase, the interparticle pore space of a packing in our case, obtains assigned seed points that are distributed in either a random or predefined manner. Then, from each seed location, straight chords are released to different directions, so that each chord represents a straight line segment, which measures the distance between two opposite interfaces. Next, the lengths of all chords in the structure are assembled into a CLD that is fitted with a probability density function (PSD) of two-parameter *k*-Gamma distribution

$$f\left(l_{\mathrm{c}}\right)=\frac{k^{k}}{\Gamma(k)}\frac{l_{\mathrm{c}}^{k-1}}{\mu^{k}}\exp\left(-k\frac{l_{\mathrm{c}}}{\mu}\right) \tag{1}$$

where l_{c} is chord length, μ_{c} denotes the mean chord length, and k is a shape parameter.

The greater part of chords released from one point probes the morphology of their local pore. Therefore, the distribution shape within the interquartile range (IQR) represents an averaged pore configuration throughout the structure. A minor number of chords that form tails of the PSD hit also interfaces of adjacent pores and thus the CLD discovers information about short-range heterogeneities of a studied structure.[28]

In Chapter 1, we demonstrate, as an alternative to Voronoi tessellation, an application of CLD analysis to physical reconstructions of chromatographic packings and search for a relationship between statistical parameters of CLD and dispersion coefficients, D_{L}. The particulate beds, namely their bulk regions, were reconstructed by means of CLSM and FIB-SEM.[21,27] Values of longitudinal dispersion D_{L} were obtained by the combination of the lattice–Boltzmann method (LBM) that serves for the preparation of the fluid flow velocity map, and a random-walk particle

[42] N. N. Medvedev et al. *J. Comput. Chem.*, 27, 1676–1692, 2006.
[43] K. Lochmann, L. Oger, and D. Stoyan. *Solid State Sci.*, 8, 1397–1413, 2006.
[44] M. Danisch, Y. Jin, and H. A. Makse. *Phys. Rev. E*, 81, 051303, 2010.
[45] F. M. Schaller et al. *Philos. Mag.*, 93, 3993–4017, 2013.
[46] K. Hormann and U. Tallarek. *J. Chromatogr. A*, 1312, 26–36, 2013.
[47] T. Müllner et al. *Adv. Mater.*, 27, 6009–6013, 2015.
[48] T. Müllner et al. *Langmuir*, 33, 2205–2214, 2017.

tracking (RWPT) technique to simulate diffusive motion of point-like tracers. Adsorption of tracers on the solid interface was neglected. Additionally to physically reconstructed packings, we have also extended the analyzed data set by monosized computer-generated packings with various porosities and four different heterogeneity protocols published in Khirevich et al.[30]

Investigation of continuous beds: hindered diffusion and morphological analysis

Sizes of solute molecules diffusing through a porous structure are often similar to dimensions of pore network branches.[49–55] Whereas some processes, e.g., filtration, benefit from the hindrance, performance of heterogeneous catalysis and chemical separations is directly proportional to the size of an accessible area of solid phase. Moreover, if interfacial kinetics occurs fast, hindered diffusion of solutes becomes a main actor and has a crucial impact on the productivity of the chemical system.

Knowledge about the dependency of the global diffusive hindrance on morphology gives a possibility to control process performance in agreement with the application of the confining porous medium. The definition of the global diffusive hindrance factor $H(\lambda)$ is

$$H(\lambda) = \frac{D_{\mathrm{eff,H}}(\lambda)}{D_{\mathrm{m}}} \tag{2}$$

whereby λ represents the degree of confinement and is defined as the ratio between solute molecule or particle size (in the following referred to as tracers) and averaged pore size. $D_{\mathrm{eff,H}}(\lambda)$ is the effective diffusion coefficient of the tracer that diffuse through the confining medium and thus the coefficient has a direct relationship with the morphology of the porous medium.[56,57] D_{m} is the molecular diffusion coefficient of the tracer in the bulk space.

A lot of work was done to define the diffusive hindrance factor. Some expressions for simple geometrical shapes like slit pores or cylinders are readily present in publications and reviewed in the work of Dechadilok and Deen.[58] The pioneering Renkin equation that was the basis for further evolution of the hindrance factor expression was obtained as a solution for the case of spherically shaped tracer falling in a liquid-filled pipe. Simplicity of this model also consists in the assumption of a constant drag coefficient over the pore cross-section as well as along the

[49] J. Kärger and D. M. Ruthven. *New J. Chem.*, 40, 4027–4048, 2016.
[50] A. T. Florence. *J. Control. Release*, 164, 115–124, 2012.
[51] Y. S. Polyakov and A. L. Zydney. *J. Memb. Sci.*, 434, 106–120, 2013.
[52] H. Al-Obaidi and A. T. Florence. *J. Drug Deliv. Sci. Technol.*, 30, 266–277, 2015.
[53] C. Sievers et al. *ACS Catal.*, 6, 8286–8307, 2016.
[54] J. M. Angelo and A. M. Lenhoff. *J. Chromatogr. A*, 1440, 94–104, 2016.
[55] V. I. Syngouna and C. V. Chrysikopoulos. *Sci. Total Environ.*, 545-546, 210–218, 2016.
[56] M. J. Skaug et al. *ACS Nano*, 9, 2148–2156, 2015.
[57] F. Babayekhorasani et al. *Soft Matter*, 12, 8407–8416, 2016.
[58] P. Dechadilok and W. M. Deen. *Ind. Eng. Chem. Res.*, 45, 6953–6959, 2006.

pore axis. The Renkin equation determines the dependency of the diffusion coefficient value on steric interactions and works out very well for the experimental conditions that correspond to Renkins simplification with degree of confinement less than 0.4, i.e., $\lambda \leq 0.4$.[59,60]. It follows that

$$H(\lambda) = \Phi(\lambda)K_{\mathrm{d}}(\lambda) = (1-\lambda)^2(1 - 2.104\lambda + 2.09\lambda^3 - 0.95\lambda^5) \tag{3}$$

The first term $\Phi(\lambda) = (1-\lambda)^2$ is the equilibrium partitioning coefficient, which is the cross-sectional average tracer concentration at either pore end divided by the adjacent external particle concentration for purely steric hindrances between tracer and pore. The second term $K_{\mathrm{d}}(\lambda) = D_{\mathrm{eff,K}}(\lambda)/D_{\mathrm{m}}$ represents the local hindrance factor that comprises hydrodynamic drag, which is experienced by the tracer while it diffuses in the cylindrical pore.

Afterwards, the Renkin model gained several modifications,[58,61,62] but it still represents the physics in a single pore of constant cross-section. Accessible porosity and diffusive tortousity of porous media obviously play an important role if we consider hindered diffusion in a random pore network. Therefore, another research was done that combined the Renkin equation with a semi-empirical polynomial expression describing the evolution of the pore network morphology with increasing λ.[63]

For lack of better approach, all these simplified models were also used to estimate hindrance diffusion for complex porous systems. However, various experimental researches on mass transfer[56,57,64–70] have shown a more intricate nature of diffusion in a real porous structure with a random pore network. Therefore, a more advanced model based on a random pore network is still demanded.

The availability of imaging techniques in conjunction with the possibility to simulate diffusion in 3D images makes this problem manageable. Several works have already recently demonstrated that both the Renkin equation and the equation of Deen and Dechadilok can significantly overestimate hindered diffusion and, for this reason, the equations are not suitable for an accurate analysis with respect to real porous structures. Moreover, the authors have shown that the effective topological and geometrical properties of a pore network display an individual dependency on lambda[7,24–26] and, for this moment, general patterns of the relation remain vague

[59] R. H. Li, D. H. Altreuter, and F. T. Gentile. *Biotechnol. Bioeng.*, 50, 365–373, 1996.
[60] E. M. Renkin. *J. Gen. Physiol.*, 38, 225–243, 1954.
[61] P. M. Bungay and H. Brenner. *Int. J. Multiph. Flow*, 1, 25–56, 1973.
[62] W. M. Deen. *AIChE J.*, 33, 1409–1425, 1987.
[63] V. Wernert, R. Bouchet, and R. Denoyel. *Anal. Chem.*, 82, 2668–2679, 2010.
[64] J. Kärger and R. Valiullin. *Chem. Soc. Rev.*, 42, 4172–4197, 2013.
[65] T. Titze et al. *Angew. Chemie Int. Edit.*, 54, 14580–14583, 2015.
[66] A. Galarneau et al. *J. Phys. Chem. C*, 120, 1562–1569, 2016.
[67] F. Elwinger, P. Pourmand, and I. Furó. *J. Phys. Chem. C*, 121, 13757–13764, 2017.
[68] J. Kärger et al. *Chem.-Ing.-Tech.*, 82, 779–804, 2010.
[69] J. Kärger et al. *Nat. Mater.*, 13, 333–343, 2014.
[70] M. J. Skaug and D. K. Schwartz. *Ind. Eng. Chem. Res.*, 54, 4414–4419, 2015.

and have still to be studied.

Chapter 2 makes a further step in disclosing the nature of hindered diffusion in disordered mesoporous networks of continuous beds. In particular, it provides a hindrance factor expression as well as a quantitative morphological characterization for three random mesoporous samples from the mesoporous skeleton of hierarchically-structured macro-mesoporeous silica monoliths that are often utilized for separation, heterogeneous catalysis, storage and other important processes.[5,71–73] The reconstructions were performed with the STEM technique. Diffusion simulations in reconstructed silica were conducted using the RWPT technique.

Physical adsorption: experiment and simulation

Significant progress has been achieved in recent years in the synthesis of materials with hierarchical pore systems, tailored pore size and structure, as well as controlled surface functionality for applications related to engineering (chemical separation, heterogeneous catalysis), energy (supercapacitors, batteries, fuel cells), environment (desalination, nuclear waste storage, water remediation), and medicine (oral drug delivery).[32,71,74–90] Importantly, the morphological and functional properties of these materials are basically determined by the geometry and topology of their pore networks. Thus, a comprehensive morphological characterization is essential to any optimization strategies for these materials. As a consequence, along with efforts focused on the development of new materials, many investigations were dedicated to the understanding and characterization of the underlying pore structures. Experimental techniques utilized for this purpose include gas adsorption, small angle X-ray and neutron scattering, mercury porosimetry, scanning and transmission electron microscopy, thermoporometry, and NMR-based methods.[91] Each technique has a limited length scale of applicability for pore size analysis. Among these, gas adsorption measurements are widely used to assess the pore size distribution, internal sur-

[71] K. K. Unger, R. Skudas, and M. M. Schulte. *J. Chromatogr. A*, 1184, 393–415, 2008.
[72] A. Galarneau et al. *Comptes Rendus Chim.*, 19, 231–247, 2016.
[73] E. Aznar et al. *Chem. Rev.*, 116, 561–718, 2016.
[74] F. Gritti and G. Guiochon. *J. Chromatogr. A*, 1228, 2–19, 2012.
[75] J. Zhang and C. Ming Li. *Chem. Soc. Rev.*, 41, 7016–7031, 2012.
[76] D. I. Fried, F. J. Brieler, and M. Fröba. *ChemCatChem*, 5, 862–884, 2013.
[77] S. Lwin and I. E. Wachs. *ACS Catal.*, 4, 2505–2520, 2014.
[78] L. Vilcocq et al. *ChemSusChem*, 7, 1010–1019, 2014.
[79] R. Munirathinam, J. Huskens, and W. Verboom. *Adv. Synth. Catal.*, 357, 1093–1123, 2015.
[80] D. J. Wales et al. *Chem. Soc. Rev.*, 44, 4290–4321, 2015.
[81] W. J. Roth et al. *Chem. Soc. Rev.*, 45, 3400–3438, 2016.
[82] R. Millini and G. Bellussi. *Catal. Sci. Technol.*, 6, 2502–2527, 2016.
[83] K. Ganesan et al. *Mater. Des.*, 92, 345–355, 2016.
[84] M. Hartmann and W. Schwieger. *Chem. Soc. Rev.*, 45, 3311–3312, 2016.
[85] K. Zhang and M. L. Ostraat. *Catal. Today*, 264, 3–15, 2016.
[86] L. Xu and P. Wu. *New J. Chem.*, 40, 3968–3981, 2016.
[87] J. Florek, R. Caillard, and F. Kleitz. *Nanoscale*, 9, 15252–15277, 2017.
[88] D. M. Schlipf et al. *Adv. Mater. Interfaces*, 4, 1601103, 2017.
[89] R. Diab et al. *Adv. Colloid Interface Sci.*, 249, 346–362, 2017.
[90] H. Singh and R. S. Myong. *Adv. Mater. Sci. Eng.*, 9565240, 2018.
[91] J. Rouquerol et al. *Pure Appl. Chem.*, 66, 1739–1758, 1994.

face area, and to some extent the architecture of the pore network. This experimental approach is popular, as it allows assessing a wide range of pore sizes including the complete range of micropores ($<2\,\mathrm{nm}$) and mesopores ($2\,\mathrm{nm}-50\,\mathrm{nm}$).[92] In addition, this technique is convenient to use, non-destructive, and not that cost intensive compared to some of the above-mentioned methods.[93,94]

An important aspect in the interpretation of gas sorption experiments is the hysteresis between adsorption and desorption isotherms, associated with the filling and emptying of the mesopores by capillary condensation and evaporation, respectively. The pressure at which capillary condensation is observed can be larger than that at which capillary evaporation takes place.[95] This hysteresis effect depends on the pore geometry and temperature and would be closely concerned with the mechanisms of capillary condensation and evaporation.[96–99]

The first explanation for hysteresis in a cylindrical pore open at both ends was proposed by Foster in 1932.[100] He showed that the conception of capillary condensation as a secondary process, following layer adsorption, provides a simple explanation for hysteresis observed in such a pore. It was suggested that the lack of reversibility is due to a delay in the formation of the meniscus during the addition of vapor to the system. It is now well recognized that pore imperfections, such as corrugation or a variation of the pore width along the pore axis, can strongly affect hysteresis.[98,101–103] Particularly, in pores with ink-bottle configuration, pore-blocking and cavitation mechanisms of desorption can be observed.

The relationship between the shape of the hysteresis loop and the 3D pore network morphology of a material is even more complex. In addition to effects observed on the scale of individual pores, there are also effects that take place on the scale of the pore network. A classical scenario of capillary condensation[100] implies that the vapor–liquid transition is delayed due to the existence of metastable adsorption films and hindered nucleation of liquid bridges. In an open pore filled with liquid-like condensate, the vapor–liquid interface is already present and evaporation/desorption occurs without nucleation via a receding meniscus.[93] This desorption mechanism is associated with the equilibrium vapor–liquid transition[104,105] and is dominant in ordered mesoporous materials with mainly uniform cylindrical pores and ordered 3D pore

[92] M. Thommes et al. *Pure Appl. Chem.*, 87, 1051–1069, 2015.
[93] K. A. Cychosz et al. *Chem. Soc. Rev.*, 46, 389–414, 2017.
[94] J. Rouquerol et al. *Adsorption by Powders and Porous Solids: Principles, Methodology and Applications*. Academic Press, Sept. 6, 2013. 647 pp.
[95] S. J. Gregg, K. S. W. Sing, and H. W. Salzberg. *J. Electrochem. Soc.*, 114, 279C, 1967.
[96] T. Horikawa, D. D. Do, and D. Nicholson. *Adv. Colloid Interface Sci.*, 169, 40–58, 2011.
[97] B. Coasne et al. *Chem. Soc. Rev.*, 42, 4141–4171, 2013.
[98] K. Morishige. *Langmuir*, 29, 11915–11923, 2013.
[99] J. Li et al. *Mol. Simul.*, 42, 1–8, 2016.
[100] A. G. Foster. *Trans. Faraday Soc.*, 28, 645, 1932.
[101] B. Coasne, K. E. Gubbins, and R. J.-M. Pellenq. *Phys. Rev. B*, 72, 024304, 2005.
[102] K. Morishige. *J. Phys. Chem. C*, 121, 5099–5107, 2017.
[103] N. Klomkliang, D. D. Do, and D. Nicholson. *Chem. Eng. J.*, 239, 274–283, 2014.
[104] J. Landers, G. Y. Gor, and A. V. Neimark. *Colloid Surface A*, 437, 3–32, 2013.
[105] P. A. Monson. *Langmuir*, 24, 12295–12302, 2008.

networks.[106]

In more complex pore architectures, as in networks with ink-bottle pores, evaporation is also delayed. As a consequence, the wider body of the pore remains filled until the neck evaporates at lower vapor pressure (pore-blocking effect). Thus, the pore-blocking induced evaporation represents a percolation transition. Therefore, for some disordered materials, the desorption branch of the hysteresis loop can be significantly steeper than the adsorption branch. In this case, the confined liquid evaporates from the pore system (or part of it) when the liquid from the largest neck evaporates.

A similar hysteresis loop is also observed when the size distribution of the pore cavities is relatively wide compared to the distribution of the neck sizes. Several studies using model materials containing well-defined ink-bottle pores revealed that if the pore neck diameter is smaller than a certain critical size (for a given temperature and adsorptive), then desorption occurs via cavitation, or, spontaneous nucleation of a bubble in the pore.[107–114] In this case, the pore body empties, while the pore neck remains filled. For nitrogen and argon adsorption at $77\,\mathrm{K}$ and $87\,\mathrm{K}$, respectively, the critical neck size is $5\,\mathrm{nm}-6\,\mathrm{nm}$.[109,110,113] Hence, for a given temperature and adsorptive, the neck size dictates the desorption mechanism. Correspondingly, by varying the neck size or entrances to the main pore system, one should be able to observe a transition from cavitation induced evaporation to pore blocking.

Developments in theoretical and numerical models in recent years enable to better comprehend the physics of fluid dynamics in porous materials and, consequently, to facilitate the targeted optimization of porous materials.[10,32,104,115–120] Mesoporous space in porous media is conventionally described by physisorption analysis and characteristics extracted from adsorption/desorption isotherms.[93,121] However until now, physisorption analysis cannot provide any morphological descriptors for random mesoporous silica that could quantitatively relate morphology and transport. Therefore, relationships between physisorption isotherms, pore structure and effective diffusivity stay a relevant issue for scientists.

The lattice-gas MFDFT numerical model for the modeling of physical adsorption has been

[106] K. Morishige and N. Tarui. *J. Phys. Chem. C*, 111, 280–285, 2007.
[107] H.-J. Woo, L. Sarkisov, and P. A. Monson. *Langmuir*, 17, 7472–7475, 2001.
[108] L. Sarkisov and P. A. Monson. *Langmuir*, 17, 7600–7604, 2001.
[109] P. I. Ravikovitch and A. V. Neimark. *Langmuir*, 18, 1550–1560, 2002.
[110] P. I. Ravikovitch and A. V. Neimark. *Langmuir*, 18, 9830–9837, 2002.
[111] A. Vishnyakov and A. V. Neimark. *Langmuir*, 19, 3240–3247, 2003.
[112] B. Libby and P. A. Monson. *Langmuir*, 20, 4289–4294, 2004.
[113] M. Thommes et al. *Langmuir*, 22, 756–764, 2006.
[114] K. Morishige et al. *Langmuir*, 22, 9220–9224, 2006.
[115] R. Evans. *J. Phys.: Condens. Mat.*, 2, 8989–9007, 1990.
[116] L. D. Gelb et al. *Reports Prog. Phys.*, 62, 1573–1659, 1999.
[117] A. V. Neimark, P. I. Ravikovitch, and A. Vishnyakov. *J. Phys.: Condens. Mat.*, 15, 347–365, 2003.
[118] P. A. Monson. *Micropor. Mesopor. Mat.*, 160, 47–66, 2012.
[119] J. D. Evans et al. *Chem. Mater.*, 29, 199–212, 2017.
[120] W. P. Krekelberg et al. *J. Phys. Chem. C*, 121, 16316–16327, 2017.
[121] M. Thommes et al. *J. Chromatogr. A*, 1191, 57–66, 2008.

widely used in recent years to simulate fluid dynamics and fluid distribution in simplified pore networks like connected chains of cylinders with varying width or computer-generated porous structures, e.g., Vycor glass.[10,118,122] A step forward is to combine the MFDFT model with a 3D physical reconstruction of mesoporous space, which, in turn, can enable to delve into the virtual structure and to gain a detailed picture about the morphological particularities related to the shape of adsorption/desorption isotherms.[18,123,124]

In Chapter 3, we present an unprecedented step forward for physisorption analysis, applying the MFDFT approach to a physical reconstruction of a mesoporous silica sample from a hierarchical silica monolith. We simulated isotherms with type H2 hysteresis that exhibit good qualitative agreement with experimental curves (nitrogen, 77 K) for the same material. 3D maps with liquid and gas phase distributions that come as an output of MFDFT calculations were used to study the liquid arrangement comparing meta- and equilibrium states for both fixed pressure and fixed density in the hysteresis region. The good agreement between experiment and simulation also served as a validation for correctness of the chosen MFDFT parameters, i.e., temperature and fluid-wall interaction, which allowed to safely expand conclusions obtained from the virtual analysis to the physical world. Chapter 4 presents an extension of the research on the relationships between the shape of the hysteresis loop and the local pore morphology of porous media employing results from physisorption simulations in reconstructions of two ordered silicas, SBA-15 and KIT-6, and one random silica from the mesoporous shell of a solid core–porous shell particle.

[122] S. Naumov et al. *Phys. Rev. E*, 78, 060601, 2008.
[123] Z. Liu et al. *Microscopy*, 62, 109–146, 2013.
[124] D. S. Su, B. Zhang, and R. Schlögl. *Chem. Rev.*, 115, 2818–2882, 2015.

Chapter 1

Relationship between bed heterogeneity, chord length distribution, and longitudinal dispersion in particulate beds

Authors:

Artur Svidrytski, Dzmitry Hlushkou and Ulrich Tallarek*

State of publication:

Published on August 30, 2019 in Journal of Chromatography A, Vol. 1600, pp 167–173
DOI: 10.1016/j.chroma.2019.04.044

Abstract We analyse a relationship between the bulk microstructure of randomly packed beds, which we quantify through chord length distribution (CLD) analysis of the interparticle void space, and the associated flow heterogeneity, as expressed by the longitudinal dispersion coefficient at a Péclet number of $Pe = 10$. A random collection of physically reconstructed packings is complemented with a systematic set of computer-generated packings of monosized spheres, for which the packing-generation algorithm has been carefully adjusted to realize a monotonic variation of the bed porosity and microstructural heterogeneity. The most relevant difference in the morphology between these computer-generated and the physically reconstructed packings are structural defects present in the real packings, such as particle oligomers and larger voids as well as contaminations and particle debris. These defects influence the pore space morphology and introduce additional structural heterogeneity. Hydrodynamic dispersion coefficients for all packings are derived by implementing the lattice-Boltzmann method to simulate fluid flow and a random-walk particle tracking technique to record the transport of passive, point-like tracers in the flow fields. We propose a morphological descriptor, σ/μ, based on statistical parameters of a CLD (standard deviation σ and mean chord length μ) that can be used to predict the dispersion coefficient in packed beds, independent from the underlying particle size distribution, packing-generation protocol, bed porosity, and the occurrence of structural defects.

1.1 Introduction

The discovery of quantitative relationships between morphological properties of microscopically disordered porous materials (like randomly packed beds of spherical particles in liquid chromatography) and relevant fluid as well as solute transport properties, such as the longitudinal dispersion coefficient D_L (and plate height H_L in liquid chromatography), belong to major challenges in materials science.[37–39] Many processes in adsorption, separation, and catalysis rely on efficient mass transfer besides material functionality, so that the optimization of material performance exposes the detailed understanding of relevant transport properties (such as D_L) and transport limitations as major research theme.[35,36] This, in turn, requires the generation of sufficient knowledge about the consequences of material preparation conditions for the resulting three-dimensional (3D) material morphology and process-relevant transport properties.[125–127] The approach is completed by identification of morphological descriptors that sensitively correspond to mass transfer resistances in the microscopically disordered pore spaces.[28]

For example, we have previously applied Voronoi tessellation[40] to computer-generated bulk[30] and cylindrically-confined[41] packings of monosized hard spheres, to characterize their degree of heterogeneity and correlate it with eddy dispersion simulated in the packings. Voronoi tessellation partitions the entire packing space into a set of non-overlapping Voronoi volumes associated with local packing density. The Voronoi cell in a packing of monosized hard spheres is the polyhedron that covers all points closer to a given sphere center than to any other, as illustrated by Fig. 1 in two and three dimensions. With the precise knowledge of particle positions, size, and shape, we performed a Voronoi tessellation for packings with systematically varied porosity and microstructure,[30] to assign statistical moments of the Voronoi volume distributions (standard deviation, skewness) to the carefully adjusted bed characteristics. The derived scalar measures correlated strongly with eddy dispersion in these packings: We observed excellent agreement between the statistical analysis, revealing a bed-porosity and packing generation-protocol dependent short-range disorder, and the short-range interchannel contribution to eddy dispersion.[30] The latter characterizes eddy dispersion in the interparticle pore space of randomly packed beds

[37] Torquato and Haslach. *Appl. Mech. Rev.*, 55, B62–B63, 2002.
[38] G. Guiochon, A. Felinger, and D. G. G. Shirazi. *Fundamentals of Preparative and Nonlinear Chromatography*. 2nd ed. Academic Press, 2006.
[39] J. Kärger, D. M. Ruthven, and D. N. Theodorou. *Diffusion in Nanoporous Materials, 2 Volume Set*. John Wiley & Sons, 2012. 932 pp.
[35] F. Gritti and G. Guiochon. *J. Chromatogr. A*, 1221, 2–40, 2012.
[36] F. Gritti and G. Guiochon. *Anal. Chem.*, 85, 3017–3035, 2013.
[125] M. R. Schure and R. S. Maier. *J. Chromatogr. A*, 1126, 58–69, 2006.
[126] M. F. Wahab et al. *Anal. Chem.*, 89, 8177–8191, 2017.
[127] L. E. Blue et al. *J. Chromatogr. A*, 1523, 17–39, 2017.
[28] T. Müllner, K. K. Unger, and U. Tallarek. *New J. Chem.*, 40, 3993–4015, 2016.
[40] A. Okabe et al. "Spatial Tessellations: Concepts and Applications of Voronoi Diagrams" in: *Int. Encycl. Geogr. People, Earth, Environ. Technol.* Chichester, England: John Wiley & Sons Ltd., 2000. 1–11
[30] S. Khirevich et al. *J. Chromatogr. A*, 1217, 4713–4722, 2010.
[41] S. Khirevich et al. *J. Chromatogr. A*, 1262, 77–91, 2012.

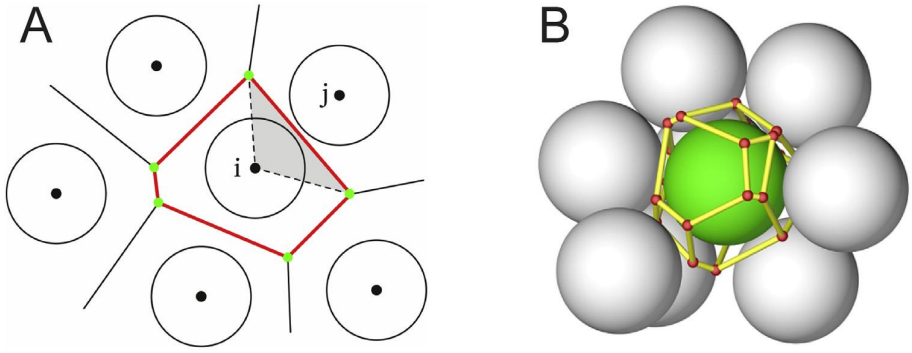

Figure 1.1: (A) Voronoi cells in a random configuration of monosized disks (two dimensions). The Voronoi cell of disk i (encased by the bold red lines) covers all points that are closer to this disk than to any other. The gray-shaded area represents the contribution of disk j to the Voronoi area of disk i. (B) Highlighted Voronoi cell in a random packing of monosized spheres (three dimensions), where the edges and corners of the cell are indicated by yellow sticks and red dots, respectively.

originating in velocity fluctuations over a length scale of $1-2$ particle diameters.[35,36,128,129]

While this simple tessellation scheme (Fig. 1.1) is straightforward for monosized disks and spheres, it has also been extended to polydisperse disks and spheres as well as to irregularly shaped objects.[42–45] However, real packings (like those in liquid chromatography) pose an even greater challenge with respect to the microstructure of particulate beds: In contrast to computer-generated packings of monosized or polydisperse ideal spheres, they may contain packing defects like particle oligomers and larger voids as well as contaminations and particle debris.[21,27] This issue is illustrated by Fig. 1.2. It is obvious that defects characterized by such a fine structure and a highly irregular shape make extremely difficult the adaptation and evaluation of a spatial tessellation scheme (similar to that in Fig. 1.1) to capture their influence on the effective longitudinal dispersion coefficient D_L and plate height H_L at a given average flow velocity (u_av).

An alternative to the spatial tessellation approach for morphological analysis of packings with defects (cf. Fig. 1.2), which helps us out of this problematic situation, is to resort to chord length distribution (CLD) analysis.[28] Since the generation of CLDs does not require assumptions about the size and shape of a solid, liquid, or void phase, it is virtually applicable to all multiphase materials.[31,130–132] In general, the chords sample a geometry by measuring distances between

[128] J. Giddings. *Dynamics of Chromatography. Part. 1: Principles and Theory*. New York, NY: Marcel Dekker, 1965.
[129] S. Khirevich et al. *Anal. Chem.*, 81, 7057–7066, 2009.
[42] N. N. Medvedev et al. *J. Comput. Chem.*, 27, 1676–1692, 2006.
[43] K. Lochmann, L. Oger, and D. Stoyan. *Solid State Sci.*, 8, 1397–1413, 2006.
[44] M. Danisch, Y. Jin, and H. A. Makse. *Phys. Rev. E*, 81, 051303, 2010.
[45] F. M. Schaller et al. *Philos. Mag.*, 93, 3993–4017, 2013.
[21] S. Bruns et al. *J. Chromatogr. A*, 1268, 53–63, 2012.
[27] A. E. Reising et al. *J. Chromatogr. A*, 1504, 71–82, 2017.
[31] P. Levitz. *Cem. Concr. Res.*, 37, 351–359, 2007.
[130] P. Levitz and D. Tchoubar. *J. Phys. I*, 2, 771–790, 1992.
[131] S. Torquato and B. Lu. *Phys. Rev. E*, 47, 2950–2953, 1993.
[132] S. Torquato. *Annu. Rev. Mater. Sci.*, 32, 77–111, 2002.

Figure 1.2: Packing defects in selected images from physical bed reconstruction by confocal laser scanning microscopy. The interparticle void space is shown in white.

two interfaces set apart by a homogenous phase. For this purpose, seed points are placed, for example, in the interparticle pore space of a packing. From each point, vectors are projected into space until they hit the interface. Chord lengths are then extracted as the sum of the absolute lengths of a pair of opposed vectors. Once a statistically significant number of chords has been collected, they are evaluated and assembled into a CLD. The chord lengths analyse the pore space morphology on a local scale, i.e., the majority of chords probe a single pore, but some chords also probe adjacent pores. Therefore, the CLD reveals information about local and short-range heterogeneities over length scales of a single pore and a few pores, respectively.[28]

We have used CLDs in the past to compare the morphologies of silica-based[20,22,46] and organic-polymer monoliths,[71,72] which similar to particulate beds with complex defects (Fig. 1.2) do not lend themselves to spatial tessellation schemes. In this brief follow-up article, we extend the CLD analysis to physical reconstructions of chromatographic packings. These have been investigated previously, especially in the context of column wall effects.[21,27,133] In the present work, we restrict ourselves to the analysis of bulk regions from these packings, which are unaffected by wall effects, to search for a relationship between short-range bed heterogeneity, parameters from the CLD analysis of the interparticle pore space, and longitudinal dispersion. The dispersion coefficients D_L for that purpose are derived by adapting the lattice-Boltzmann method (LBM) to simulate fluid flow directly in the reconstructions, serving as realistic 3D geometrical models, and a random-walk particle tracking (RWPT) technique to determine the transport and dispersion of passive, i.e., non-adsorbing, point-like tracers in the simulated flow fields.

These data for the physically reconstructed packings are complemented by corresponding data for computer-generated packings of monosized hard spheres, for which the packing-generation algorithm has been adjusted to realize a systematic variation of the bed density

[20] S. Bruns et al. *J. Chromatogr. A*, 1218, 5187–5194, 2011.
[22] D. Stoeckel et al. *Langmuir*, 31, 7391–7400, 2015.
[46] K. Hormann and U. Tallarek. *J. Chromatogr. A*, 1312, 26–36, 2013.
[71] K. K. Unger, R. Skudas, and M. M. Schulte. *J. Chromatogr. A*, 1184, 393–415, 2008.
[72] A. Galarneau et al. *Comptes Rendus Chim.*, 19, 231–247, 2016.
[133] A. E. Reising et al. *J. Chromatogr. A*, 1513, 172–182, 2017.

(porosity) and degree of packing heterogeneity (evaluated after the statistical analysis of the Voronoi volume distributions[30]). This systematic modulation contrasts with a random variation of these parameters in the real packings and will be therefore trend-setting in the establishment of generic morphology–transport relationships.

1.2 Employed packed beds

1.2.1 Computer-generated sphere packings

We used previously presented isotropic, bulk, random packings of monosized, hard spheres with dimensions of about $10 \times 10 \times 70$ sphere diameters and periodic boundary conditions in all directions.[30] Packing dimensions, the packing length in particular, were informed by the analysis of hydrodynamic dispersion, i.e., sufficiently long packings are required in the flow direction to reach asymptotic dispersion coefficients D_{L}.[134]

Four graded packing types were generated with a modified Jodrey-Tory algorithm,[135] a collective-rearrangement method.[136] Bed generation started from a random distribution of sphere centers in a box, for which sphere overlap was typical. Each iteration included the search for the two sphere centers with minimum pair-wise distance that defined the maximal sphere diameter at which no sphere-overlap occurred in the current bed configuration, followed by a symmetrical displacement of the two sphere centers up to a new distance. The displacement length used in the second step was scaled by a constant α. Different packing types were generated by varying the initial distribution of sphere centers (R-packings vs. S-packings) and the value of α.[30] R-packings were obtained from a random and uniform initial distribution of sphere centers in the simulation box, while for S-packings the simulation box was first divided into a number of equal cubes identical to the number of spheres in a generated packing and then each sphere center was placed randomly into a cube. This results in a more homogeneous structure of generated S-packings in comparison with R-packings. The scaling constant was set to $\alpha = 0.001$ (R $\times$ 0.001 protocol), $\alpha = 1$ (R and S protocols), or $\alpha = 2$ (S $\times$ 2 protocol). With a small displacement length, sphere centers remain close to their initial positions during bed generation, preserving the randomness of the initial distribution; a larger displacement length yields a more homogeneous distribution of sphere centers in the final bed.

Each packing type was generated at six bed porosities ($\varepsilon = 0.366$, 0.38, 0.40, 0.42, 0.44 and 0.46). However, we were unable to generate S $\times$ 2-packings at $\varepsilon = 0.366$. Altogether, 23 computer-generated sphere packings were employed in this study. For the CLD analysis and LBM–RWPT simulations, the generated packings were discretized on a uniform cubic grid with a resolution of 60 nodes per sphere diameter. It was shown that this grid resolution is sufficient for the accurate simulation of hydrodynamic dispersion coefficients D_{L} in random sphere packings.[134]

[134] S. Khirevich, A. Höltzel, and U. Tallarek. *Commun. Comput. Phys.*, 13, 801–822, 2013.
[135] W. S. Jodrey and E. M. Tory. *Phys. Rev. A*, 32, 2347–2351, 1985.
[136] A. Bezrukov, M. Bargieł, and D. Stoyan. *Part. Part. Syst. Charact.*, 19, 111–118, 2002.

1.2.2 Physically reconstructed packings

For the physical bed reconstructions, we resort to microstructures that are available from the literature.[21,27,133] They are based on the following C18-modified silica particles: $1.9\,\mu\mathrm{m}$ Acquity (Waters, Milford, MA), $2.6\,\mu\mathrm{m}$ Kinetex (Phenomenex, Aschaffenburg, Germany), $2.5\,\mu\mathrm{m}$ Poroshell (Agilent Technologies, Waldbronn, Germany), and $2.7\,\mu\mathrm{m}$ Halo (Advanced Materials Technologies, Wilmington, DE). The Acquity particles came in $75\,\mu\mathrm{m}$ i.d. fused-silica capillary columns prepared by Jorgenson and coworkers[27] using slurry concentrations of 140 and $200\,\mathrm{mg/mm}$ (subsequently referred to as Acquity 140 (cc) and Acquity 200 (cc), respectively) and in a $2.1\,\mathrm{mm}$ i.d. narrow-bore analytical column provided by Waters, designated as Acquity (ac). The remaining particles were packed into$1.9\,\mu\mathrm{m}1.9\,\mu\mathrm{m}$ i.d. fused-silica capillaries, as described before.[21] The bulk region of each capillary packing was reconstructed by confocal laser scanning microscopy.[21,27] On the other hand, the reconstruction from the bulk region of the analytical packing was obtained using focused ion-beam scanning electron microscopy (FIB–SEM).[133]

Relevant material properties like the mean particle diameter (d_p) and the relative standard deviation (RSD) of the particle size distribution (PSD), as well as the interparticle porosity (ε) of the reconstructions are summarized in Table 1.1. The measured PSDs can be found in the supplementary material of.[137] PSDs and d_p-values have been obtained from SEM images by ignoring contaminations as well as broken and agglomerated particles. We also determined the Sauter mean diameter $d_\mathrm{S} = 6V_\mathrm{solid}/A_\mathrm{ext}$ directly from the analysis of each reconstruction (cf. Table 1.1), where V_solid and A_ext are the volume of the solid phase (including structural defects) and its external surface area, respectively. The relevance of dS for dispersion simulations will be discussed in Section 1.5. The voxel size in the final reconstructions was $41.4\,\mathrm{nm}$ for Acquity (ac) and $30\,\mathrm{nm}$ for the other packings. Fig. 1.3 illustrates computer-generated packings from the set of the 23 (for a bed porosity of $\varepsilon = 0.40$), together with the six physically reconstructed beds employed for this investigation.

Table 1.1: Properties of the PSDs and bed reconstructions.

	Acquity (ac)	Acquity_140 (cc)	Acquity_200 (cc)	Halo	Kinetex	Poroshell
d_p [μm][a]	1.97	1.93	1.94	2.62	2.48	2.53
RSD (%)	14.8	15.2	15.2	4.6	2.8	6.0
d_S [μm][b]	1.96	1.99	2.01	2.53	2.32	2.4
ε [–][b]	0.394	0.453	0.458	0.363	0.400	0.384

[a]Determined from the SEM-based PSDs.
[b]Based on the analysis of the physical reconstructions.

1.3 Chord length distribution (CLD) analysis

The interparticle void space of the 23 computer-generated and six physically reconstructed packings was subjected to CLD analysis.[130,131] From the center of each void voxel adjacent to (i.e., in contact with) solid phase, 13 pairs of opposing vectors were sprouted along directions ac-

[137] D. Hlushkou and U. Tallarek. *J. Chromatogr. A*, 1581-1582, 173–179, 2018.

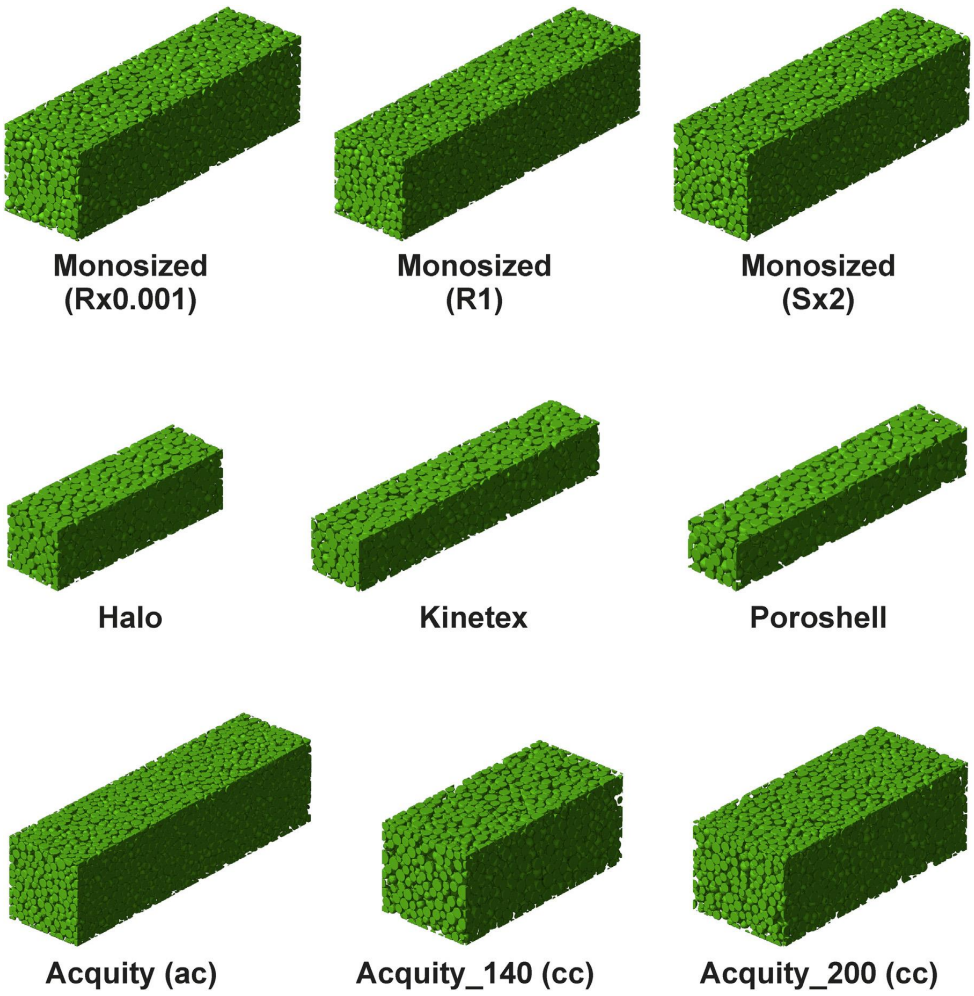

Figure 1.3: Visualization of selected computer-generated and physically reconstructed packings employed for morphological analysis and flow-dispersion simulations. Top row: computer-generated packings of monosized hard spheres ($\varepsilon = 0.40$); middle and bottom rows: physical reconstructions (see Table 1.1 for particle and bed characteristics).

cording to the scheme in Fig. 1.4, until they hit a solid–void interface. If a vector projected out of the packing boundaries, the associated vector pair was discarded. The sum of the lengths of an opposing vector pair (a chord) yielded the interface-to-interface distance while passing a point-of-origin (a seed point). According to the number of voxels along the solid–void interface in a packing (i.e., the number of seed points), the total number of generated chords ranged from 7.05×10^8 (Kinetex packing) to $\sim 1.5 \times 10^9$ (computer-generated packings with $\varepsilon = 0.366$). The aforementioned (deterministic) approach to the allocation of seed points differs slightly from that we used in our previous studies;[20–22,46–48] where these points were placed randomly in the void space. With the new approach, statistical uncertainty resulting from random positions of the seed points, which may affect the accuracy of the CLD analysis, was eliminated. Moreover, it

[47] T. Müllner et al. *Adv. Mater.*, 27, 6009–6013, 2015.
[48] T. Müllner et al. *Langmuir*, 33, 2205–2214, 2017.

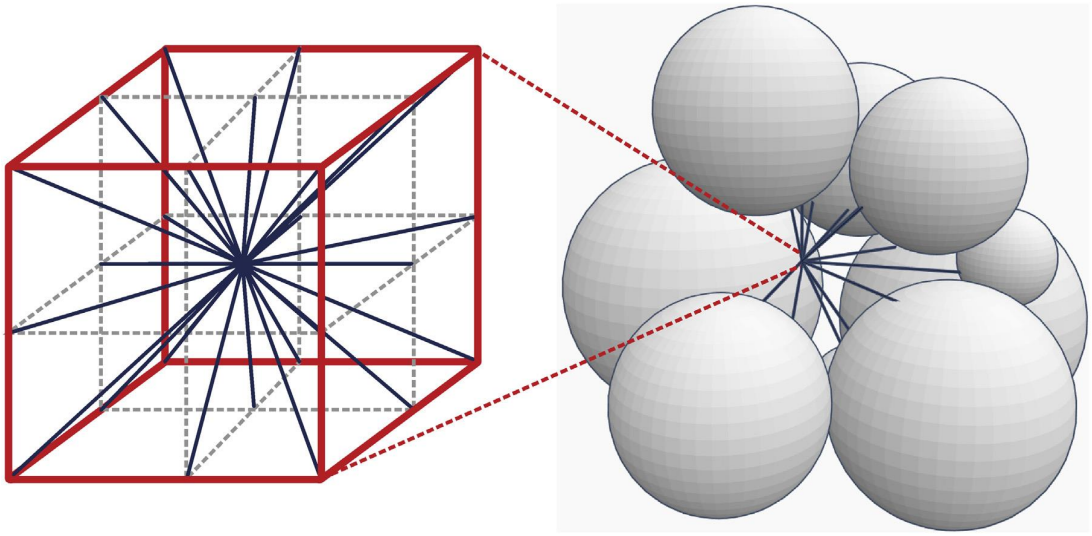

Figure 1.4: Illustration of the directions for 3D spreading of chords from a single seed point in the center of a voxel and implementation in the interparticle void space of a packing (i.e., for voxels along the solid–void interface).

allows to involve the complete area of the solid–void interface in the CLD analysis.

From the CLDs the mean chord length (μ) and standard deviation (σ) were determined for each packing. It was previously shown that the first-moment parameter μ and the second-moment parameter in the form $k = \mu^2/\sigma^2$ can be correlated to, respectively, the transchannel and the short-range interchannel contribution to longitudinal dispersion (and chromatographic plate height) in computer-generated random sphere packings.[28]

1.4 Simulation of longitudinal dispersion

The LBM has become very powerful for flow simulations in computer-generated sphere packings[30,129,138–143] and reconstructed monoliths[144,145] to study with unprecedented detail the hydrodynamics in chromatographic supports. Validation and program realization of the LBM flow simulation and RWPT-method used here to determine longitudinal dispersion coefficients D_L in the 23 computer-generated and six physically reconstructed packings have been reported before.[134,143] D_L-values for the computer-generated packings discussed in Section 1.5 correspond to the plate heights H_L presented in.[30] In these papers, all relevant details about the packing generation and implementation of the simulations can be found. By contrast, the pore-scale simulation of fluid flow and

[138] R. S. Maier et al. *Phys. Fluids*, 12, 2065–2079, 2000.
[139] M. R. Schure et al. *Anal. Chem.*, 74, 6006–6016, 2002.
[140] S. Khirevich et al. *Anal. Chem.*, 79, 9340–9349, 2007.
[141] A. Daneyko et al. *Anal. Chem.*, 83, 3903–3910, 2011.
[142] D. Hlushkou et al. *J. Phys. Chem. C*, 117, 22974–22985, 2013.
[143] A. Daneyko et al. *J. Chromatogr. A*, 1407, 139–156, 2015.
[144] H. Koku et al. *J. Chromatogr. A*, 1237, 55–63, 2012.
[145] D. Hlushkou et al. *J. Chromatogr. A*, 1303, 28–38, 2013.

dispersion in physically reconstructed chromatographic packings of such fine ($\sim 3\,\mu\mathrm{m}$) particles, to our knowledge, has not been reported so far or even been used in a further study to establish correlations with descriptors of packing microstructure.

For this purpose, we simulated fluid flow in the interparticle pore space by the LBM with the 3D lattice spacing adjusted to the voxel size in the reconstructed packings. At the solid–liquid interface, a halfway bounce-back rule was used to implement the no-slip flow velocity boundary condition. The body force associated with the hydrostatic pressure was taken as uniform over the lattice with zero components in transverse directions and a positive value in longitudinal direction. Mirror and periodic boundary conditions were imposed at the external faces of a reconstruction in longitudinal and transverse directions, respectively. Then, the calculated 3D velocity fields $\boldsymbol{u}(\boldsymbol{r})$ were used to simulate advective–diffusive transport with a RWPT technique, where a large number ($N = 10^6$) of passive, point-like tracers were initially distributed randomly and uniformly in the interparticle void space of a packing. During each time step Δt, the displacement of a tracer was determined as the sum of advective and diffusive contributions according to

$$\Delta \boldsymbol{r} = \boldsymbol{u}(\boldsymbol{r})\Delta t + \boldsymbol{\beta} \tag{1.1}$$

where $\boldsymbol{\beta}$ is a vector with random orientation in space and a length governed by a Gaussian distribution with zero mean and standard deviation $(6D_\mathrm{m}\Delta t)^{1/2}$ ($6D_\mathrm{m}$ is the diffusion coefficient in free, unconfined space). In all the simulations, we assumed that the packing particles were nonporous, i.e., impermeable for tracers. Passive interaction of the tracers with the packing particles was handled through a multiple-rejection boundary condition at the particle surface, that is, when a tracer hit the impermeable surface during an iteration, the displacement was rejected and recalculated until the tracer position was in the pore space. After each time step, all tracer positions were recorded and a time-dependent longitudinal dispersion coefficient evolved from

$$D_\mathrm{L}(t) = \frac{1}{2N}\frac{d}{dt}\sum_{i=1}^{N}\left[\Delta x_i(t) - \langle \Delta x(t)\rangle\right]^2 \tag{1.2}$$

where $\Delta x_i(t) \equiv x_i(t) - x_i(0)$ and $\langle \Delta x(t)\rangle$ are the displacement in the longitudinal direction of the i-th tracer and the average displacement of the tracer ensemble after time t, respectively. The time-independent dispersion coefficients D_L were determined from the asymptote of the monitored transient dispersion curve $D_\mathrm{L}(t)$, observed in the long-time limit.

1.5 Results and conclusions

With the LBM–RWPT approach briefly described above, we simulated advective–diffusive transport in all packings at a reduced flow velocity or Péclet number ($Pe = u_\mathrm{av} d_\mathrm{S}/D_\mathrm{m}$) of 10 to

determine the longitudinal dispersion coefficients D_L. It was shown[141] that the use of the Sauter (surface-mean) diameter d_S for the definition of Pe ensures a comparison of dispersion coefficients in packings with different PSDs under the condition of equal total surface area. The pore-scale velocity non-uniformity of the flow field in the interparticle void space of a packing is caused by the no-slip boundary condition at the surface of the solid particles. Therefore, the external surface area of the particles has an impact on the flow field and on the dispersion contribution that emerges from this flow non-uniformity. The dispersion regime for a porous medium in the velocity range of ca. $5 < Pe < 300$ is referred to as the "boundary-layer dispersion regime" in recognition of the presence and importance of the viscous boundary layer at the solid–fluid interface, in which mass transport normal to the interface is diffusion-limited.[141,146,147] Additionally, the use of d_S instead of d_p is more appropriate to account for the effect of the packing defects (contaminations, broken particles, debris, agglomerates, etc.) on the actual flow heterogeneity and resulting hydrodynamic dispersion. $Pe = 10$ was chosen because at this value advection already becomes a dominating transport mechanism. Thus, in this study we consider a situation, which is different to that we analyzed in the preceding paper,[137] when the only transport mechanism in the reconstructed packed beds was diffusion.

Fig. 1.5 shows the evolution of the longitudinal dispersion coefficients $D_L(t)$, normalized by D_m, in the reconstructed packings as a function of the dimensionless convective time $t_c = u_{av}t/d_S$. A value of $t_c = 1.0$ corresponds to the average time it takes a tracer to be transported downstream over a distance of d_S by the flow. At sufficiently long times, transient dispersion coefficients $D_L(t)$ approach asymptotic values D_L (Fig. 1.5), with superimposed stochastic noise inherent for a random process (diffusion in our case).

The asymptotic values of D_L/D_m (at $Pe = 10$) are plotted in Fig. 1.6A as a function of the bed porosity ε for all packings. In general, D_L/D_m-values for the physically reconstructed packings (solid circles) are larger than those for the computer-generated packings (open red symbols) at the corresponding porosity. The observed differences in the dispersion coefficients between the physically reconstructed and computer-generated packings can be explained by structural defects that are present in the real packings (cf. Fig. 1.2).[137] These defects influence the pore space morphology and introduce additional structural heterogeneity, which is absent in the computer-generated packings. For the latter, the D_L/D_m-value decreases at any porosity from the R $\times$ 0.001 to the S $\times$ 2 packing type. At low porosities (ε =0.366 and 0.38), the data points corresponding to the different types of computer-generated packings almost coincide but fan out with increasing ε (Fig. 1.6A). Furthermore, for any packing generation protocol the value of D_L/D_m increases with the bed porosity. The monotonic increase of D_L/D_m with ε, as observed in Fig. 1.6A for the computer-generated packings, is broken for the real packings. The largest D_L/D_m-values from all investigated bed structures were obtained for Acquity 140 (cc) and Acquity 200 (cc), which are characterized also by the highest porosity among the physically

[146] D. L. Koch and J. F. Brady. *J. Fluid Mech.*, 154, 399–427, 1985.

[147] M. Sahimi. *Flow and Transport in Porous Media and Fractured Rock: From Classical Methods to Modern Approaches*. 2n ed. Weinheim: Wiley-VCH, 2011.

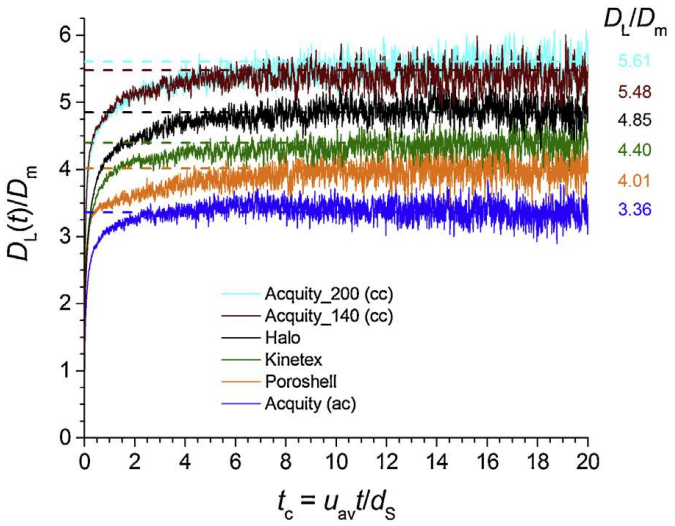

Figure 1.5: Transient longitudinal dispersion coefficient $D_\mathrm{L}(t)$ in the reconstructed packings, normalized by the molecular diffusion coefficient D_m, as a function of the dimensionless convective time $t_\mathrm{c} = u_\mathrm{av}t/d_\mathrm{S}$ at a Péclet number of $Pe = u_\mathrm{av}d_\mathrm{S}/D_\mathrm{m} = 10$. Here, u_av is the average flow velocity and d_S the Sauter diameter (cf. Table 1.1). The column to the right summarizes the $D_\mathrm{L}/D_\mathrm{m}$-data, where D_L is the asymptotic, long-time value of $D_\mathrm{L}(t)$.

reconstructed packings. At the same time, the $D_\mathrm{L}/D_\mathrm{m}$value in the Halo packing is larger than in the Poroshell, Kinetex, and Acquity (ac) packings, although the Halo reconstruction has the lowest porosity among all analyzed structures. The Halo packing is also characterized by the largest difference between its $D_\mathrm{L}/D_\mathrm{m}$-value and that for the computer-generated packing at a similar bed porosity. This finding indicates that the dependence of the longitudinal dispersion coefficient on porosity for real packed beds is more complex than for the computer-generated packings and also more intricate than a simple, generic dispersivity–porosity relationship would suggest.

In Fig. 1.6B, we present the values of σ/μ for all packings, i.e., the standard deviation σ of a CLD normalized by the corresponding mean chord length μ, as a function of the porosity. The same color-symbol coding is used as in Fig. 1.6A. The comparison of both panels in Fig. 1.6 reveals a remarkably close relation between $D_\mathrm{L}/D_\mathrm{m}$ and σ/μ for all packings. Similar to the dispersion coefficients, the values of σ/μ for the physically reconstructed packings are always higher than those for the computer-generated packings at the corresponding porosity. For the latter, the normalized standard deviations of the CLDs have very similar values at low bed porosities ($\varepsilon = 0.366$ and 0.38) and fan out with increasing ε. In these packings, the σ/μ-value also decreases from the R $\times$ 0.001 to the S $\times$ 2 packing type at any porosity. Finally, the σ/μ–ε dependence for the physically reconstructed packings demonstrates the same non-monotonic behavior as the dispersion coefficients simulated in these packings.

The close relation between the longitudinal dispersion coefficient and the σ/μ-value (characterizing the short-range heterogeneity) for the investigated packings is demonstrated with Fig. 1.7: All data points are close to the dashed line and the largest relative difference be-

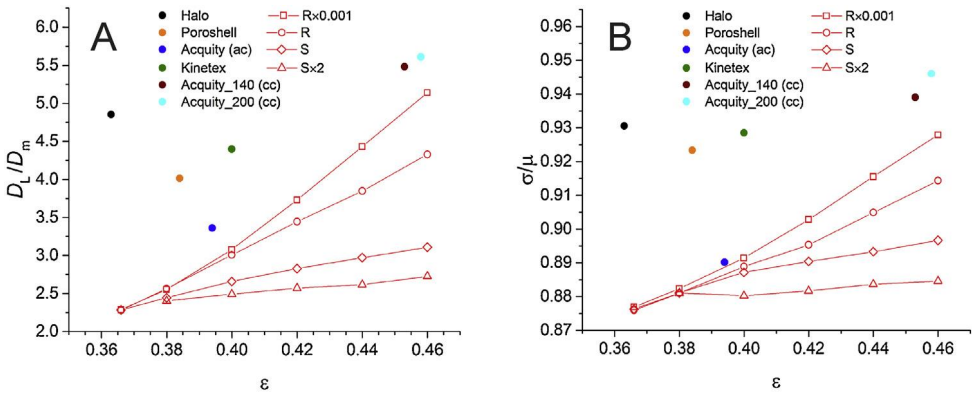

Figure 1.6: Correlation between $D_\mathrm{L}/D_\mathrm{m}$ at $Pe = 10$ and σ/μ from CLD analysis for all packings. The dashed line is a linear fit to the data points.

tween the data and the approximating straight line is less than $13\,\%$ (the value of the adjusted R^2 was 0.959). This result implies that the proposed morphological descriptor (σ/μ) based on the CLD analysis can be applied for a quite accurate estimation of the dispersion coefficient in particle-packed beds, independent from the underlying PSD, packing preparation protocol, bed porosity, and the occurrence of packing defects.

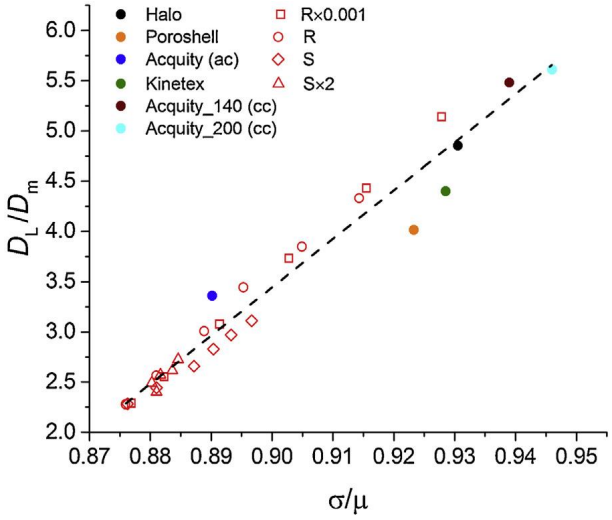

Figure 1.7: (A) Results of the flow-dispersion simulations: $D_\mathrm{L}/D_\mathrm{m}$ at $Pe = 10$ as a function for all packings. (B) Results of the morphological analysis: σ/μ as a function of ε, where σ is the standard deviation of a CLD and μ the mean chord length.

To summarize, this work has revealed two important points. First, the relationship between longitudinal dispersion and bed porosity (D_L–ε) for the reconstructed packings demonstrates non-monotonic behavior. This complexity prevents the use of a generic dispersivity–porosity relationship for real packings. Second, the morphological descriptor based on CLD analysis of the interparticle void space in the packings adequately accounts for the subtle morphological

features in real packings and their influence on dispersion. This knowledge may help to derive more quantitative dispersivity–porosity relationships in the future.

Acknowledgements

The authors thank the Deutsche Forschungsgemeinschaft DFG (Bonn, Germany) for financial support of this work under grant TA 268/9–1.

Chapter 2

Hindrance factor expression for diffusion in random mesoporous adsorbents obtained from pore-scale simulations in physical reconstructions

Authors: Stefan-Johannes Reich[§], Artur Svidrytski[§], Dzmitry Hlushkou, Daniela Stoeckel, Christian Kübel, Alexandra Höltzel, and Ulrich Tallarek*

State of publication:

Published on February 7, 2018 in Industrial & Engineering Chemistry Research, Vol. 57.8, pp 3031–3042

DOI: 10.1021/acs.iecr.7b04840

Abstract Hindered diffusion of solutes is the rate-limiting step in many processes where random porous media play a central role as providers of adsorbing or reactive interfaces. Key to an optimized layout of these processes is the knowledge of the overall diffusive hindrance factor $H(\lambda) = D_{\text{eff,H}}(\lambda)/D_{\text{m}}$, which quantifies the degree to which diffusion through a material (represented by the effective diffusion coefficient $D_{\text{eff,H}}$) is hindered compared with diffusion in the bulk liquid (represented by D_{m}) in dependence of λ, the ratio of solute size to mean pore size. To arrive at an adequate hindrance factor expression for random mesoporous silica, we use electron tomography to physically reconstruct the mesopore space of three macro-mesoporous silica monoliths. The samples share the same general mesopore shape and topology at varied mean feature size, as established by morphological analysis, and serve as realistic models in pore-scale simulations of hindered diffusion. From a large set of $D_{\text{eff,H}}(\lambda)$ values for $0 \leq \lambda \leq 0.9$, we derive a quantitative expression for $H(\lambda)$ that captures the morphological evolution (in dependence of λ) and allows to predict the extent of hindered diffusion from material properties. We propose the expression for structures of similar morphology as the investigated samples, which potentially encompasses all mesoporous silica materials obtained through sol–gel processing.

[§] S.-J.R. and A.S. contributed equally to this work.

2.1 Introduction

Diffusion of solute molecules or particles through random networks of liquid-filled pores whose dimensions are comparable to the solute or particle size is ubiquitous in nature and technology.[49–55] Depending on the process, hindered diffusion may have desirable or undesirable consequences. For example, the exclusion of solute molecules or particles from parts of the porous network due to hindered diffusion may be intended (filtering) or harmful. The latter is the case whenever solid–liquid interfaces play a central role in the process, as in heterogeneous catalysis and chemical separations. Partial exclusion of solute molecules diminishes the active surface area of a support, which in turn directly decreases its mass loadability. And when the interfacial kinetics (sorption, reaction) are fast, the diffusive transport of solutes to and from the active sites on the surface becomes the limiting factor to the process performance.

Key to improving processes controlled by hindered diffusion is to know the relationship between the morphology of the confining medium and the global (or overall) diffusive hindrance factor, which quantifies the degree to which the diffusion of solute molecules or particles (in the following referred to as tracers) is hindered by the confinement based on the ratio between tracer size and pore size (λ). The global diffusive hindrance factor is defined as $H(\lambda) = D_{\text{eff,H}}(\lambda)/D_{\text{m}}$, whereby $D_{\text{eff,H}}(\lambda)$ is the effective (long-time, asymptotic) diffusion coefficient of the tracer for diffusion through the confining medium and D_{m} is the (free) diffusion coefficient of the tracer in the bulk liquid. The value of $D_{\text{eff,H}}(\lambda)$ reflects hydrodynamic and excluded-volume effects and is therefore intrinsically tied to the morphology of the porous medium.[56,57]

Diffusive hindrance factor expressions for simple geometrical models, cylindrical or slit pores, are readily available, as summarized by Dechadilok and Deen.[58] The famous Renkin equation, for example, considers the diffusion of spherical tracers through a cylindrical pore, assuming a drag coefficient that is is constant over the pore cross-section and equal to the drag coefficient along the pore axis (centerline approximation); $H(\lambda)$ is then given by[58]

$$H(\lambda) = \Phi(\lambda)K_{\text{d}}(\lambda) = (1-\lambda)^2(1 - 2.104\lambda + 2.09\lambda^3 - 0.95\lambda^5) \tag{2.1}$$

The overall hindrance factor $H(\lambda)$ is the product of the equilibrium partitioning coefficient $\Phi(\lambda) = (1-\lambda)^2$, which is the cross-sectional average tracer concentration at either pore end

[49] J. Kärger and D. M. Ruthven. *New J. Chem.*, 40, 4027–4048, 2016.
[50] A. T. Florence. *J. Control. Release*, 164, 115–124, 2012.
[51] Y. S. Polyakov and A. L. Zydney. *J. Memb. Sci.*, 434, 106–120, 2013.
[52] H. Al-Obaidi and A. T. Florence. *J. Drug Deliv. Sci. Technol.*, 30, 266–277, 2015.
[53] C. Sievers et al. *ACS Catal.*, 6, 8286–8307, 2016.
[54] J. M. Angelo and A. M. Lenhoff. *J. Chromatogr. A*, 1440, 94–104, 2016.
[55] V. I. Syngouna and C. V. Chrysikopoulos. *Sci. Total Environ.*, 545-546, 210–218, 2016.
[56] M. J. Skaug et al. *ACS Nano*, 9, 2148–2156, 2015.
[57] F. Babayekhorasani et al. *Soft Matter*, 12, 8407–8416, 2016.
[58] P. Dechadilok and W. M. Deen. *Ind. Eng. Chem. Res.*, 45, 6953–6959, 2006.

divided by the adjacent external particle concentration for purely steric interactions between tracer and pore, and the local hindrance factor $K_{\mathrm{d}}(\lambda) = D_{\mathrm{eff,K}}(\lambda)/D_{\mathrm{m}}$, which quantifies the degree to which diffusion inside the cylindrical pore is hindered due to hydrodynamic interactions between tracer and the pore wall. Equation 2.1 is valid for $\lambda \leq 0.4$; within the centerline approach, this relationship was extended by Bungay and Brenner[61] for $0 \leq \lambda \leq 1$ (cf. Table 1 in Deen[62]). Further, Dechadilok and Deen[58] presented an improved hindrance factor correlation for $0 \leq \lambda \leq 0.95$ (see Figure 2 in their paper and their eq 16) based on the off-axis hydrodynamic results of Higdon and Muldowney[148] ($0 \leq \lambda \leq 0.9$) and of Mavrovouniotis and Brenner[149] ($\lambda = 0.95$). Equation 2.1 refers to a single, cylindrical pore of constant cross-section, but is widely applied to random porous media as well. An improved description of hindered diffusion through microscopically disordered materials was achieved by embedding the Renkin equation (eq 2.1) in a model that employs a semi-empirical relationship for the evolution of the pore network morphology with increasing λ. The model considers that the accessible porosity of a porous medium as well as the diffusive tortuosity of the accessible pore space are functions of λ and gives the overall hindrance factor as[63]

$$H(\lambda) = \frac{\varepsilon(\lambda)}{\tau(\lambda)} K_{\mathrm{d}}(\lambda) = \frac{\varepsilon_0 (1-\lambda)^2}{\tau(\lambda)} (1 - 2.104\lambda + 2.09\lambda^3 - 0.95\lambda^5) \tag{2.2}$$

For $\lambda = 0$, eq 2.2 recovers the familiar expression $D_{\mathrm{eff,H}}/D_m (= \varepsilon_0 D_{\mathrm{eff,K}}/D_m) = \varepsilon_0/\tau_0$, where ε_0 and τ_0 are the porosity and diffusive tortuosity, respectively, experienced by a point-like tracer. For the effective diffusive tortuosity $\tau(\lambda)$ of the accessible porosity $\varepsilon(\lambda)$ experienced by a finite-size tracer, Wernert et al.[63] proposed a modified Weissberg equation

$$\tau(\lambda) = 1 - p \ln[\varepsilon(\lambda)] = 1 - p \ln[\varepsilon_0 (1-\lambda)^2] \tag{2.3}$$

with a fitting parameter p to account for the pore space topology. Estimating the effective diffusive tortuosity of the porous medium with eq 2.3 instead of using a constant tortuosity factor improved the description of experimental diffusivities of polystyrene particles through amorphous, mesoporous silica significantly. Further refinement is in principle possible by incorporating additional material parameters, for example, for the pore size distribution and the pore interconnectivity. Nevertheless, eqs 2.2 and 2.3 represent rather simple models, a cylindrical pore and a bed of overlapping spheres, respectively; it is therefore questionable if these models can be stretched so far as to represent the complex morphology of random porous media.

[61] P. M. Bungay and H. Brenner. *Int. J. Multiph. Flow*, 1, 25–56, 1973.
[62] W. M. Deen. *AIChE J.*, 33, 1409–1425, 1987.
[148] J. J. L. Higdon and G. P. Muldowney. *J. Fluid Mech.*, 298, 193–210, 1995.
[149] G. M. Mavrovouniotis and H. Brenner. *J. Colloid Interface Sci.*, 124, 269–283, 1988.
[63] V. Wernert, R. Bouchet, and R. Denoyel. *Anal. Chem.*, 82, 2668–2679, 2010.

Experimental mass transport studies by pulsed field-gradient nuclear magnetic resonance,[64–67] microimaging,[68,69] and various optical methods[56,57,70] have revealed diffusion in random porous media as more complex than often assumed, suggesting that the true morphology of a material needs to be expressly considered to derive improved diffusive hindrance factor expressions. This has recently become possible through methods that allow the physical reconstruction of a porous material at the required resolution. Physical reconstructions offer several advantages. First, the structural heterogeneity of a material is spatially resolved and can be quantitatively assessed over several length scales, disclosing salient features of a preparation process. Second, the morphology can be analysed by statistical methods to derive appropriate structural descriptors for different mass transport properties. And third, the reconstructions can serve as models for direct (pore-scale) numerical simulations of the studied transport processes, such as hindered diffusion. This allows to individually address and quantify the effects from material morphology, hydrodynamics, and specific interactions between tracer and pore surface.[28,31,32]

Pore-scale simulations of hindered diffusion in physical reconstructions of random porous media are still scarce in the literature. In a pioneering work, Langford et al.[150] implemented Brownian dynamics and network modeling for predicting the effective diffusion coefficients of different-sized tracers in three chromatographic adsorbents (a network of cross-linked agarose bundles and methacrylate co-polymer base matrices) reconstructed by electron tomography. The simulations revealed subtle trends in the transport data, for instance, a trade-off between pore size and connectivity effects for different tracer sizes. Through dissipative particle dynamics simulations, Müter et al.[151] studied the diffusion of spherical tracers with variable diameter and attractive surface interaction in the highly irregular pore system of chalk, reconstructed by X-ray nanotomography. They found that tracer size and adhesion properties have a strong influence on tracer mobility and must be taken into account when predicting the permeability in nanoporous rocks from primary petrophysical parameters, such as the surface area, porosity, and diffusive tortuosity. Recently, we simulated hindered diffusion for $\lambda \leq 0.474$ in mesoporous silica reconstructed by scanning transmission electron microscopy (STEM) tomography.[33] For $\lambda > 0.2$, the simulated values of $D_{\text{eff,H}}(\lambda)$ were significantly overestimated by the Renkin equation (as well as by the expression proposed by Deen and Dechadilok); we also observed that the effective geometrical and topological properties of the material varied strongly with λ.

[64] J. Kärger and R. Valiullin. *Chem. Soc. Rev.*, 42, 4172–4197, 2013.
[65] T. Titze et al. *Angew. Chemie Int. Edit.*, 54, 14580–14583, 2015.
[66] A. Galarneau et al. *J. Phys. Chem. C*, 120, 1562–1569, 2016.
[67] F. Elwinger, P. Pourmand, and I. Furó. *J. Phys. Chem. C*, 121, 13757–13764, 2017.
[68] J. Kärger et al. *Chem.-Ing.-Tech.*, 82, 779–804, 2010.
[69] J. Kärger et al. *Nat. Mater.*, 13, 333–343, 2014.
[70] M. J. Skaug and D. K. Schwartz. *Ind. Eng. Chem. Res.*, 54, 4414–4419, 2015.
[28] T. Müllner, K. K. Unger, and U. Tallarek. *New J. Chem.*, 40, 3993–4015, 2016.
[31] P. Levitz. *Cem. Concr. Res.*, 37, 351–359, 2007.
[32] B. Coasne. *New J. Chem.*, 40, 4078–4094, 2016.
[150] J. F. Langford et al. *J. Chromatogr. A*, 1126, 95–106, 2006.
[151] D. Müter et al. *J. Phys. Chem. C*, 119, 10329–10335, 2015.
[33] D. Hlushkou, A. Svidrytski, and U. Tallarek. *J. Phys. Chem. C*, 121, 8416–8426, 2017.

Because the extent of hindered diffusion in silica supports is critical to their performance in various important applications[5,71–73] (storage/controlled release, sorption, separation, catalysis), we now aim for a quantitative description of hindered diffusion in random mesoporous silica through an $H(\lambda)$ expression that is valid over the range of $0 \leq \lambda \leq 0.9$.

2.2 Experimental section

2.2.1 Mesoporous silica samples

Three macro-mesoporous silica monoliths (Figure 2.11, Supporting Information), which according to their preparation history were likely to retain similarities in their mesopore spaces, serve as mesoporous silica samples in this study. The monoliths came from a set of six received from Merck Millipore (Darmstadt, Germany) in form of analytical columns for reversed-phase liquid chromatography (rods of $4.6\,\mathrm{mm}$ i.d. $\times\, 100\,\mathrm{mm}$ length, clad in polyether ether ketone, the silica surface modified with C_{18} chains and fully endcapped). Cladding and surface modifications were removed for this study as described in the Supporting Information. The monoliths were prepared by standard sol–gel processing combined with chemically induced phase separation yielding wet, macro–microporous gels, followed by hydrothermal treatment of the gels to widen the micropores to mesopores through surface etching.[152] Varying the conditions of the hydrothermal treatment step produced six monoliths with highly similar macropore space properties (mean macropore size, $1.1–1.2\,\mu\mathrm{m}$; macroporosity, $0.56–0.58$, skeleton thickness: $0.7–0.8\,\mu\mathrm{m}$), but different mesopore size ($d_{\mathrm{meso}} = 5.5–26\,\mathrm{nm}$), mesoporosity, and surface area.[153] The three samples are denoted according to their mean mesopore size d_{meso}, determined by standard nitrogen physisorption analysis (Figure 2.12), as Si12 ($d_{\mathrm{meso}} = 12.3\,\mathrm{nm}$), Si21 ($d_{\mathrm{meso}} = 21.3\,\mathrm{nm}$), and Si26 ($d_{\mathrm{meso}} = 25.7\,\mathrm{nm}$).

2.2.2 STEM Tomography

For STEM tomography[154,155] a small piece from a monolith was ground in a mortar. The silica crumbs were then dusted over a holey Cu grid (Quantifoil Micro Tools, Jena, Germany), on which Au fiducial markers ($6.5\,\mathrm{nm}$ diameter) were deposited from an aqueous suspension (CMC, University Medical Center, Utrecht, The Netherlands). Electron tomography was performed using an image-corrected Titan $80–300$ TEM (FEI, Hillsboro, OR) at the Karlsruhe Nano Micro Facility, operated at an acceleration voltage of $300\,\mathrm{kV}$ in STEM mode with a nominal beam diameter of $0.2\,\mathrm{nm}$. STEM images were collected with a high-angle annular dark-field (HAADF) collector

[5] D. Enke, R. Gläser, and U. Tallarek. *Chem.-Ing.-Tech.*, 88, 1561–1585, 2016.
[71] K. K. Unger, R. Skudas, and M. M. Schulte. *J. Chromatogr. A*, 1184, 393–415, 2008.
[72] A. Galarneau et al. *Comptes Rendus Chim.*, 19, 231–247, 2016.
[73] E. Aznar et al. *Chem. Rev.*, 116, 561–718, 2016.
[152] S. Altmaier and K. Cabrera. *J. Sep. Sci.*, 31, 2551–2559, 2008.
[153] K. Hormann and U. Tallarek. *J. Chromatogr. A*, 1365, 94–105, 2014.
[154] P. A. Midgley and M. Weyland. *Ultramicroscopy*, 96, 413–431, 2003.
[155] C. Kübel et al. *Microsc. Microanal.*, 11, 378–400, 2005.

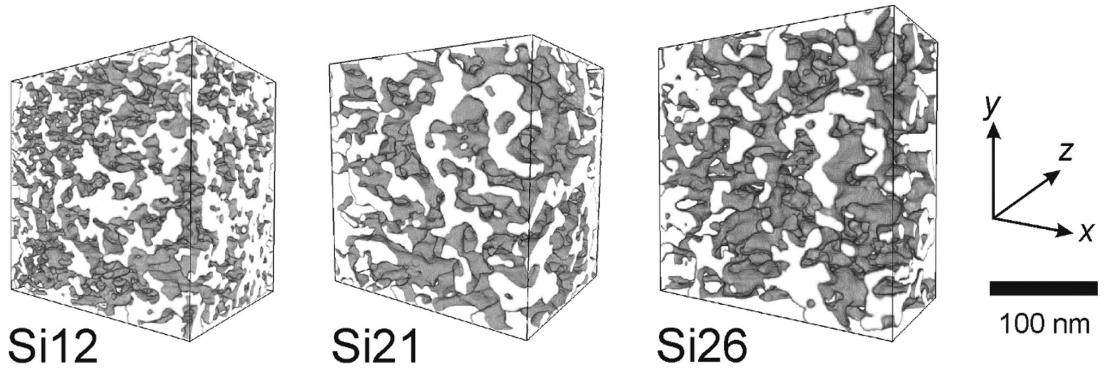

Figure 2.1: 3D physical reconstructions (white–solid, gray–void) obtained by STEM tomography of the microscopically disordered mesopore space of three macro–mesoporous silica monoliths (Figure 2.11). The monoliths stem from the same sol–gel processing step, but were subjected to varied conditions during the postgelational, hydrothermal treatment step. The mean mesopore size increases from sample Si12 ($d_{\text{meso}} = 12.3\,\text{nm}$) over sample Si21 ($d_{\text{meso}} = 21.3\,\text{nm}$) to sample Si26 ($d_{\text{meso}} = 25.7\,\text{nm}$). With physical dimensions ($x \times y \times z$) of $227.5 \times 227.5 \times 175\,\text{nm}^3$ (Si12), $225 \times 225 \times 175\,\text{nm}^3$ (Si21), and $270 \times 270 \times 135\,\text{nm}^3$ (Si26), the reconstructions have volumes of $9–10\,\text{nL}$.

over a range of $-74°$ to $74°$ (in $2°$ steps) for samples Si12 and Si21 and from $-76°$ to $76°$ (in $1°$ steps) for sample Si26. Image alignment was performed using IMOD 4.7[156] with 35 fiducial markers yielding an average residual alignment error of ~ 2, ~ 1.5 and ~ 1.2 pixels for sample Si12, Si21, and Si26, respectively. Subsequent 3D reconstruction was performed using the Xplore3D software package (FEI) with 25 iterations of the implemented SIRT algorithm.[157] Images were denoised using the nonlinear anisotropic diffusion filter implemented in IMOD. They were then segmented manually, restored, and rendered in AMIRA (Visage Imaging, Berlin, Germany), as described previously.[14] The final image stacks had the following dimensions ($x \times y \times z$): $227.5 \times 227.5 \times 175\,\text{nm}^3$ consisting of $0.35\,\text{nm}^3$ voxels for sample Si12; $225 \times 225 \times 175\,\text{nm}^3$ consisting of $0.5\,\text{nm}^3$ nm3 voxels for sample Si21; and $270 \times 270 \times 135\,\text{nm}^3$ consisting of $0.5\,\text{nm}^3$ voxels for sample Si26. The physical reconstructions (Figure 2.1) cover a volume of $\sim 9\,\text{nL}$ (Si12 and S21) or $\sim 10\,\text{nL}$ (Si26).

2.2.3 Chord Length Distribution (CLD) Analysis

A CLD of the void space (or solid phase) was obtained by placing seed points randomly into the void space (or solid phase) of a reconstruction, as indicated by the left panel in Figure 2.2.[28,31] In particular, 32 equiangularly distributed vectors per seed point were spread out until they reached the solid–void border. The length of a chord consisting of two opposing vectors was collected in a histogram, unless one vector projected out of the image bounds, in which case the chord was discarded. Seed points were generated until 10^6 chords had been collected. Using the Levenberg–Marquardt algorithm, the histogram was fitted to the *k*-Gamma function (central

[156] J. R. Kremer, D. N. Mastronarde, and J. R. McIntosh. *J. Struct. Biol.*, 116, 71–76, 1996.
[157] P. Gilbert. *J. Theor. Biol.*, 36, 105–117, 1972.
[14] D. Stoeckel et al. *Langmuir*, 30, 9022–9027, 2014.

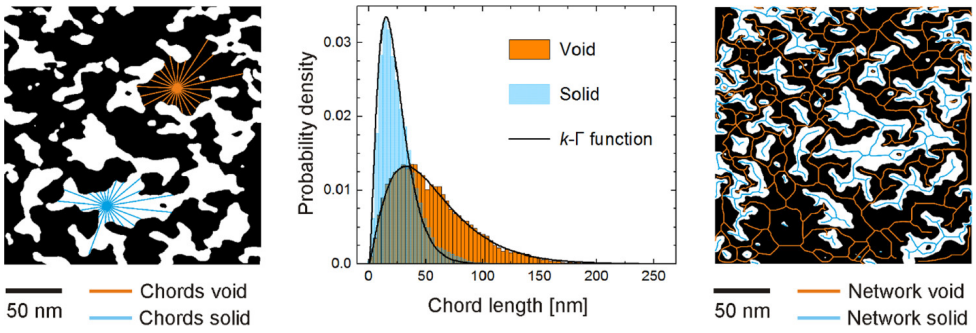

Figure 2.2: Scheme illustrating CLD (left and middle) and medial axis analysis (right) of a reconstructed mesopore space. (Left) From seed points, which are randomly distributed over the entire void space (or solid phase), vectors are spread in equiangular directions. If two opposing vectors reach the solid–void border, the sum of both vector lengths is counted as a chord length; otherwise, the vector pair is discarded. Chord lengths are collected into a CLD. (Center) CLDs obtained for void space and solid phase of sample Si26 and the corresponding fits to the k-Gamma function (cf. eq 2.4). (Right) Topological skeleton. An iterative-thinning algorithm reduces the void space (or solid phase) to a medial axis of one-voxel thickness while conserving the topological properties. The local connectivity is the number of branches that meet at a junction.

panel in Figure 2.2)

$$f\left(l_{\mathrm{c}}\right)=\frac{k^{k}}{\Gamma(k)}\frac{l_{\mathrm{c}}^{k-1}}{\mu^{k}}\exp\left(-k\frac{l_{\mathrm{c}}}{\mu}\right) \tag{2.4}$$

In eq 2.4, l_{c} is the chord length, Γ is the Gamma function, μ is the first statistical moment, and $k=\mu^{2}/\sigma^{2}$ is the second statistical moment of the distribution. Values for μ and k obtained from fitting the CLD to the *k*-Gamma function are quantitative measures for average feature size and size homogeneity in the investigated space, respectively.[28]

Medial Axis Analysis

An iterative-thinning algorithm, available as ImageJ plug-in bundle (Skeletonize3D and AnalyzeSkeleton) was applied to reduce the void space (or solid phase) of a reconstruction to a medial axis of one-voxel thickness under conservation of the topological properties, as shown in the right panel of Figure 2.2. The average pore connectivity Z of the resulting topological skeleton was calculated as the average number of branches (pores) of the medial axis meeting at a node (junction) according to $Z=3n_{\mathrm{t}}/n_{\mathrm{j}}+4n_{\mathrm{q}}/n_{\mathrm{j}}+5n_{\mathrm{x}}/n_{\mathrm{j}}$, with $n_{\mathrm{x}}/n_{\mathrm{j}}=1-n_{\mathrm{t}}/n_{\mathrm{j}}-n_{\mathrm{q}}/n_{\mathrm{j}}$, where n_{j} is the total number of junctions, n_{t} is the number of triple-point junctions (connecting three branches), n_{q} the number of quadruple-point junctions (connecting four branches), and n_{x} the number of higher-order junctions (connecting five or more branches). Therefore, $n_{\mathrm{t}}/n_{\mathrm{j}}$, $n_{\mathrm{q}}/n_{\mathrm{j}}$, and $n_{\mathrm{x}}/n_{\mathrm{j}}$ give the fraction of nodes in the network connecting 3, 4, or >4 branches, respectively.

The branches of the medial axis network were characterized through the average value of the geometric branch tortuosity τ_{branch}, calculated as the average of all node-to-node network

distances $d_{\text{branch},i}$ over the Euclidean distances $d_{\text{euclid},i}$ between these nodes:

$$\tau_{\text{branch}} = \frac{1}{n}\sum_{i=1}^{n}\frac{d_{\text{branch},i}}{d_{\text{euclid},i}} \tag{2.5}$$

2.2.4 Geodesic Distance Propagation

The geodesic distance d_{geod} between two points in the void space is defined as the shortest path between them that does not cross the solid phase. We calculated the geodesic distance from a starting void voxel closest to the geometrical center of a reconstruction to all other void voxels employing Dijkstras shortest path algorithm (Figure 2.13 in the Supporting Information).[6] Each voxel was connected to 26 neighbours, excepting solid voxels, which were excluded from the analysis. A void voxel was treated as a vertex in a graph. The Euclidean distance was used as a weight of edges in this graph and could thus take only values of 1, $\sqrt{2}$, or $\sqrt{3}$. The global geometric tortuosity τ_{geom} is the ratio of d_{geod} to d_{euclid} for the case of sufficiently long geodesic distances

$$\tau_{\text{geom}} = \lim_{d_{\text{geod}}\to\infty}\frac{d_{\text{branch},i}}{d_{\text{euclid},i}} \tag{2.6}$$

where d_{euclid} is the Euclidean distance between starting and current voxel. For calculation of the global geometric tortuosity we used $\sim 10^6$ values per reconstruction (Figure 2.14). More information and the software download can be found elsewhere.[6]

2.2.5 Simulation of diffusion.

Accuracy, validation, and the program realization of the diffusion simulations by a random-walk particle-tracking (RWPT) technique[158,159] have previously been reported in detail,[33] which is why the approach is only briefly described here. A large number ($N = 5 \times 10^6$) of passive (i.e., nonadsorbing and nonreacting) tracer particles was initially distributed randomly and uniformly in the void space of a reconstructed volume (Figure 2.1). During each time step δt of the simulation, adjusted such that the mean diffusive displacement did not exceed $\Delta h/10$ (where Δh is the spatial resolution of a reconstruction), the displacement of every tracer due to random diffusive motion was calculated from a Gaussian distribution with zero mean and standard deviation $(2D_{\text{m}}\delta t)^{1/2}$ along each Cartesian coordinate. The passive interaction of the tracer particles with the pore walls was handled through a multiple-rejection boundary condition at the surface: when a tracer hit the impermeable wall during an iteration, the displacement was rejected and recal-

[6] K. Hormann et al. *New J. Chem.*, 40, 4187–4199, 2016.
[158] F. Delay, P. Ackerer, and C. Danquigny. *Vadose Zo. J.*, 4, 360–379, 2005.
[159] J. Salles et al. *Phys. Fluids A*, 5, 2348–2376, 1993.

culated until the tracer position was in the void space.[160–162] The accuracy of the RWPT-approach realized with the above boundary conditions was confirmed by comparing simulated values of the diffusion coefficient in regular arrays of spheres[29,143] with values calculated using the analytical approach.[163] After each time step, all tracer positions were recorded and a time-dependent diffusion coefficient evolved from

$$D\left(t\right) = \frac{1}{6N}\frac{\mathrm{d}}{\mathrm{d}t}\sum_{i=1}^{N}\left[\Delta r_i(t) - \langle \Delta r(t)\rangle\right]^2 \tag{2.7}$$

where $\Delta r_i(t) \equiv r_i(t) - r_i(0)$ and $\langle \Delta r_i(t)\rangle$ are the displacement of the *i*-th tracer and the average displacement of the tracer ensemble after time t, respectively. The normalized effective diffusion coefficients $D_{\text{eff,K}}/D_{\text{m}}$ were determined from the asymptotes of the normalized transient diffusion curves observed in the long-time limit. (Figure 2.15 in the Supporting Information illustrates the typical shape of the underlying transient $D(t)/D_{\text{m}}$-curves for sample Si12 at selected λ-values.)

In contrast to point-like tracers, which have access to the entire void space of a reconstruction, the void space accessible to finite-size tracers is smaller due to their steric interaction with the impermeable pore walls. For example, in the case of diffusion in a cylindrical pore, the center of a hard spherical tracer particle of diameter d_{tracer} is excluded from an annular region of thickness $d_{\text{tracer}}/2$ at the wall. In other words, the void space accessible to the center of a finite-size tracer becomes identical to the void space accessible to a point-like tracer if the pore diameter is reduced by d_{tracer}. An extension of the above isomorphism concept to random porous media was proposed by Torquato and co-worker.[164,165] According to this approach, the reduction of the accessible pore space for finite-size tracers can be accounted for by eroding the pore space accessible to point-like tracers with a structuring element of size d_{tracer}.[144] We implemented this mathematical morphology operation to generate the accessible mesopore space in the three reconstructions for the following d_{tracer}-values: 14 d_{tracer}-values increased in $0.7\,\text{nm}$ steps in the range $d_{\text{tracer}} = 0.7-9.8\,\text{nm}$ for sample Si12; 19 d_{tracer}-values increased in $1\,\text{nm}$ steps in the range $d_{\text{tracer}} = 1.0-19.0\,\text{nm}$ for sample Si21; and 21 d_{tracer}-values increased in $1\,\text{nm}$ steps in the range $d_{\text{tracer}} = 1.0-21.0\,\text{nm}$ for sample Si26. Afterwards, this information was imported into the RWPT-simulations to model the diffusion of passive tracers (of size d_{tracer}) in the three reconstructions. For each reconstructed volume and tracer size, these simulations delivered a value for the normalized local effective diffusivity and thus the local

[160] L. M. Schwartz, E. J. Garboczi, and D. P. Bentz. *J. Appl. Phys.*, 78, 5898–5908, 1995.
[161] L. M. Schwartz and J. R. Banavar. *Phys. Rev. B*, 39, 11965–11970, 1989.
[162] M. E. Kainourgiakis et al. *Transp. Porous Media*, 58, 43–62, 2005.
[29] H. Liasneuski et al. *J. Appl. Phys.*, 116, 034904, 2014.
[143] A. Daneyko et al. *J. Chromatogr. A*, 1407, 139–156, 2015.
[163] M. H. Blees and J. C. Leyte. *J. Colloid Interface Sci.*, 166, 118–127, 1994.
[164] S. Torquato. *J. Chem. Phys.*, 95, 2838–2841, 1991.
[165] I. C. Kim and S. Torquato. *J. Chem. Phys.*, 96, 1498–1503, 1992.
[144] H. Koku et al. *J. Chromatogr. A*, 1237, 55–63, 2012.

hindrance factor $K_{\mathrm{d}}(\lambda) = D_{\mathrm{eff,K}}(\lambda)/D_{\mathrm{m}}$. The local parameters are related to the respective global parameters $D_{\mathrm{eff,H}}(\lambda)$ and $H(\lambda)$ through the accessible porosity $\varepsilon(\lambda)$: $D_{\mathrm{eff,H}}(\lambda) = \varepsilon(\lambda) D_{\mathrm{eff,K}}(\lambda)$ and $H(\lambda) = D_{\mathrm{eff,H}}(\lambda)/D_{\mathrm{m}} = \varepsilon(\lambda) D_{\mathrm{eff,K}}(\lambda)/D_{\mathrm{m}} = \varepsilon(\lambda) K_{\mathrm{d}}(\lambda)$. The value of the accessible porosity ε at a given value of λ was available as the void volume fraction of an eroded pore space at this λ.

The program realization of the RWPT-algorithm was implemented as a parallel code in C language using the Message Passing Interface (MPI) standard on a supercomputing platform at the Jülich Supercomputing Center (JSC, Forschungszentrum Jülich, Germany). All numerical codes and their description can be found in the Supporting Information of ref.[33]

2.3 Results and discussion

2.3.1 Physical reconstruction and morphological evaluation of the mesoporous silica samples.

Figure 2.1 shows the physical reconstructions that were obtained by STEM tomography of the microscopically disordered mesopore space of the three macro–mesoporous silica monoliths. As chromatographic columns, for example, the three monoliths would be suitable for small molecules (Si12, $d_{\mathrm{meso}} = 12.3\,\mathrm{nm}$), peptides (Si21, $d_{\mathrm{meso}} = 21.3\,\mathrm{nm}$), or small proteins (Si26, $d_{\mathrm{meso}} = 25.7\,\mathrm{nm}$). The following analysis focuses on determining the relevant morphological characteristics of each sample and on establishing the reconstructions as valid models for the simulation of hindered diffusion. We begin by determining geometrical properties of the reconstructed mesopore spaces by CLD analysis (Figure 2.2). This type of analysis returns two parameters: μ as the first statistical moment of the distribution, and k as a second-moment parameter related to the width of the distribution, defined by μ and the standard deviation σ as $k = \mu^2/\sigma^2$. The value for μ is equivalent to the mean chord length and thus a measure of the mean feature size. The value for k indicates the homogeneity of the feature size over the geometrical range of locally generated chord lengths. Figure 2.2 shows that CLD analysis (as well as medial axis analysis) can in principle also be used to characterize the morphological properties of the solid phase.

Prior to extracting global geometrical properties from the reconstructed volumes, we had to ascertain that their dimensions were sufficient to represent the global morphology of the mesoporous silica samples. To ensure the absence of finite-size effects in the extracted μ- and k-values,[166] we performed CLD analyses in subvolumes of the reconstructions. Figure 2.3 shows the results obtained for the sample with the largest feature size, Si26, by plotting the values for μ and k that were obtained with eq 2.4 from CLDs generated in cuboids of increasing edge lengths. For small edge lengths, the data scatter as expected, but at $\sim 70\,\%$ of the full edge lengths (which corresponds to about $34\,\%$ of the total reconstructed volume) μ and k approach constant values. The finite-size analysis for the μ- and k-values of samples Si12 and Si21 gave comparable results, so that the physical reconstructions shown in Figure 2.1 can be considered

[166] T. Müllner et al. *Mater. Today*, 17, 404–411, 2014.

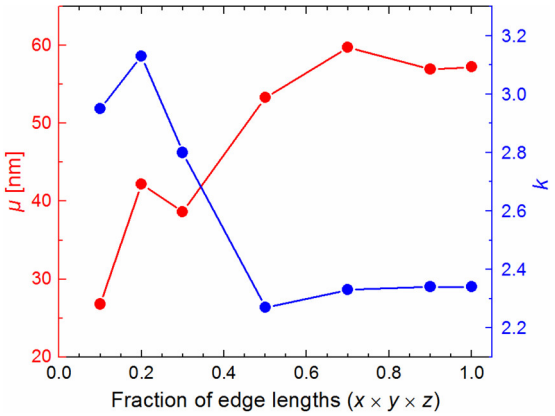

Figure 2.3: Analysis of finite-size effects in the reconstructed void space of sample Si26. Values for μ (mean chord length) and k (homogeneity factor) were obtained with eq 2.4 from CLDs generated in subvolumes of the reconstruction.

as representative of the monoliths' mesopore space and therefore as suitable for the derivation of global morphological properties and diffusive mass transport characteristics.

Figure 2.4 and Table 2.1 contain the results of the CLD analysis performed on the entire void space of each reconstruction. Apart from the μ- and k-values obtained with eq 2.4, the mode of each CLD is also given. The mode indicates the length scale on which structural order exists in a material that exihibts correlated disorder,[130] such as amorphous silica formed in a sol–gel process. Table 2.1 compares the geometrical data derived by CLD analysis of the reconstructions with values for the mean mesopore diameter (d_{meso}) and the specific surface area (A_{spec}) obtained by nitrogen physisorption analysis of the mesoporous silica samples (Figure 2.12). The values for μ and the mode confirm that the mean feature size of the mesopore space increases from sample Si12 to Si21 to Si26, as indicated by the d_{meso}-values. The data from CLD analysis are not necessarily equivalent to d_{meso}, because CLD analysis is not tied to any specific pore geometry, whereas the conversion of nitrogen physisorption data into pore diameters requires a specific pore model, in this case a cylinder. For an infinitely long cylinder the mode of the CLD corresponds to the cylinder diameter.[167] The three samples show a nearly constant relation of ~ 1.2 between the mode and d_{meso} and of ~ 2.2 between μ and d_{meso}. The former confirms the cylindral pore model for the derivation of d_{meso} as suitable, the latter encourages the use of d_{meso} for normalizing the chord lengths l_{c}. The normalized CLDs (inset in Figure 2.3) overlap nearly perfectly, which indicates that d_{meso} and chord length characteristics are linearly scaled among the three samples. This is an important result, because it allows the experimentally accessible parameter d_{meso} to define $\lambda = d_{\text{tracer}}/d_{\text{meso}}$ in the subsequent simulations of hindered diffusion.

To determine the topological properties of the reconstructed mesopore spaces, we used medial axis analysis (Figure 2.2) and geodesic distance propagation (eq 2.6 and Figures 2.13 and 2.14 in the Supporting Information). The right panel in Figure 2.2 visualizes the branch–

[130] P. Levitz and D. Tchoubar. *J. Phys. I*, 2, 771–790, 1992.
[167] W. Gille, D. Enke, and F. Janowski. *J. Porous Mater.*, 8, 179–191, 2001.

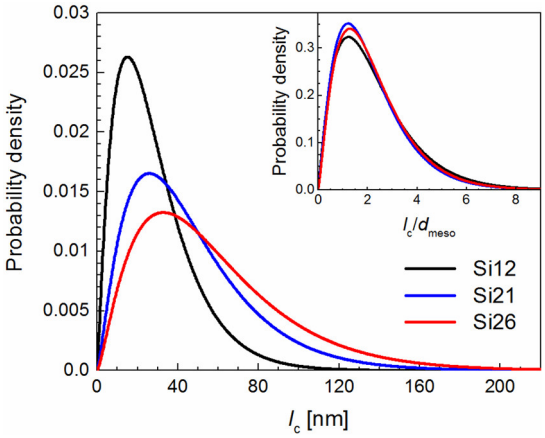

Figure 2.4: CLDs obtained for the void space of the three reconstructions. (Inset) CLDs normalized by the mean mesopore size (d_{meso}) of the mesoporous silica samples as determined by nitrogen physisorption analysis (cf. Figure 2.12).

node network resulting from application of a thinning algorithm that reduces the pore space to a medial axis of one-voxel thickness while the topology is conserved. The number of branches that originate from a junction (a node of the medial axis) quantifies the local branch connectivity, interpreted as the local pore connectivity. According to Table 2.2, which lists the percentages of nodes connecting 3, 4, or > 4 branches and the resulting average pore connectivity (Z), the three mesopore spaces share a highly similar distribution of the local pore connectivity. $85{-}88\,\%$ of junctions connect three branches (the minimal number of branches that defines a junction), about $11\,\%$ of junctions connect four branches, higher-order junctions are rare ($\sim 2\,\%$). The average pore connectivity of $Z \approx 3$ therefore reflects the typical junction in the disordered mesopore spaces. We also calculated the average branch tortuosity τ_{branch} (eq 2.5) from the medial axis network and determined the global geometric tortuosity τ_{branch} (eq 2.6) by geodesic distance propagation for each reconstruction (Table 2.3). Because the medial axis path d_{branch} between points A and B is longer than the geodesic distance d_{geod} (top panel in Figure 2.13), the average branch tortuosity ($\tau_{\text{branch}} \approx 1.2$) is larger than the global geometric tortuosity ($\tau_{\text{geom}} \approx 1.1$). As observed for the pore connectivity, the three reconstructed mesopore spaces are practically undistinguishable with regard to their branch and geometric tortuosities.

The final part of the morphological evaluation builds a transition to the subsequent pore-

Table 2.1: Geometrical properties of the mesoporous silica samples.

	Si12	Si21	Si26
μ [nm][a]	28.3	45.7	57.2
mode [nm][a]	15.0	25.5	32.4
k [−][a]	2.13	2.29	2.34
d_{meso} [nm][b]	12.3	21.3	25.7
A_{spec} [$\text{m}^2\,\text{g}^{-1}$][b]	315.7	173.8	129.6

[a]From CLD analysis of the void space of the reconstructed mesopore spaces.
[b]From nitrogen physisorption analysis (cf. Figure 2.12).

Table 2.2: Connectivities of the topological skeleton of the reconstructed mesopore spaces.[a]

	Si12	Si21	Si26
n_t/n_j [%]	85.6	87.6	86.6
n_q/n_j [%]	11.8	10.6	11.3
n_x/n_j [%]	2.6	1.8	2.0
Z	3.17	3.14	3.15

[a]Percentage of nodes connecting 3, 4, or > 4 branches (n_t/n_j, n_q/n_j, and n_x/n_j, respectively) as well as the resulting average pore connectivity (Z).

scale simulations of hindered diffusion by discussing the diffusive tortuosity τ_0 and the porosity ε_0 of the reconstructed mesopore spaces (Table 2.3). The diffusive tortuosity $\tau_0 = D_m/D_{eff,K}(\lambda = 0)$ was determined from pore-scale simulations of the diffusion of point-like tracers ($d_{tracer} = 0$ and thus $\lambda = d_{tracer}/d_{meso} = 0$) in the reconstructions. This parameter accounts inherently for the overall effect of the pore space morphology on diffusive transport of tracers, in contrast to the geometric tortuosity, which characterizes only the sinuousness of transport pathways without considering other relevant morphological properties of the pore space (e.g., the nonuniformity in the local size of pores or local "bottleneck" configurations). The comparison of τ_{geom} and τ_0 (Table 2.3) raises two points. First, the diffusive tortuosity is larger than the geometric tortuosity ($\tau_0 > \tau_{geom}$), because point-like tracers diffusing through the mesopore space experience more obstruction than expected from the geometric tortuosity values, since Brownian motion leads tracers to deviate from the ideal (geodesic) route. The geometric tortuosity value should be considered as a lower bound. Second, contrary to the constant τ_{geom}-values, the τ_0-values decrease (i.e., the $D_{eff,K}$-values increase) from sample Si12 to Si26, which is a consequence of the different porosities of the samples. The porosity ε_0, calculated as the fraction of void voxels in a reconstruction, increases along with d_{meso} from $\sim 58\,\%$ (Si12) over $\sim 65\,\%$ (Si21) to $\sim 70\,\%$ (Si26). A higher porosity, in turn, results in a lower diffusive tortuosity.[28] The geometric tortuosity (τ_{geom}), which does not reflect any actual mass transport, remains unaffected by the different porosities, because the pore network topology is excellently conserved among the three samples. It is noteworthy that the insufficiency of using only τ_{geom} to describe adequately transport phenomena in porous media was already revealed by numerical and experimental investigations of

Table 2.3: Tortuosities and void volume fraction of the reconstructed mesopore spaces.

	Si12	Si21	Si26
τ_{branch}[a]	1.20	1.20	1.19
τ_{geom}[b]	1.13	1.13	1.10
τ_0[c]	1.67	1.45	1.35
ε_0[d]	0.577	0.649	0.702

[a]From medial axis analysis (cf. eq 2.5).
[b]From geodesic distance propagation (cf. eq 2.6 and Figures 2.13 and 2.14).
[c]From simulations of diffusion with point-like tracers.
[d]Void voxel fraction of a reconstruction.

computer-generated[168] and physically reconstructed porous structures.[169] Therefore, we use the geometric tortuosity in our work exclusively for morphological analysis of the mesoporous silica samples.

The comprehensive morphological evaluation of the three reconstructed mesopore spaces supports the hypothesis that the postgelational, hydrothermal treatment produces very little changes in the then-existing morphology of the macro–microporous wet gels beyond enlarging micropores to mesopores by removal of silica mass. The data in Tables 2.1-2.3 and Figure 2.4 show that the three mesoporous silica samples differ in pore size and porosity, but not in pore shape and topology; they also retain homogeneous structures on length scales larger than the mean pore size, as indicated by the k-values. In these respects, the mesoporous silica samples resemble the well-known controlled pore glasses.[67,170] The three reconstructed mesopore spaces therefore define a consistent set of model structures to test the scalability of hindered diffusion with respect to d_{meso} and the value of λ.

2.3.2 Pore-scale simulations of hindered diffusion.

For simulations of hindered diffusion in the reconstructed mesopore spaces we used d_{tracer}-values between 0.7 and $21.0\,\text{nm}$, whereby range and intervals were adapted to the respective d_{meso}-value of a sample, as described in the Experimental Section. Figure 2.5A summarizes the primary data obtained from the simulations, plotted as $D_{\text{eff,K}}/D_{\text{m}}$ as a function of d_{tracer}, plus the values for point-like tracers ($d_{\text{tracer}} = 0$) obtained from simulations of obstructed diffusion in the reconstructed mesopore spaces. The mobilities in Figure 2.5A cover the range from $D_{\text{eff,K}}/D_{\text{m}} = 1/\tau_0$ to ~ 0.01. Figure 2.5B compares hindered diffusion in the three reconstructions by displaying the data in dimensionless form. Plotted as $D_{\text{eff,K}}(\lambda)/D_{\text{eff,K}}(\lambda = 0)$ as a function of λ, the data neatly collapse onto a single curve that characterizes hindered diffusion in the disordered mesopore spaces for the range $0 \leq \lambda \leq 0.9$. We quantified this information by a least-squares fit to the full data set in Figure 2.5B and obtained the following expression for the local hindrance factor $K_{\text{d}}(\lambda)$:

$$\begin{aligned} K_{\text{d}}(\lambda) &= \frac{D_{\text{eff,K}}(\lambda)}{D_{\text{m}}} \\ &= \frac{D_{\text{eff,K}}(\lambda)}{D_{\text{eff,K}}(\lambda = 0)\tau_0} \\ &= \frac{1}{\tau_0}\left(1 - 1.216\lambda - 0.58\lambda^2 - 5.199\lambda^3 + 13.350\lambda^4 - 7.455\lambda^5\right) \end{aligned} \tag{2.8}$$

This equation captures the data remarkably well and therefore allows a precise prediction of the local effective diffusion coefficients in mesoporous silica from the knowledge of tracer size, mean mesopore size, and the diffusive tortuosity. Because eq 2.8 was obtained from simulations within

[168] G. Gaiselmann et al. *AIChE J.*, 60, 1983–1999, 2014.
[169] D. Wiedenmann et al. *AIChE J.*, 59, 1446–1457, 2013.
[170] P. Levitz et al. *J. Chem. Phys.*, 95, 6151–6161, 1991.

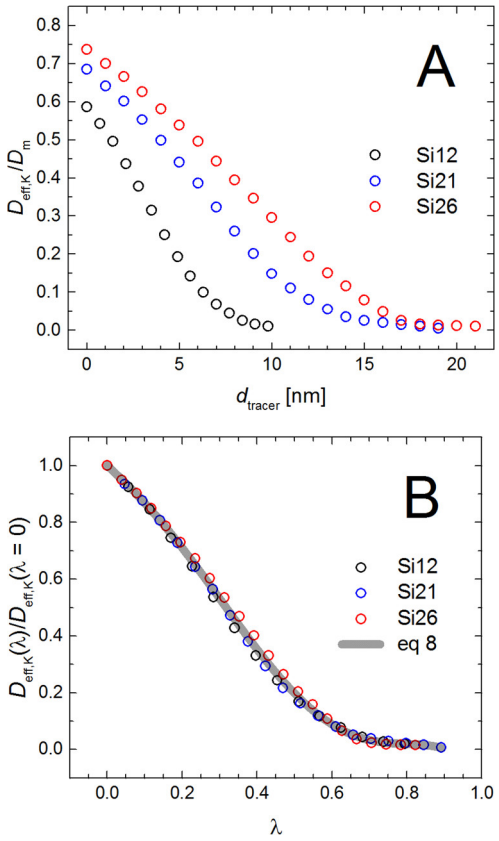

Figure 2.5: Simulations of tracer diffusion in the three reconstructions. (A) Local effective diffusion coefficient $D_{\mathrm{eff,K}}$, normalized by the free diffusion coefficient in the bulk liquid D_{m}, as a function of the tracer size d_{tracer}. (B) Local effective diffusion coefficient $D_{\mathrm{eff,K}}(\lambda)$, normalized by the effective diffusivity of point-like tracers (i.e., $D_{\mathrm{eff,K}}(\lambda = 0) = D_{\mathrm{m}}/\tau_0$), as a function of $\lambda = d_{\mathrm{tracer}}/d_{\mathrm{meso}}$, the ratio of tracer to mean mesopore size. The gray curve displays the expression for $K_{\mathrm{d}}(\lambda)\tau_0$ derived from the entire data set (eq 2.8); the respective τ_0-values are given in Table 2.3.

the mesopore space, the effective diffusive tortuosity of the mesopore space is already inherently included in the derived expression for $K_{\mathrm{d}}(\lambda)$.

To get from $K_{\mathrm{d}}(\lambda)$ to the overall hindrance factor $H(\lambda)$, we additionally needed an expression for the accessible porosity, $\varepsilon(\lambda)$, that is, the fraction of ε_0 that is accessible to tracers of a given size. Because our approach was to erode the pore space accessible to point-like tracers with a structuring element of size d_{tracer},[33] the value for ε at a given $\lambda = d_{\mathrm{tracer}}/d_{\mathrm{meso}}$ was easily available as the void volume fraction of the eroded pore space at the respective d_{tracer}-value. Figure 2.6 summarizes the accessible porosity data obtained for the three reconstructions by displaying $\varepsilon(\lambda)$, normalized by the porosity value for point-like tracers ($\varepsilon(\lambda = 0) \equiv \varepsilon_0$, Table 2.3), as a function of λ. As observed for the local hindered mobilities in Figure 2.5B, the accessible porosity data also collapse onto a single curve. A least-squares fit to the full data set yielded the following

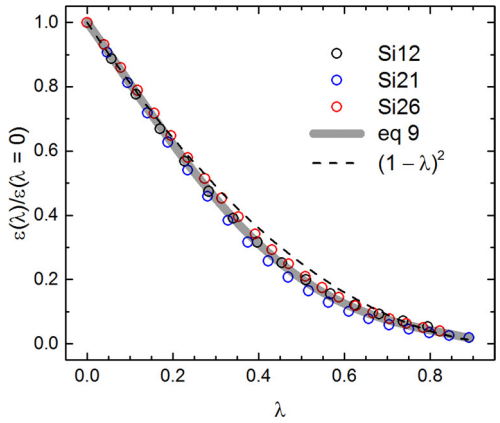

Figure 2.6: Void volume fractions experienced by different-sized tracers in the three reconstructions. Accessible porosity $\varepsilon(\lambda)$, normalized by the porosity accessible to point-like tracers (i.e., $\varepsilon(\lambda) \equiv \varepsilon_0$, cf. Table 2.3), as a function of $\lambda = d_{\text{tracer}}/d_{\text{meso}}$, the ratio of tracer to mean mesopore size. The gray curve displays the expression derived for $\varepsilon(\lambda)$ from the entire data set (eq 2.9). The dashed line indicates the factor used in the Renkin equation (eq 2.1) in place of $\varepsilon(\lambda)$.

expression for $\varepsilon(\lambda)$:

$$\frac{\varepsilon(\lambda)}{\varepsilon(\lambda = 0)} = 1 - 2.200\lambda + 1.245\lambda^2 \tag{2.9}$$

Interestingly, eq 2.9 is still reminiscent of the respective expression $\varepsilon(\lambda)/\varepsilon_0 = (1-\lambda)^2$ used by Wernert et al.[63] and based on the Renkin equation (eq 2.1).[62] This similarity shows that the true mesopore shape of the monoliths is not so far removed from a cylinder, although this cannot be recognized from a visual inspection of the physical reconstructions in Figure 2.1. While the cylinder is a good approximation of the mesopore shape when a simple geometrical model is needed, as for the routine conversion of physisorption data into pore size distributions, the true mesopore shape is better described as a subtly twisted tube of somewhat varying diameter.

From combining eqs 2.8 and 2.9 we finally obtained a quantitative expression for the global diffusive hindrance factor $H(\lambda)$:

$$\begin{aligned} H_(\lambda) &= \frac{D_{\text{eff,H}}(\lambda)}{D_{\text{m}}} \\ &= \varepsilon(\lambda) K_{\text{d}}(\lambda) \\ &= \frac{\varepsilon_0}{\tau_0}\left(1 - 3.416\lambda + 3.338\lambda^2 - 5.433\lambda^3 + 24.063\lambda^4 - 43.298\lambda^5 + 33.022\lambda^6 - 9.282\lambda^7\right) \end{aligned} \tag{2.10}$$

To evaluate the derived expression for the global hindrance factor, we returned to the simulated

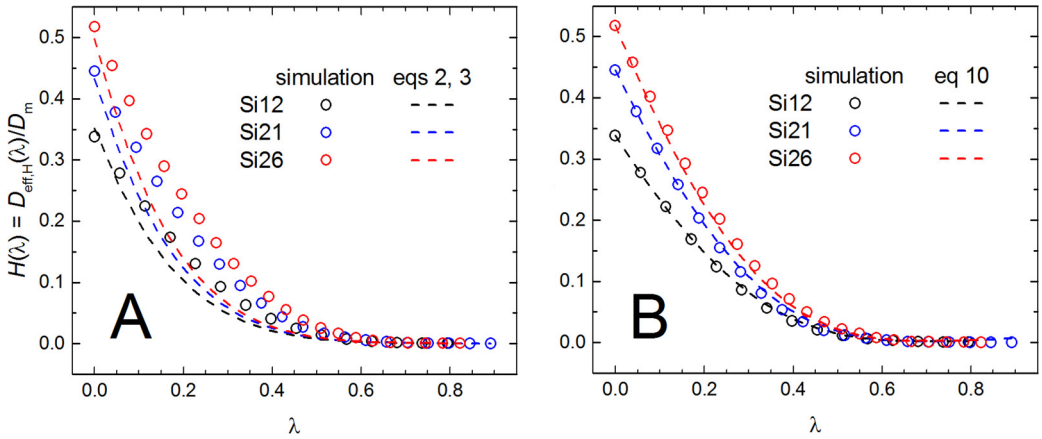

Figure 2.7: Dependence of the overall diffusive hindrance factor $H(\lambda)$ on $\lambda = d_{\text{tracer}}/d_{\text{meso}}$, the ratio of tracer to mean mesopore size, in the three reconstructions. Comparison of the simulation-based $H(\lambda)$-data (A) with model predictions based on eqs 2.2 and 2.3 (using $p = 1.16$ and ε_0 from Table 2.3) and (B) with eq 2.10 (using ε_0 and τ_0 from Table 3).

data. From the data sets for $D_{\text{eff,K}}(\lambda)$ and $\varepsilon(\lambda)$, the respective global values for each reconstruction were calculated through $D_{\text{eff,H}}(\lambda) = \varepsilon(\lambda)D_{\text{eff,K}}(\lambda)$ and $H(\lambda) = D_{\text{eff,H}}(\lambda)/D_{\text{m}}$. Figures 2.7 panels A and B show the three $H(\lambda)$-data sets compared with predictions based on the model of Wernert et al.[63] (eqs 2.2 and 2.3) and with our global hindrance factor expression (eq 2.10), respectively. Figure 2.7B visualizes very well that the $H(\lambda)$-curves have the largest slope and also the largest divergence from each other at low-to-medium λ-values. At $\lambda > 0.4$, the $H(\lambda)$-curves start to approach the asymptote of $H(\lambda) \approx 0$. For comparison with the model of Wernert et al.,[63] we followed their procedure to determine the pore space topology parameter p. We fitted the τ_0–ε_0 data pairs obtained for the three reconstructions (Table 2.3) to eq 2.3 (with $\lambda = 0$) and received a value of $p = 1.16$. Figure 2.7A shows that the model of Wernert et al.[63] captures the general form of the $H(\lambda)$-curves reasonably well, but substantially underestimates the data in the critical low-to-medium range ($0.1 \leq \lambda \leq 0.4$). At $\lambda \approx 0.23$, for example, the simulation-based values are $H(\lambda) = 0.130$ for sample Si12, $H(\lambda) = 0.165$ for sample Si21, and $H(\lambda) = 0.204$ for sample Si26; the model of Wernert et al.[63] predicts values of $H(\lambda) = 0.084$ (Si12), $H(\lambda) = 0.095$ (Si21), and $H(\lambda) = 0.107$ (Si26), that is, it underestimates the data by a factor of 1.55, 1.73 and 1.90, respectively.

The possible source of this divergence lies in eq 2.3. The diffusive tortuosity–porosity relationship $\tau(\lambda)$–$\varepsilon(\lambda)$ for a random porous medium should adequately describe (i) the morphological effects of a complex pore network on diffusive mass transport;[28] and (ii) the exact dependence of these interrelationships on λ, which presents a major challenge. Wernert et al.[63] approached this problem with the modified Weissberg equation with a fitting parameter p, a sensible choice given the success of the Weissberg equation. Weissberg originally derived the equation (with $p = 0.5$) on a theoretical basis as a lower bound for the diffusive tortuosity in random

arrangements of freely overlapping spheres, that is, for a specific model structure.[171] Traditionally, diffusive tortuosity–porosity correlations are tested against self-similar materials, which can be prepared with varied mean pore size and porosity without inducing major accompanying changes in topology.[172–174] Simply speaking, this means that pores can be made larger or smaller, but the pathways between them are not altered. A good example for self-similar materials are fluidized beds of hard particles undergoing a stepwise densification to form first loose and finally dense packings.[173] The relatively smooth densification process leaves the topological properties of the pore network largely unaffected. The macro–mesoporous silica monoliths used in this work are also self-similar materials, as proven by the morphological analysis. This is why applying eq 2.6 to the τ_0–ε_0 data pairs obtained for samples Si12, Si21, and Si25 yielded rather consistent p-values ($p = 1.22, 1.04, 0.99$), which could be approximated with the fitted value of $p = 1.16$. Diffusive tortuosity–porosity correlations valid for point-like tracers in self-similar materials, however, do not necessarily account for the topological evolution of a given material that is experienced by different-sized tracers.

How different the same material can look to point-like and finite-size tracers is visualized in Figure 2.8, which shows the accessible porosity $\varepsilon(\lambda)$ in the reconstructed mesopore space of sample Si12 for four different λ-values. As the accessible void volume fraction decreases with increasing λ, the available pore network thins out as whole pathways are closed off. To quantify the changes in pore space topology experienced by different-sized tracers, we determined the fraction of triple-point and quadruple-point junctions in the available pore networks for $0 \leq \lambda \leq 0.9$. Figure 2.9 shows the dramatic decline of the pore connectivity with increasing tracer size. At $\lambda = 0.4$, the number of triple-point and quadruple-point junctions has dropped to $\sim 60\,\%$ and $\sim 50\,\%$, respectively, of its original value for $\lambda = 0$. This means that the decrease of $D_{\text{eff,K}}(\lambda)$ and $H(\lambda)$ (Figures 2.5 and 2.7, respectively) reflects the removal of entire branches from the pore network and thus complex topological changes in the accessible pore space. Contrary to the self-similar structures of the three mesoporous samples (Figure 2.1), the pore networks available for different λ-values (Figure 2.8) are not connected through a straightforward relationship. For macro–mesoporous silica monoliths, the morphological changes that accompany an increasing tracer size are more substantial than the morphological changes caused by varying the hydrothermal treatment step in monolith synthesis.

The three-step approach (physical reconstruction/morphological analysis/pore-scale simulations) we developed in this work can be applied to derive global hindrance factor expressions also for other types of porous media. To arrive at this expression, one needs (as was shown above) to account for changes with λ of both the local hindrance factor $K_{\text{d}} = D_{\text{eff,K}}/D_{\text{m}}$ and the accessible porosity. A reduction of $D_{\text{eff,K}}$ with λ was already confirmed by experimental studies and nu-

[171] H. L. Weissberg. *J. Appl. Phys.*, 34, 2636–2639, 1963.
[172] P. Y. Lanfrey, Z. V. Kuzeljevic, and M. P. Dudukovic. *Chem. Eng. Sci.*, 65, 1891–1896, 2010.
[173] M. Barrande, R. Bouchet, and R. Denoyel. *Anal. Chem.*, 79, 9115–9121, 2007.
[174] S. Khirevich et al. *J. Chromatogr. A*, 1218, 6489–6497, 2011.

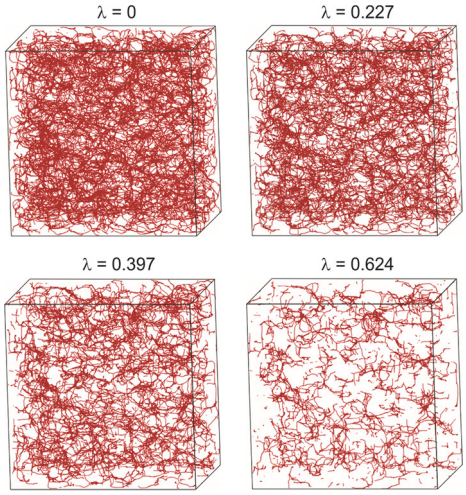

Figure 2.8: Visualization of the available pore network for different-sized tracers in the reconstructed mesopore space of sample Si12 ($d_{\text{meso}} = 12.3\,\text{nm}$). The accessible porosity $\varepsilon(\lambda)$ decreases with $\lambda = d_{\text{tracer}}/d_{\text{meso}}$, the ratio of tracer to mean mesopore size, as $\varepsilon(\lambda = 0) \equiv \varepsilon_0 = 0.577$, $\varepsilon(\lambda = 0.227) = 0.327$, $\varepsilon(\lambda = 0.397) = 0.182$, and $\varepsilon(\lambda = 0.624) = 0.069$.

merical simulations of diffusion in various porous media, such as controlled pore glasses,[67,175,176] Vycor porous glasses,[177,178] and random packings of particles.[179] For example, Guo et al.[177] employed dynamic light scattering to measure the effective diffusion coefficient of polystyrenes with different molecular weights in Vycor 7930 glass. The internal surface of the Vycor glass was pretreated to replace active hydroxyl groups with alkyl groups and minimize adsorption. A similar experimental approach was followed by Kluijtmans et al.[176] in a systematic study of the effective diffusion coefficient of uncharged colloidal silica particles in controlled pore glasses. Combining glasses with three different mean pore radii and silica particles with four different diameters, the authors determined the effective diffusion coefficient for λ-values in the range from 0.08 to 0.6. In Figure 2.10, we compare the experimental results reported in the two mentioned papers for porous glasses (symbols) with our results for the mesoporous silicas (grey curve). Since the porosity ε_0 of the glasses studied in refs [176] and [177] was different, we applied to the experimental data (reported as plots of $D_{\text{eff,K}}/D_{\text{m}}$ vs λ) the same approach we used to unify our data in Figure 2.5B for the three silica samples with different porosities. For that purpose, the experimental data were multiplied by the tortuosity τ_0, estimated for similar materials as ~ 1.28.[175] Like in Figure 2.5B, the grey curve in Figure 2.10 displays the expression for $K_{\text{d}}(\lambda)\tau_0$ derived from the data set for the mesoporous silicas (eq 2.8). Though the data in Figure 2.10 indicate some difference in the functional dependence of the local hindrance factor on λ for the sol–gel based silicas and the porous glasses, the general agreement is rather good. On the other

[175] M. T. Bishop, K. H. Langley, and F. E. Karasz. *Macromolecules*, 22, 1220–1231, 1989.
[176] S. G.J. M. Kluijtmans, J. K. G. Dhont, and A. P. Philipse. *Langmuir*, 13, 4982–4987, 1997.
[177] Y. Guo, K. H. Langley, and F. E. Karasz. *Phys. Rev. B*, 50, 3400–3403, 1994.
[178] M. E. Kainourgiakis et al. *J. Chem. Phys.*, 111, 2735–2743, 1999.
[179] S. G.J. M. Kluijtmans and A. P. Philipse. *Langmuir*, 15, 1896–1898, 1999.

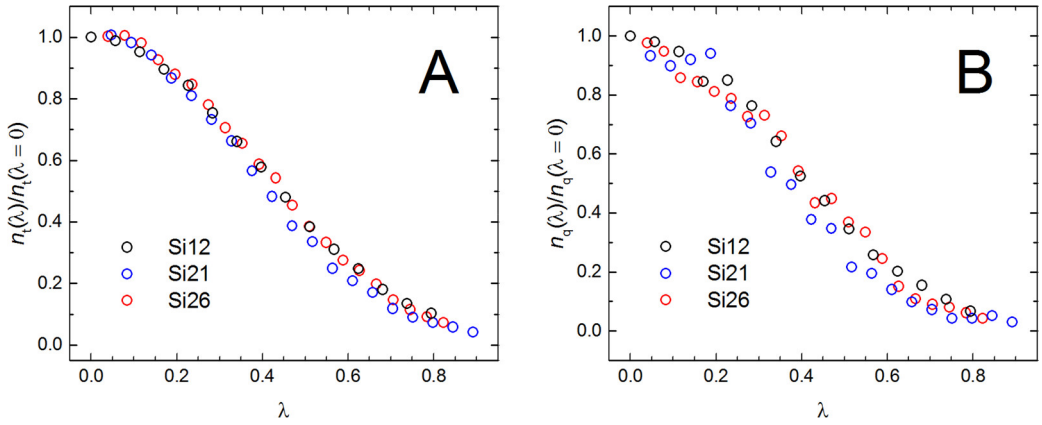

Figure 2.9: Tracer-size dependent evolution of the topological skeleton in the three reconstructions. Relative population of nodes in the branch–node network connecting three (n_t, panel A) or four branches (n_q, panel B) as a function of $\lambda = d_{tracer}/d_{meso}$, the ratio of tracer to mean mesopore size. Absolute numbers of triple-point and quadruple-point junctions are normalized by the corresponding values for point-like tracers.

hand, this agreement does not mean that eq 2.10 can immediately be applied to determine the global hindrance factor for the glasses. To arrive at an adequate expression for $H(\lambda)$ for these materials, one needs to know how the accessible porosity changes with λ. This information can be obtained only after physical reconstruction followed by morphological analysis.

2.4 Conclusions

Through an approach consisting of an informed selection of mesoporous silica samples, their physical reconstruction by STEM tomography, and pore-scale simulations of the diffusion of different-sized tracers in the reconstructions providing long-time, effective diffusion coefficients in dependence of λ, the ratio between tracer and mean mesopore size, over $0 \leq \lambda \leq 0.9$, we have derived an expression for the overall diffusive hindrance factor. The derived expression allows precise predictions about the extent of hindered diffusion from reliable values for the material parameters D_m, d_{meso}, ε_0, and τ_0. D_m can be estimated experimentally or from established correlations, d_{meso} is derived from standard physisorption measurements, and ε_0 and τ_0 are also conveniently accessible by experiment.[63] Predicting the hindrance factor could improve the performance of mesoporous silica adsorbents in their various applications. Smaller mesopores increase the surface area and therefore the capacity (mass loadability), but carry the risk of hindered diffusion. The presented expression for the diffusive hindrance factor allows to find the optimum mesopore size for a given range of solute sizes, either to maximize effective diffusivities or to identify an acceptable compromise between transport limitations and mass loadability, which also includes adjustments of particle porosity (ε_0).

Our results have shown that simple models and equations based on self-similar structures are inadequate concepts to describe hindered diffusion in random porous media. Because the structures evolving from a given mesopore space at different λ-values are not self-similar, their

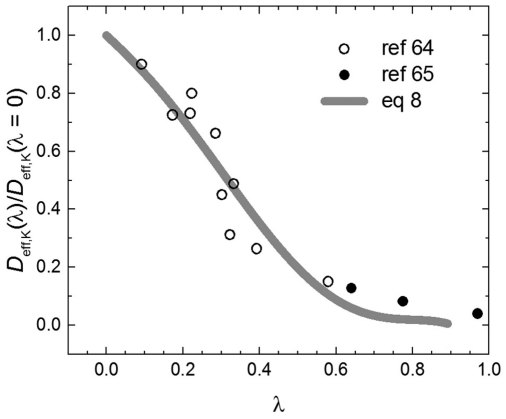

Figure 2.10: Comparison between the local effective diffusion coefficient $D_{\mathrm{eff,K}}(\lambda)$, normalized by the effective diffusivity of point-like tracers (i.e., $D_{\mathrm{eff,K}}(\lambda = 0) = D_{\mathrm{m}}/\tau_0$), as a function of $\lambda = d_{\mathrm{tracer}}/d_{\mathrm{meso}}$, the ratio of tracer to mean mesopore size. Experimental data for controlled pore glasses[176] (open circles) and Vycor 7930 glass[177] (solid circles) are compared with our simulated data for the sol–gel based mesoporous silicas represented by the gray curve.

evolution cannot be predicted by a generic diffusive tortuosity–porosity relationship. Precise predictions of diffusive hindrance factors require an explicit consideration of the morphology–transport relationships in a material. The presented expression for the diffusive hindrance factor is the first equation derived for a random porous medium based on its reconstructed morphology. We expect the equation to hold for mesoporous silica with similar morphology as the investigated samples. Assuming that the morphology of a material is determined by its preparation process, the derived equation has the potential to describe hindered diffusion in all mesoporous silica materials obtained through sol–gel processing, which would include the mesoporous silica particles used for packed beds. A comprehensive, spatiotemporally resolved analysis of transport in hierarchically porous materials, such as the studied silica monoliths or packed beds of porous silica particles, could become possible in the future through the proper implementation of fluid flow, adsorption, and reaction in pore-scale simulations, which explicitly include, for example, the diffusion-limited mass transfer of (finite-size) tracers between flowing and stagnant regions,[143] or the adsorption sojourn time distribution of an analyte.[180]

Acknowledgements

This work was supported by the Deutsche Forschungsgemeinschaft DFG (Bonn, Germany) under grant TA 268/9–1 and by the Karlsruhe Nano Micro Facility (KNMF) at the Karlsruhe Institute of Technology (Karlsruhe, Germany) under the KNMF long-term user proposal 2015-014-008069. We thank the John von Neumann Institute for Computing (NIC) and the Jülich Supercomputing Center (JSC), Forschungszentrum Jülich (FZJ, Jülich, Germany), for the allocation of a special CPU-time grant (NIC Project No. 10214, JSC Project ID HMR10).

[180] D. Hlushkou et al. *Anal. Chem.*, 86, 4463–4470, 2014.

2.5 Supporting information

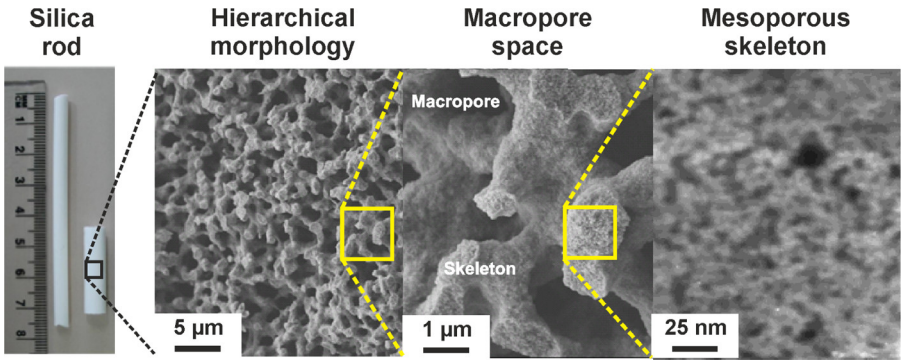

Figure 2.11: Hierarchical pore space morphology of macro–mesoporous silica monoliths (adapted from Stoeckel et al.[14]). The macropores form an interskeleton network of flow-through channels, dedicated to advection-dominated fluid transport through the monolith, usually by pressuredriven flow. Mass transfer in the intraskeleton mesopores is diffusion-limited.

Nitrogen Physisorption Analysis. Because the monoliths were received as columns for reversed-phase chromatography, the bonded phase (C_{18} chains and endcapping groups) had to be removed from the silica surface. This was done through thermal decomposition under nitrogen atmosphere. The monoliths were placed in an oven, whose temperature was raised to $350\,^{\circ}\mathrm{C}$ over $15\,\mathrm{h}$ and kept at that value for $30\,\mathrm{h}$. After slowly returning to room temperature, the temperature was raised again to $450\,^{\circ}\mathrm{C}$ and kept at that value for $6\,\mathrm{h}$. The resulting bare-silica monoliths were then evacuated for $16\,\mathrm{h}$ at $120\,^{\circ}\mathrm{C}$ prior to nitrogen physisorption analysis at $77\,\mathrm{K}$ on an automated gas adsorption station (QUADRASORB evo, Quantachrome Corporation, Boynton Beach, FL). The mesopore size distributions were derived from the adsorption branches of the nitrogen sorption isotherms (Figure 2.12) using the non-local density functional theory (NLDFT) method with a cylindrical pore model.[93]

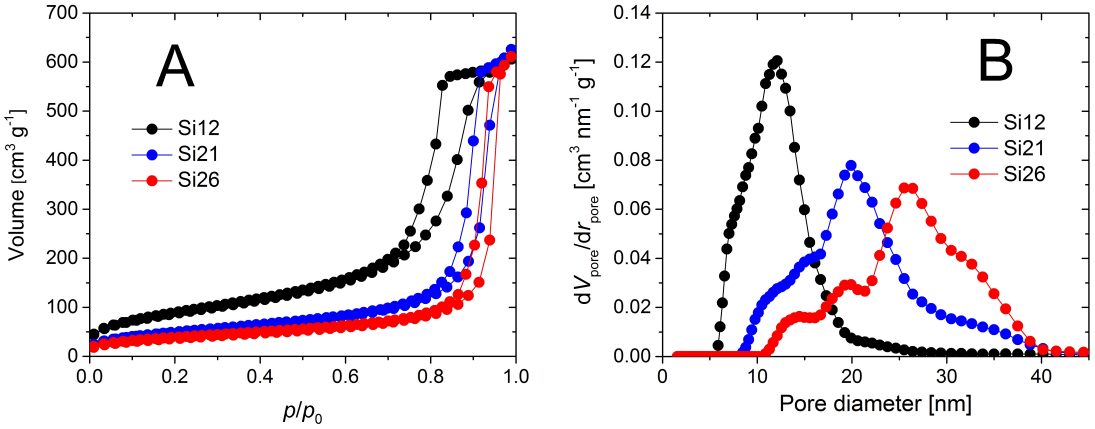

Figure 2.12: (A) Nitrogen sorption isotherms acquired for samples Si12, Si21, and Si26, as well as (B) the corresponding mesopore size distributions derived from NLDFT analysis of the adsorption branch.

[93] K. A. Cychosz et al. *Chem. Soc. Rev.*, 46, 389–414, 2017.

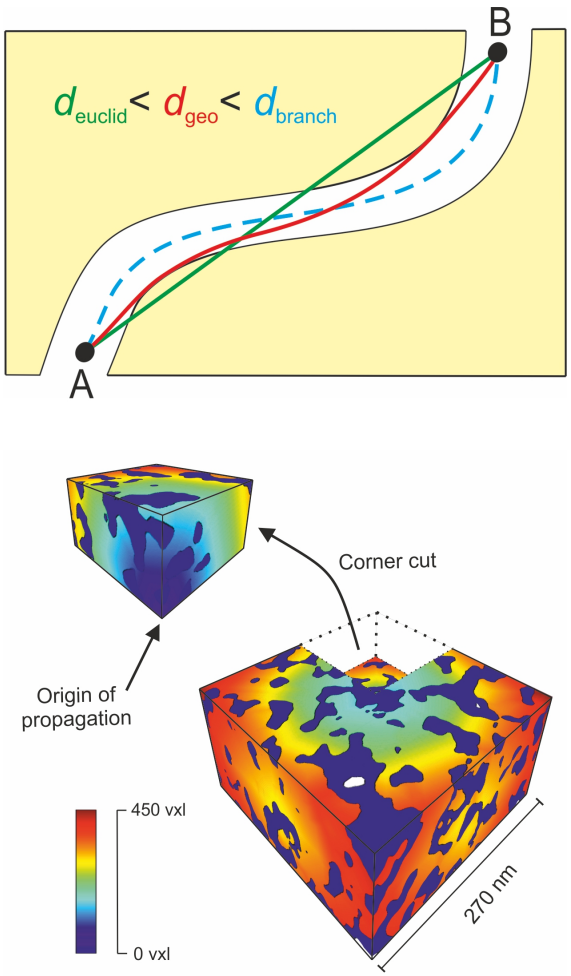

Figure 2.13: (Top) Schematic illustration of the medial axis branch length d_{branch}, the geodesic distance d_{geod}, and the Euclidean distance d_{euclid}. (Bottom) Visualization of geodesic distance extraction in the reconstructed mesopore space of sample Si26. The starting point of the propagation is indicated in the corner-cut representation. Geodesic distances are color-coded from blue to red (short to long distances) with dark blue indicating the solid phase.

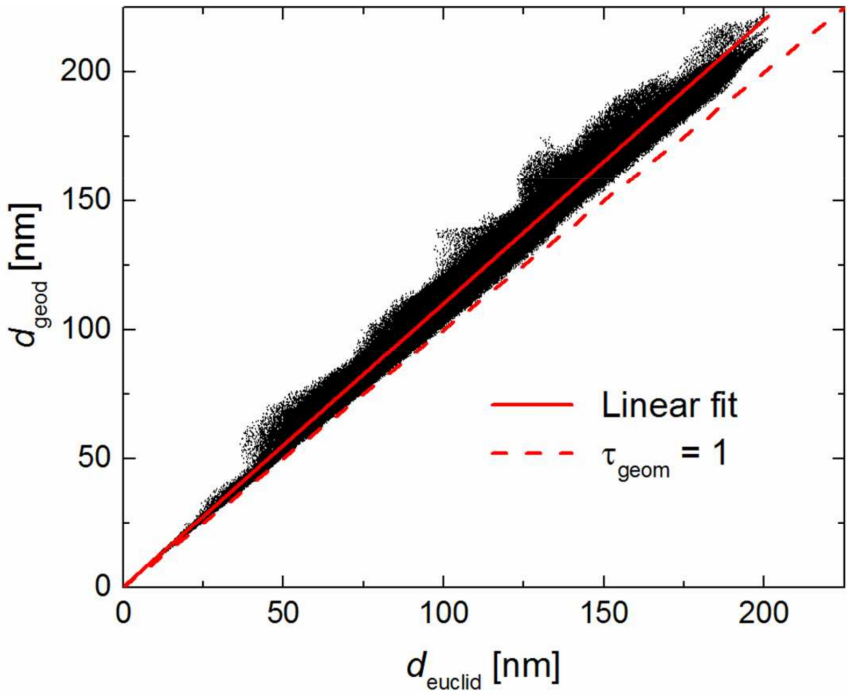

Figure 2.14: Geodesic distances against corresponding Euclidean distances as determined in the reconstructed mesopore space of sample Si12. The global geometric tortuosity τ_{geom} is derived from the slope of a linear fit (solid line); the dashed line indicates the lower limit of τ_{geom}.

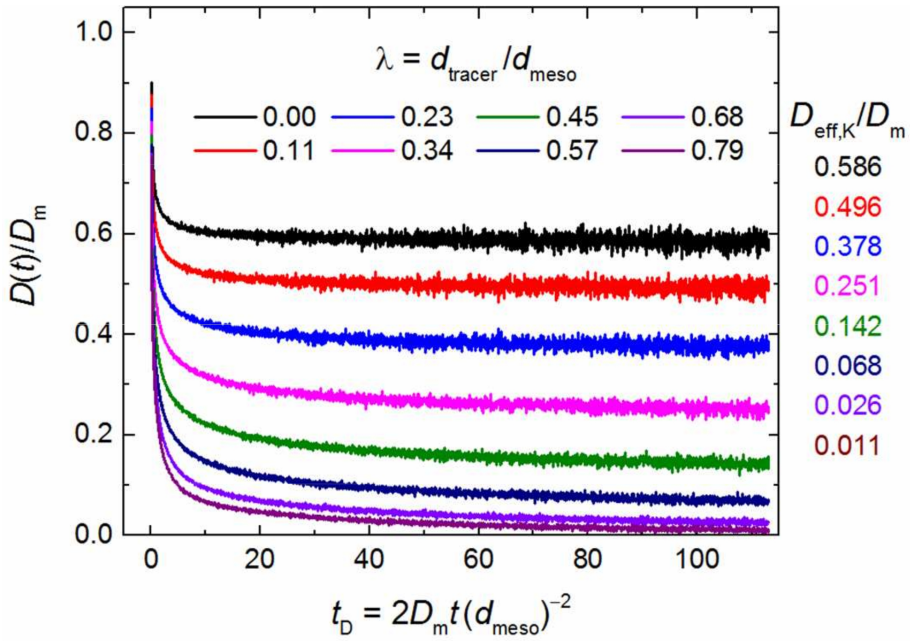

Figure 2.15: Tracer diffusion in the reconstructed mesopore space of sample Si12 ($d_{\text{meso}} = 12.3\,\text{nm}$) simulated for eight different values of λ, the ratio of tracer to mean mesopore size. Transient diffusion coefficients $D(t)$, normalized by the (free) molecular diffusion coefficient in the bulk liquid D_{m}, are shown as a function of the dimensionless diffusion time $t_{\text{D}} = 2D_{\text{m}}t(d_{\text{meso}})^{-2}$. $D_{\text{eff,K}}$ is the asymptotic (long-time) limit of $D(t)$ determined for each value of λ. The column at right gives the values for the local hindrance factor $K_{\text{d}}(\lambda) = D_{\text{eff,K}}(\lambda)/D_{\text{m}}$ for each λ-value (colorcoded).

2.6 Nomenclature

A_{spec} = specific surface area, m^2/g

$D(t)$ = time-dependent diffusion coefficient, m^2/g

$D_{\text{eff,H}}$ = global (macroscopic) effective diffusion coefficient, m^2/g

$D_{\text{eff,K}}$ = local (pore-level) effective diffusion coefficient, m^2/g

D_{m} = diffusion coefficient in the bulk liquid, m^2/g

d_{branch} = node-to-node network distance, nm

d_{geod} = geodesic distance, nm

d_{euclid} = Euclidean distance, nm

d_{meso} = mean mesopore size determined by nitrogen physisorption analysis, nm

d_{tracer} = diameter of tracer, nm

H = global diffusive hindrance factor, m^2/g

K_{d} = local diffusive hindrance factor, m^2/g

k = second-moment parameter of the chord length distribution (homogeneity factor)

l_{c} = chord length, nm

n_{j} = total number of junctions in the topological skeleton

n_{q} = number of quadruple-point junctions

n_{t} = number of triple-point junctions

n_{x} = number of higher-order junctions (connecting five or more branches)

p = fitting parameter in the modified Weissberg equation

r_{i} = position of the i-th tracer, nm

t = time, s

Z = average pore connectivity of the topological skeleton

Greek Symbols

Δh = spatial resolution of the physical reconstruction, nm

Δr_{i} = displacement of the i-th tracer, nm

δt = time step, s

ε_0 = porosity experienced by a point-like tracer

$\varepsilon(\lambda)$ = accessible porosity as a function of λ

Φ = equilibrium partitioning coefficient

Γ = Gamma function

λ = ratio of solute size or tracer diameter to mean pore size

μ = first statistical moment of the chord length distribution (mean chord length), nm

σ = standard deviation of the chord length distribution, nm

$\tau_0 =$ diffusive tortuosity experienced by a point-like tracer

$\tau(\lambda) =$ diffusive tortuosity as a function of λ

$\tau_{\text{branch}} =$ geometric branch tortuosity

$\tau_{\text{geom}} =$ geometric tortuosity

Chapter 3

Morphology of fluids confined in physically reconstructed mesoporous silica: Experiment and Mean Field Density Functional Theory

Authors:

Artur Svidrytski, Ashutosh Rathi, Dzmitry Hlushkou, David M. Ford, Peter A. Monson, and Ulrich Tallarek*

State of publication:

Published on August 02, 2018 in Langmuir, Vol. 34, pp 9936–9945
DOI: 10.1021/acs.langmuir.8b01971

Abstract

Three-dimensional physical reconstruction of the random mesopore network in a hierarchically structured, macroporous–mesoporous silica monolith via electron tomography has been used to generate a lattice model of amorphous, mesoporous silica. This geometrical model has subsequently been employed in mean field density functional theory (MFDFT) calculations of adsorption and desorption. Comparison of the results with experimental sorption isotherms for nitrogen at 77 K shows a good qualitative agreement, with both experiment and theory producing isotherms characterized by type H2 hysteresis. In addition to the isotherms, MFDFT provides the three-dimensional density distribution for the fluid in the porous material for each state studied. We use this information to map the phase distribution in the mesopore network in the hysteresis region. Phase distributions on the desorption boundary curve are compared to those on the adsorption boundary curve for both fixed pressure and fixed density, revealing insights into the relationship between phase distribution and hysteresis.

3.1 Introduction

Recent developments in imaging techniques permit detailed reconstruction of the morphology of porous materials and provide unprecedented insight into the material structure at nanoscopic

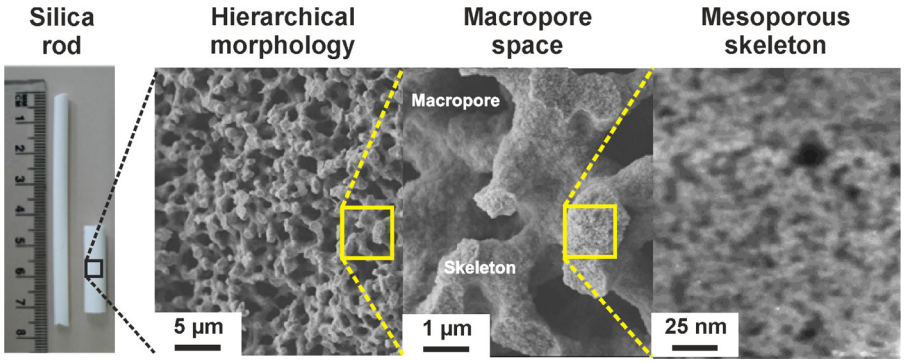

Figure 3.1: Hierarchical morphology of macroporous–mesoporous silica monoliths used as supports in liquid chromatography and catalysis (adapted from Stoeckel et al.[14]). Micrometer-sized macropores form an interskeleton network of flow-through channels for advection-dominated transport of liquid phase and solutes by pressure-driven flow. Mass transfer in the intraskeleton mesopores occurs by hindered diffusion, which depends on the actual pore space morphology and the ratio of solute size to mean mesopore size.

length scales.[18,123,124,181] At the same time, developments in molecular simulation and theory permit studies of both the density distribution and thermodynamics for fluids in porous materials.[32,104,115–120] Here, we deploy both these developments, together with experimental adsorption/desorption isotherms,[93] to investigate gas- and liquid-phase distributions in the hysteresis region for nitrogen at 77 K in amorphous, mesoporous silica from the mesoporous skeleton of a macroporous–mesoporous silica monolith illustrated further in Figure 3.1.[14]

Hierarchically structured silica monoliths of the type shown in Figure 3.1 (with interskeleton macropores and intraskeleton mesopores) enjoy widespread application in chemical separation and heterogeneous catalysis.[71,72,182–184] The macropores enable fast advective transport (usually by pressure-driven flow), the mesoporous skeleton provides a large surface for the active sites accessible by diffusion, and the resulting large contact area between macropores and skeleton

[18] R. Leary, P. A. Midgley, and J. M. Thomas. *Acc. Chem. Res.*, 45, 1782–1791, 2012.
[123] Z. Liu et al. *Microscopy*, 62, 109–146, 2013.
[124] D. S. Su, B. Zhang, and R. Schlögl. *Chem. Rev.*, 115, 2818–2882, 2015.
[181] P. Ercius et al. *Adv. Mater.*, 27, 5638–5663, 2015.
[32] B. Coasne. *New J. Chem.*, 40, 4078–4094, 2016.
[104] J. Landers, G. Y. Gor, and A. V. Neimark. *Colloid Surface A*, 437, 3–32, 2013.
[115] R. Evans. *J. Phys.: Condens. Mat.*, 2, 8989–9007, 1990.
[116] L. D. Gelb et al. *Reports Prog. Phys.*, 62, 1573–1659, 1999.
[117] A. V. Neimark, P. I. Ravikovitch, and A. Vishnyakov. *J. Phys.: Condens. Mat.*, 15, 347–365, 2003.
[118] P. A. Monson. *Micropor. Mesopor. Mat.*, 160, 47–66, 2012.
[119] J. D. Evans et al. *Chem. Mater.*, 29, 199–212, 2017.
[120] W. P. Krekelberg et al. *J. Phys. Chem. C*, 121, 16316–16327, 2017.
[93] K. A. Cychosz et al. *Chem. Soc. Rev.*, 46, 389–414, 2017.
[14] D. Stoeckel et al. *Langmuir*, 30, 9022–9027, 2014.
[71] K. K. Unger, R. Skudas, and M. M. Schulte. *J. Chromatogr. A*, 1184, 393–415, 2008.
[72] A. Galarneau et al. *Comptes Rendus Chim.*, 19, 231–247, 2016.
[182] K. Nakanishi and N. Tanaka. *Acc. Chem. Res.*, 40, 863–873, 2007.
[183] G. Guiochon. *J. Chromatogr. A*, 1168, 101–168, 2007.
[184] C. P. Haas et al. *React. Chem. Eng.*, 2, 498–511, 2017.

(the external surface) guarantees fast exchange between flowing and stagnant fluid.

Targeted optimization of monolith performance requires knowledge of relationships between monolith preparation, morphology, and resulting transport properties. Traditionally, the disordered mesopore space in these hierarchical materials is characterized by physisorption analysis.[93,121] But consequences of a given pore size distribution and pore network connectivity for the relevant mass-transport properties (e.g., effective diffusion) of a material are difficult to predict on a quantitative basis, unless structural descriptors with a proven strong correlation to the key transport phenomena become available.[28] To date, structural descriptors for random mesoporous silicas have not been discovered and hence quantitative morphology–transport relationships between hysteresis behavior, pore structure, and effective diffusivity are not available.

Physical reconstructions of amorphous, mesoporous silica from the mesoporous skeleton of macroporous–mesoporous silica monoliths have recently been employed as geometrical models in pore-scale simulations of hindered diffusion to derive a realistic hindrance factor expression for the effective diffusion coefficient of finite-size tracers.[24] Since the threedimensional array of solid and void voxels of a reconstruction is readily mapped onto a simple cubic lattice, it can also be incorporated in a lattice gas mean field density functional theory (MFDFT) to investigate the thermodynamics of a fluid confined in the mesoporous structure. This MFDFT approach with lattice gas models has been used quite widely in recent years to study the nature of adsorption and hysteresis in mesoporous materials.[118,185–187]

The present work represents a significant step forward for this approach in that the structural model used for the random mesoporous silica has been directly derived from the actual structure of the material based on electron tomography. For the particular structure considered, we have made MFDFT calculations of the molecular density distribution and thermodynamics, together with experimental measurements of the sorption isotherms for nitrogen at 77 K. There is a good agreement, with both experiment and theory showing isotherms with type H2 hysteresis. Using the three-dimensional density distributions for the fluid in the porous material for each state studied, we map the phase distribution in the random mesopore network in the hysteresis region. We compare the phase distributions on the desorption boundary curve to those on the adsorption boundary curve for both fixed pressure and fixed density, revealing insights into the relationship between phase distribution and hysteresis.

3.2 Experimental section

The material sample used to derive the three-dimensional reconstruction and geometrical model of amorphous, mesoporous silica has been removed from the mesoporous skeleton of a hierarchi-

[121] M. Thommes et al. *J. Chromatogr. A*, 1191, 57–66, 2008.
[28] T. Müllner, K. K. Unger, and U. Tallarek. *New J. Chem.*, 40, 3993–4015, 2016.
[24] S.-J. Reich et al. *Ind. Eng. Chem. Res.*, 57, 3031–3042, 2018.
[185] M. D. Donohue and G. L. Aranovich. *J. Colloid Interface Sci.*, 205, 121–130, 1998.
[186] E. Kierlik et al. *Phys. Rev. Lett.*, 87, 055701, 2001.
[187] D. W. Siderius and L. D. Gelb. *Langmuir*, 25, 1296–1299, 2009.

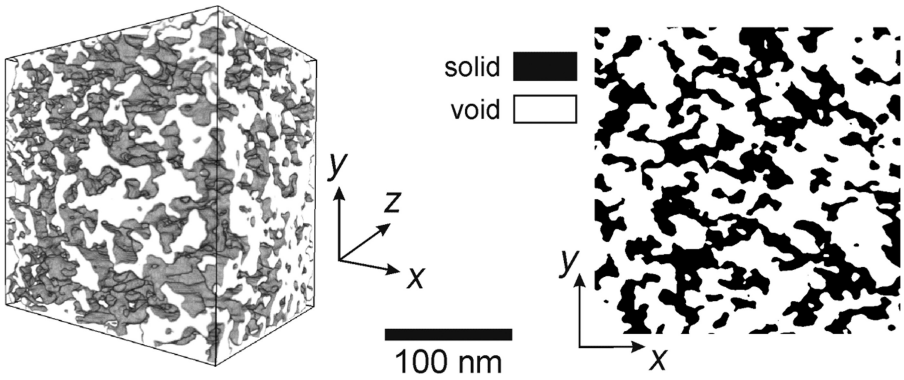

Figure 3.2: (Left) Three-dimensional reconstruction of amorphous, mesoporous silica from the skeleton of a macroporous–mesoporous silica monolith (cf. Figure 3.1) with a mean mesopore size of $12.3\,\mathrm{nm}$ and a mesoporosity of 0.577 (adapted from Reich et al.[24]). The physical dimensions of the reconstruction are $227.5 \times 227.5 \times 175\,\mathrm{nm}^3$ ($x \times y \times z$). (Right) Individual xy-slice from the reconstruction. The solid silica is shown in black.

cal silica monolith. The monolith has been prepared by standard sol–gel processing combined with chemically induced phase separation, followed by hydrothermal treatment of the gel to widen the intraskeleton micropores to mesopores through surface etching, resulting in the hierarchical, macroporous–mesoporous morphology illustrated in Figure 3.1.[152,182,183]

The monolith has been characterized by nitrogen physisorption at $77\,\mathrm{K}$ on an automated gas adsorption station (QUADRASORB evo, Quantachrome Corporation, Boynton Beach, FL), as reported.[24] The mesopore size distribution was derived from the adsorption branch of the nitrogen sorption isotherm using the non-local density functional theory method with a cylindrical pore model.[93] On the basis of this analysis, the silica sample has a mean mesopore size of $12.3\,\mathrm{nm}$ and a specific surface area of $315.7\,\mathrm{m}^2\,\mathrm{g}^{-1}$. A three-dimensional geometrical model of its mesopore space has been obtained from a single silica crumb using electron tomography.[24] Subsequent analysis of finite-size effects proved the reconstruction shown in Figure 3.2 to be representative of the monolith's mesopore space and therefore suitable for the derivation of global morphological and transport characteristics. The final image stack had dimensions of $227.5 \times 227.5 \times 175\,nm^3$ ($x \times y \times z$) consisting of $0.353^3\,nm^3$ voxels. The physical reconstruction in Figure 3.2 covers a volume of $9\,\mathrm{nL}$ and has a porosity (void volume fraction) of 0.577.

To characterize the morphology of fluid confined in the mesopore space at different relative pressures during simulated adsorption and desorption, we use medial axis analysis: an iterative-thinning algorithm, available as ImageJ plug-in bundle (Skeletonize3D and AnalyzeSkeleton), is applied to reduce the void space occupied by the gas phase at a given pressure to a medial axis of one-voxel thickness under conservation of its topological properties. The number of branches that originate from a junction (a node of the medial axis) can be interpreted as the local connectivity, without the need to define the limits of individual pores.

[152] S. Altmaier and K. Cabrera. *J. Sep. Sci.*, 31, 2551–2559, 2008.

3.3 Modeling

3.3.1 Lattice model and Mean Field DFT

We use a single-occupancy, nearest-neighbor lattice gas model for which, in MFT, the grand free energy is given by[118,186]

$$\Omega = kT \sum_i \left[(\rho_i \ln \rho_i) + (1-\rho_i)\ln(1-\rho_i)\right] - \epsilon \sum_{i<j}{}' \rho_i \rho_j + \sum_i \rho_i(\phi_i - \mu) \tag{3.1}$$

where T is the absolute temperature, k is the Boltzmann constant, ρ_i is the average fluid density at site i, $-\epsilon$ is the attractive energy between fluid molecules on nearest-neighbor sites, ϕ_i is the external field associated with the fluid–solid interaction and is a nearest-neighbor attraction with energy $-\alpha\epsilon$ (in this work, $\alpha = 2$), and μ is the chemical potential of the fluid. The primed sum denotes the restriction to pairs of sites that are nearest neighbors and which are not occupied by solid. The parameter α represents the relative strength of the interaction of a fluid molecule with the solid surface and generally accounts for both the nearest-neighbor interactions and the longer-ranged interactions integrated across the width and depth of the solid. We explored values of α ranging from 1.0 to 3.0 and found that a value of 2.0 produced isotherms that were in reasonably good agreement with the experimental isotherms across the full range of partial pressures, as described below. The bulk lattice fluid properties were obtained from eqs 2.12 and 2.13 of ref.[118] The reduced temperature of the lattice model was set to $kT/\epsilon = 0.9$. The reduced critical temperature in the lattice model in MFT is $kT/\epsilon = 1.5$. The critical temperature of nitrogen is $126.2\,\mathrm{K}$. Thus, $77\,\mathrm{K}$ is approximately equivalent to 0.6 times the critical temperature of nitrogen. Equivalently, a lattice model temperature of 0.9 is 0.6 times the critical temperature of the lattice model of 1.5.

The necessary condition for a minimum in Ω is obtained by setting its partial derivatives with respect to the ρ_i's to zero leading to the following set of nonlinear equations

$$kT \ln\left[\frac{\rho_i}{(1-\rho_i)}\right] - \epsilon \sum_j{}' \rho_j + \phi_i - \mu = 0 \quad \forall i \tag{3.2}$$

These equations are solved by fixed-point iteration starting from an initial estimate of the density distribution. To study an adsorption isotherm of average density versus relative pressure (p/p_0), we start from a low-pressure (low chemical potential) state corresponding to a low-adsorption vaporlike state in the porous material (initial state, $p/p_0 \to 0$). We then solve for increasing values of chemical potential up to the value for the bulk saturated vapor ($\mu_0 = -3kT$ for a simple cubic lattice), using the solution from the previous state as the initial estimate for the next solution. For a desorption isotherm, we start from the final state on the adsorption branch and

then follow a sequence of states of decreasing chemical potential until the original low chemical potential state is achieved.

3.3.2 Implementation for mesoporous silica

The lattice gas model is a coarse-grained one, and the lattice dimensions need not coincide with the molecular dimensions. The characteristic length scale of the real system is taken as the voxel size of the three-dimensional image ($0.35\,\mathrm{nm}$). It serves as a basis to construct the lattice model, which in this case has a spatial resolution (lattice constant) of $1.167\,\mathrm{nm}$. We have found that the optimal agreement between DFT and experiment occurs when the lattice constant is substantially larger than the voxel size. This has its origin in the fact that molecules are restricted to lattice sites, which reduces the number of possible configurations available and greatly diminishes configurational frustration under confinement compared to an off-lattice model.

We take two grids of the same total dimensions $227.5 \times 227.5 \times 175\,\mathrm{nm}^3$, but one with a cubic element of size $0.35 \times 0.35 \times 0.35\,\mathrm{nm}^3$ (grid 1) and the other one with a cubic element of size $1.167 \times 1.167 \times 1.167\,\mathrm{nm}^3$ (grid 2). Grid 1 represents the physical reconstruction of the mesoporous skeleton from the silica monolith, while grid 2 corresponds to the coarse-grained lattice representation of the skeleton. Each element in grid 1 is either fluid-accessible or solid denoted by a value of 1.0 or 0.0, respectively. We now superimpose the two grids and find the values for elements in grid 2 linearly interpolating from the values of elements in grid 1. The linearly interpolated values for elements in grid 2 end up being fractional. We assume that any element with value less than 0.5 is solid and reassign it a value of 0.0, while any element with a value larger than 0.5 is assumed to be fluid-accessible and reassigned a value of 1.0. We then use grid 2 for lattice model calculations assuming each element as one lattice site. This procedure was used only to identify the phase distributions in the system. The actual density distributions from the MFT were used to calculate the adsorption/desorption isotherms.

We solve the DFT equations for a system in which the fluid in the porous material is in contact with the bulk by surrounding our model sample by bulk in each direction. Figure 3.3 shows the setup for our calculations viewed from one side. The contact with the bulk is essential for correctly describing the development of vapor–liquid interfaces in the pores on the desorption branch of the hysteresis loop. Our model sample has $235 \times 235 \times 190$ lattice sites, including 20 lattice sites in each direction to model the bulk. To reduce the effects of the density inhomogeneity at the boundaries, we average the density over a central region of the material defined to be 15 sites from the external surface on each side. The entire system is in periodic boundaries.

To make a quantitative comparison with experiment, we need to relate the experimentally determined fluid density to the fractional density produced in our model calculations. For this purpose, we normalize the density with respect to that at the upper closure point of the hysteresis loop for both theory and experiment.

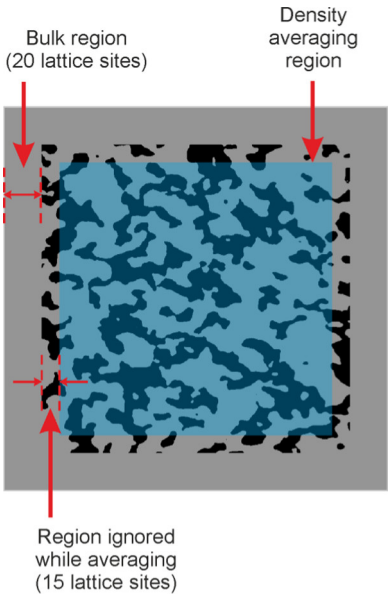

Figure 3.3: Schematic of the simulation of adsorption/desorption in the reconstructed mesopore space from the skeleton of a macroporous–mesoporous silica monolith (cf. Figures 3.1 and 3.2). The solid silica is shown in black.

3.4 Results and discussion

We have made DFT calculations for the reconstruction of amorphous, mesoporous silica shown in the left panel of Figure 3.2. For both adsorption and desorption, the spatial distributions of liquid phase and gas phase were determined for 200 values of the relative pressure (p/p_0) between 0 and 1. For each state, the results were saved as three-dimensional arrays of voxels corresponding to gas phase, liquid, and solid silica. Vapor and liquid were distinguished by assigning sites as liquid if the average occupancy was greater than 0.5 (and vapor otherwise). From the phase distributions for each p/p_0 value, the corresponding normalized density was determined as the fraction of voxels associated with liquid.

Experimental and simulated sorption isotherms are shown in the middle panel of Figure 3.4. The agreement is qualitatively good, with both isotherms exhibiting hysteresis for p/p_0 between 0.6 and 0.95. The hysteresis is of type H2.[93] The agreement between experiment and simulation at low density is relatively poor in part because the agreement was optimized for the hysteresis region. Also the low-pressure behavior for this structurally disordered system is more sensitive to the details of the solid–fluid interactions, and these are treated in a very simple way (nearest-neighbor interactions on a lattice) in our model. In contrast to the experimental data, the comprehensive information available from the simulations about the three-dimensional spatial distribution of gas and liquid allows us to determine also morphological characteristics of the spatial domains occupied by the phases and to analyze the evolution of these characteristics with relative pressure. For instance, the topology of the changing space occupied by gas phase can be described with the corresponding medial axis network. This branch-node network is generated by reducing the analyzed spatial domain (in this case, the space occupied by the gas phase at

each p/p_0 value) to a medial axis of one-voxel thickness under conservation of its topological properties.[24]

In turn, changes in the spatial distribution of the gas phase during an adsorption/desorption cycle will lead to different medial axis networks for different relative pressures. This is illustrated by the results presented in the top and bottom panels of Figure 3.4. The top panel shows (in red) the medial axis network for the gas phase at the initial state of the simulation ($p/p_0 \to 0$). This situation is highlighted for an individual slice seen next to the medial axis network, where the gas phase is white and the solid silica is black. The bottom panel of Figure 3.4 compares gas-phase medial axis networks at $p/p_0 = 0.82$ for adsorption and desorption. Differences in these networks reflect different distributions of gas phase and liquid (the latter shown in blue) for the isotherms at identical relative pressure. It indicates that the hysteresis exhibited by the normalized density can also be monitored (and complementary analyzed) through morphological descriptors for the spatial distributions of gas phase and liquid phase.

Figure 3.5A–C compares the simulated sorption isotherms (always in gray) with the evolution of three morphological characteristics of the void space in the reconstruction occupied by gas phase as a function of relative pressure. The green curves in Figure 3.5A illustrate the change in volume fraction of the gas phase with p/p_0. This hysteresis can be readily explained by the interdependence of gas-phase volume fraction and density. In Figure 3.5B, the simulated sorption isotherms are compared to the evolution of the solid–gas interfacial area (red curves). Similar to the sorption isotherms, there is no significant difference in the solid–gas interfacial area for adsorption and desorption branches at relative pressures between 0 and 0.6. However, for $p/p_0 > 0.6$, this morphological characteristic changes differently for adsorption and desorption; the shape of the hysteresis is very close to that of the gas phase volume fraction seen in Figure 3.5A. To evaluate topological changes for the phase distributions, we analyzed the number of triple-point junctions n_t (connecting three branches) in the medial axis networks for the changing space occupied by gas phase. This topological parameter characterizes the connectivity of the spatial domains occupied by an analyzed phase. The blue curves in Figure 3.5C summarize the evolution of n_t with p/p_0. This complementary analysis may in the future help to establish links between the thermodynamics (sorption) and dynamics (transport) on the mesoscopic scale of a reconstruction. For example, the pore networks evolving during an adsorption/desorption cycle can serve as a basis to calculate the geometrical tortuosities for gas phase and liquid phase at each relative pressure, reflecting actual obstruction to percolation and diffusion.[28] Overall, the hysteresis behavior revealed by the three morphological characteristics of the phase distributions (Figure 3.5A–C) consistently monitors the hysteresis of the sorption isotherms.

Figure 3.6 compares the phase distributions in the central xy-plane of the reconstruction for three points taken from the sorption isotherms. Point A (adsorption isotherm) corresponds to a relative pressure of $p/p_0 = 0.848$ and a normalized density of 0.578. The other two points (desorption isotherm) are characterized by either the same relative pressure (point B) or the same normalized density (point C) compared to point A. At the identical relative pressure (points A and B), the normalized density for the desorption branch is higher than that during adsorption. A

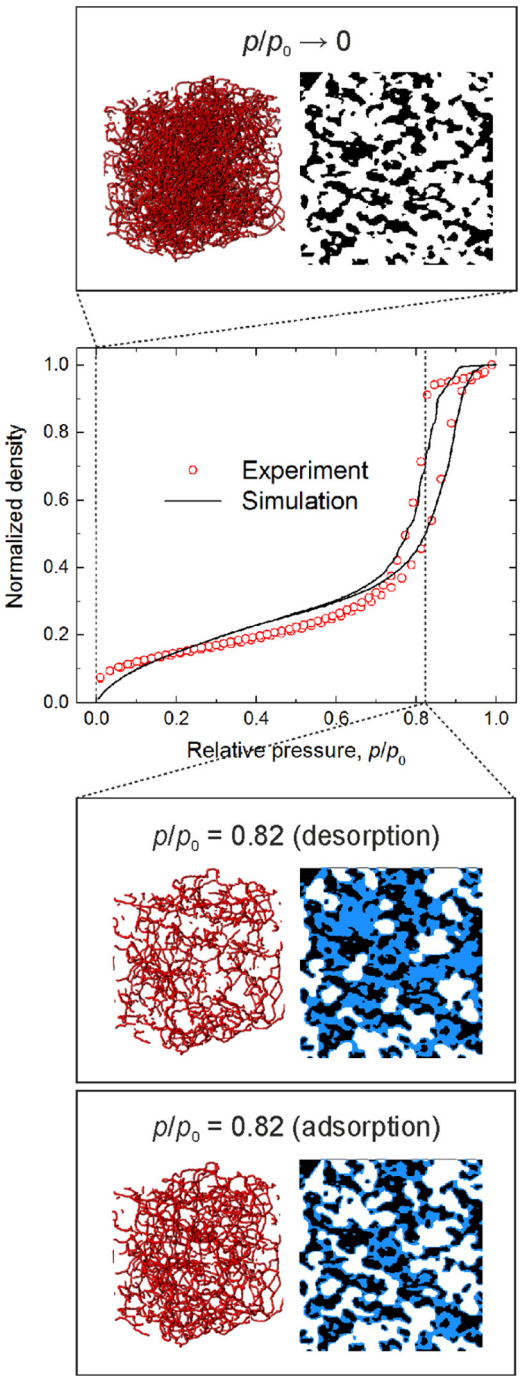

Figure 3.4: Comparison of experimental and simulated sorption isotherms (middle panel). The top panel shows the phase distribution and the medial axis network for the space occupied by gas phase at the initial state of the simulation ($p/p_0 \to 0$). In the bottom panel, the phase distributions and medial axis networks are compared for adsorption and desorption at identical relative pressure of $p/p0 = 0.82$. Gas phase: white; solid silica: black; liquid phase: blue.

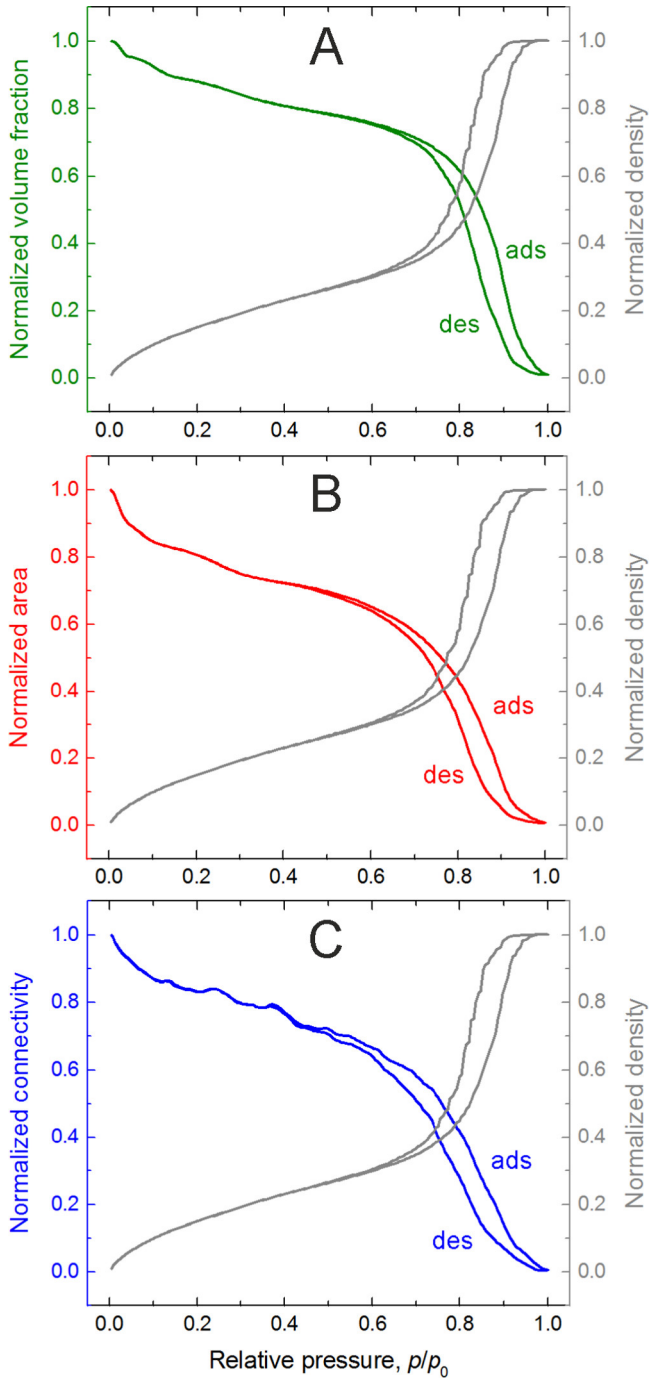

Figure 3.5: Comparison of hysteresis for the sorption isotherms (gray) and the morphological characteristics of the space occupied by gas phase: (A) volume fraction (green); (B) solid–gas interfacial area (red); and (C) number of triple-point junctions in the medial axis network (blue). The morphological characteristics are normalized by the corresponding value for the initial state of the simulation ($p/p0 \to 0$).

comparison of phase distributions corresponding to points A and B reveals that during desorption, an additional fraction of the liquid phase is distributed nonuniformly relative to adsorption. For instance, region a is characterized by a similar thickness of the adsorbed layers for adsorption and desorption. By contrast, region b is saturated with liquid during desorption, but mostly contains gas phase during adsorption. Points A and C in Figure 3.6 represent adsorption and desorption at the same normalized density. Although the corresponding phase distributions seem to be very similar for these points, a rigorous comparison reveals the presence of regions that are occupied by liquid for either adsorption or desorption. For instance, region c contains a large gas volume during adsorption, which is liquid-filled for desorption. By contrast, region d is saturated with liquid for adsorption, while gas phase is present during desorption. The evolution of the phase distributions for adsorption and desorption in this central xy-plane of the reconstruction is illustrated in two movies in the Supporting Information[§].

To distinguish between regions occupied by different phases during adsorption and desorption, we overlayed the phase distributions corresponding to points A and B and those corresponding to points A and C. The result of this analysis is presented in Figure 3.7. We used the following color coding for the liquid phase: blue identifies regions occupied by liquid for both adsorption and desorption; green highlights regions filled with liquid only for adsorption (that is, filled with gas phase for desorption); and magenta indicates regions where liquid is present only during desorption. The left panel in Figure 3.7illustrates the comparison of phase distributions corresponding to points A and B, i.e., to adsorption and desorption at the same relative pressure ($p/p_0 = 0.848$). The absence of green areas indicates that for adsorption, the liquid occupies only regions in which it is present also during desorption. The same is observed for the phase distributions at any position in the sample and for all 200 simulated p/p_0 values: at any pressure, the volume occupied by liquid phase during desorption is the volume occupied during adsorption (at this pressure) plus an additional volume. This finding can be explained by a classical scenario in capillary condensation, which implies that the vapor–liquid transition is delayed due to the existence of metastable adsorption layers and hindered nucleation of liquid bridges between pore walls.[93]

The right panel in Figure 3.7 compares the phase distributions corresponding to points A and C in Figure 3.6. The distributions of liquid phase for these two states with identical average density are remarkably different. The green areas represent regions saturated with liquid during adsorption but filled with gas phase for desorption. These regions are mainly thin layers and their formation can be explained by a higher pressure ($p/p_0 = 0.848$) during adsorption than during desorption ($p/p_0 = 0.799$) needed to achieve the same normalized density of 0.578. The magenta areas are regions where liquid is present only during desorption. In contrast to the layered structure of the green regions, the majority of the magenta regions is recognized as compact volumes. According to the color coding, these regions are free of liquid during adsorption (notwithstanding the higher pressure). Their existence can be explained by pore blocking, i.e.,

[§] The Supporting Information (movies showing the simulated evolution of phase distributions) is available free of charge on the ACS Publications website at DOI: 10.1021/acs.langmuir.8b01971

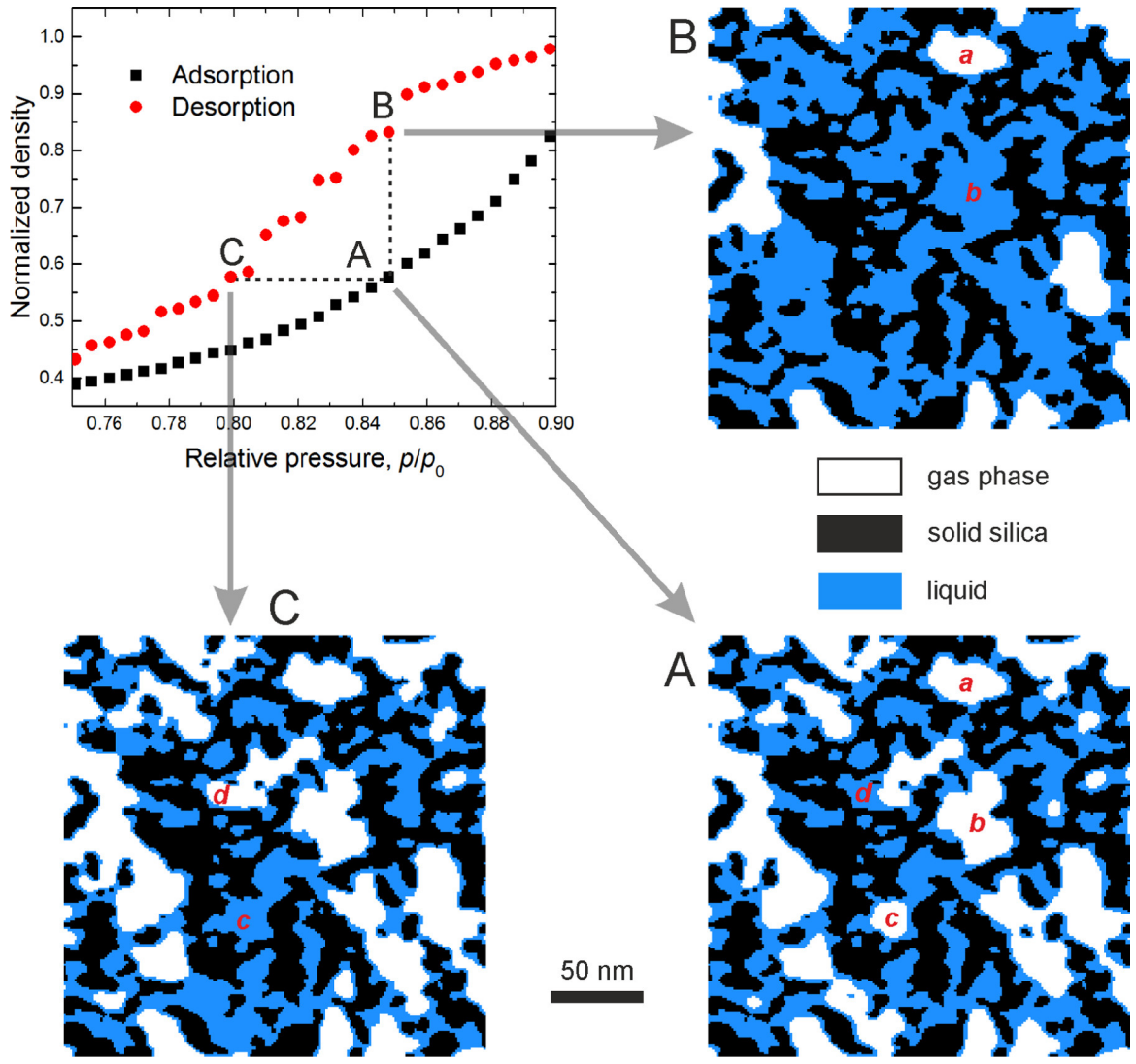

Figure 3.6: Comparison of the simulated distributions of liquid phase and gas phase for three points (A–C) from the sorption isotherms in the central xy-plane ($227.5 \times 227.5\,\mathrm{nm}^2$) of the reconstruction.

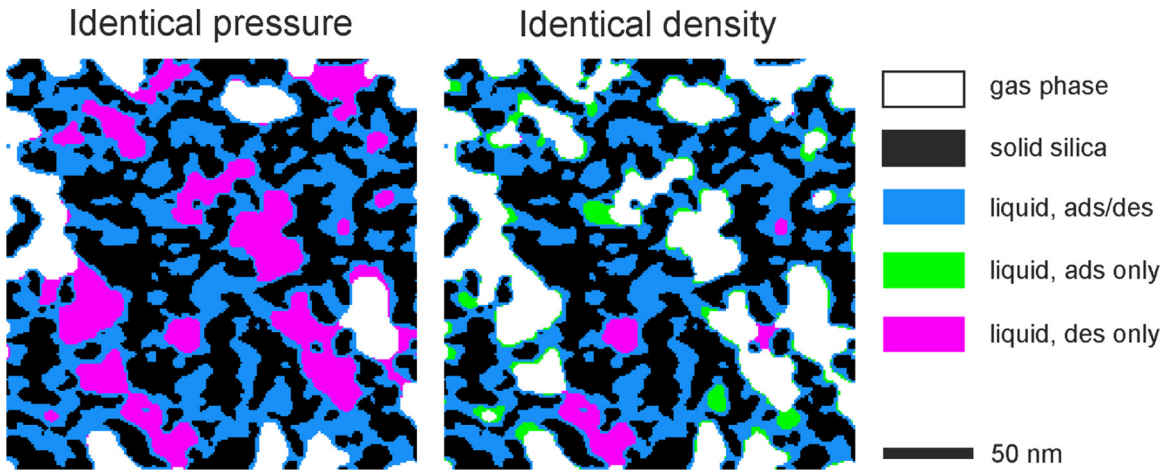

Figure 3.7: Comparison of the phase distributions for adsorption and desorption at an identical relative pressure of 0.848 (points A and B, Figure 3.6) and at an identical normalized density of 0.578 (points A and C, Figure 3.6) in the central xy-plane ($227.5 \times 227.5\,\mathrm{nm}^2$) of the reconstruction.

if a pore filled with condensate is connected to an external face through pores of smaller size, it can be emptied only after the evaporation of condensate from these small pores.[110]

Figure 3.8 shows three-dimensional distributions of the gas phase (in red) corresponding to points A and C in Figure 3.6. These distributions are highlighted for a subdomain from the reconstruction with dimensions of $82 \times 104 \times 93\,\mathrm{nm}^3$ (for better visibility, liquid phase and solid skeleton are not included). This subdomain contains a closed-end pore connected to two outer faces of the sample by a narrow neck. The occurrence of pore blocking and delayed condensation in this subdomain was confirmed by a three-dimensional analysis of the evolution of phase distributions with applied pressure. The result of this analysis is presented in Figure 3.9A–E, which shows the distribution of gas phase (in red) at different pressures during adsorption and desorption in the subdomain of the sample. For desorption at $p/p_0 = 0.799$, the region of interest highlighted by the green frame is filled with liquid (Figure 3.9D) and thus appears white. However, a decrease in relative pressure by only 0.005 results in a complete emptying of the pore (Figure 3.9E), which has turned red. During adsorption, this pore is not completely filled with condensate even at a relative pressure of $p/p_0 = 0.881$ (Figure 3.9A). With an increase in pressure to $p/p_0 = 0.892$, a narrow neck of the pore is filled with condensate, but the end of the pore still contains a spatially isolated domain with gas phase (Figure 3.9B). Only with a further increase in the relative pressure to 0.898, this domain is finally saturated with liquid (Figure 3.9C).

Additionally, we performed a three-dimensional analysis of the gas-phase distribution within the reconstruction along the complete desorption branch to detect enclosed gas-phase volumes, which can indicate cavitation. While a two-dimensional representation of the phase distribution (e.g., in Figure 3.6) suggests the occurrence of such volumes during desorption, careful three-

[110] P. I. Ravikovitch and A. V. Neimark. *Langmuir*, 18, 9830–9837, 2002.

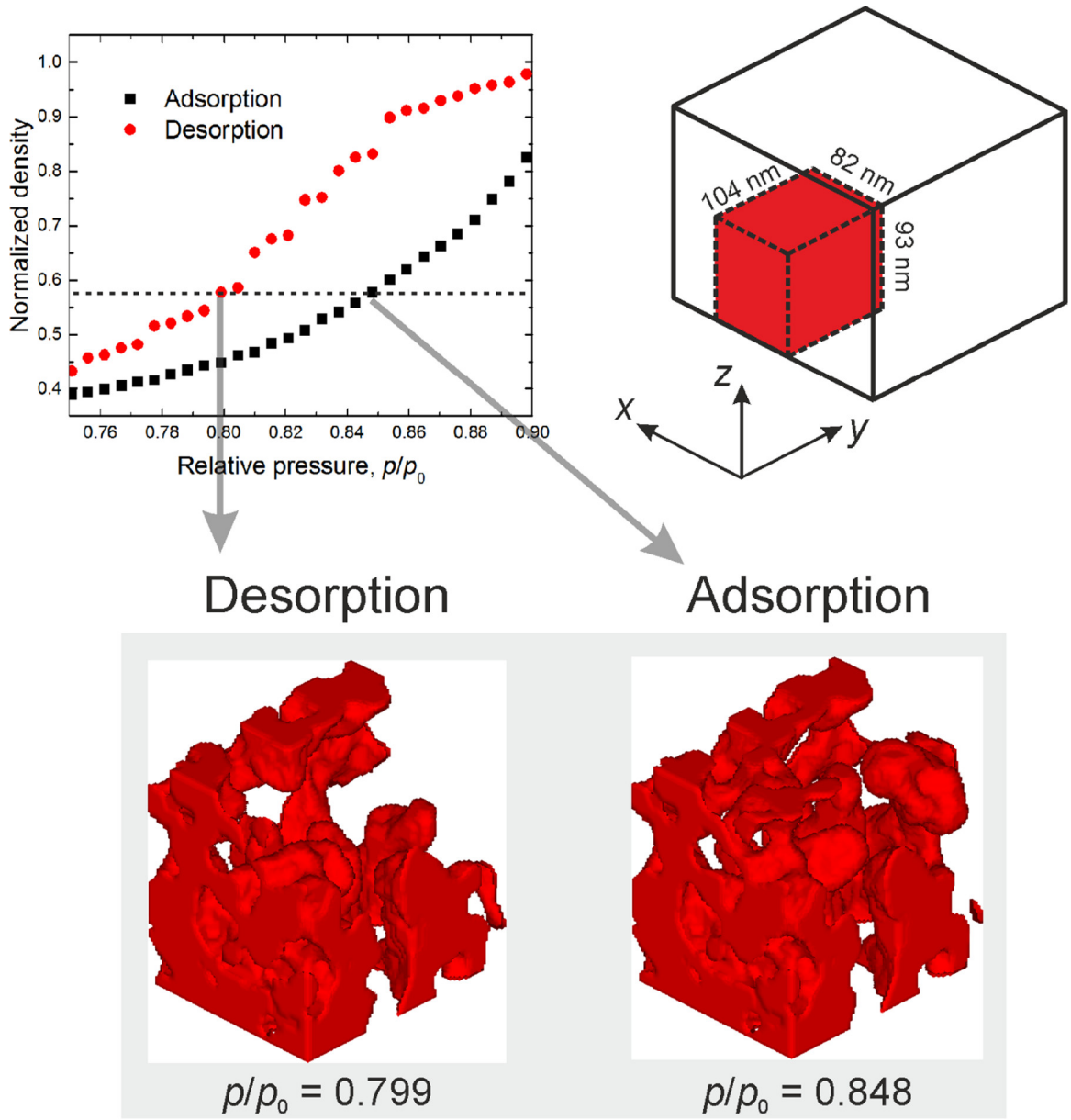

Figure 3.8: Distribution of gas phase (in red) during adsorption and desorption at an identical normalized density of 0.578. The distributions are highlighted for a subdomain of the reconstruction shown in Figure 3.2 with dimensions of $82 \times 104 \times 93\,\mathrm{nm}^3$ ($x \times y \times z$). For enhanced visibility, liquid phase and solid are not shown.

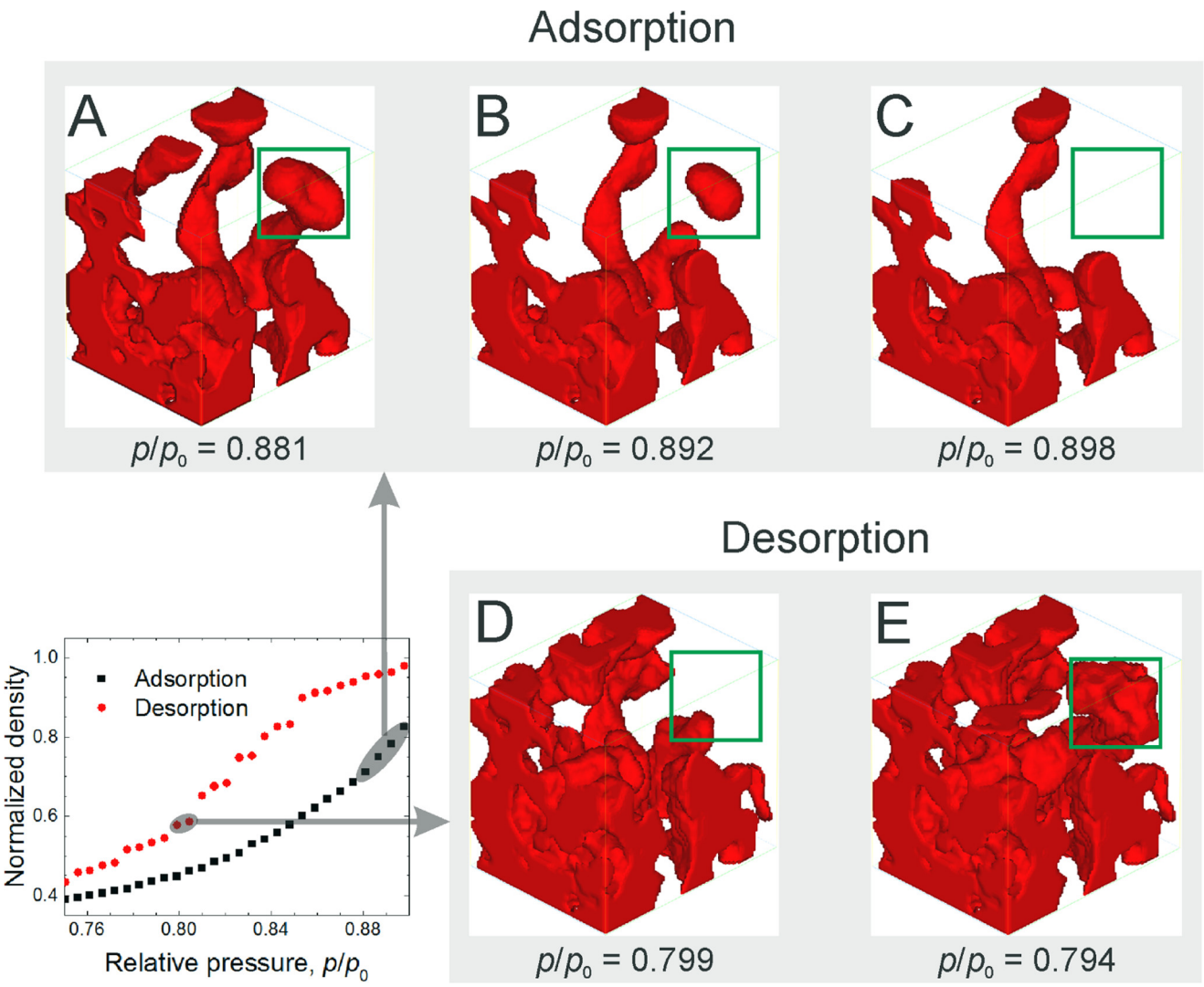

Figure 3.9: Distribution of gas phase (in red) at different relative pressure during adsorption (A–C) and desorption (D, E) in the subdomain of the reconstruction (cf. Figure 3.8). The region of interest, where pore blocking and delayed condensation are observed, is highlighted by the green frame. For enhanced visibility, liquid phase and solid are not shown.

dimensional analysis confirmed that any voxel assigned to gas phase is always connected to at least one of the outer faces of the sample. The absence of cavitation can be explained by the well-interconnected pore network in the investigated sample with a mean pore size of $\sim 12\,\mathrm{nm}$, which is significantly larger than a critical value of $5-6\,\mathrm{nm}$ for nitrogen at $77\,\mathrm{K}$ required for the occurrence of cavitation in pores with an ink-bottle geometry.[110]

3.5 Conclusions

We have combined three-dimensional physical reconstruction of the pore space morphology for amorphous, mesoporous silica from a hierarchical (macroporous–mesoporous) silica monolith by electron tomography with MFDFT studies of adsorption and desorption in the resulting realistic geometrical model. The results from MFDFT are in good agreement with experimental sorption isotherms for nitrogen at $77\,\mathrm{K}$. We have used the density distributions derived with the MFDFT calculations to construct phase distributions for each state studied. This allows us to compare phase distributions on the adsorption and desorption boundary curves of the hysteresis loop. This can be done at both fixed relative pressure, where the average density is higher on the desorption boundary curve, and at fixed average density. Desorption in these systems follows a classical pore-blocking mechanism with invasion percolation of the gas phase from the exterior of the sample. Cavitation does not appear to be part of the mechanism.

The present work illustrates that the combination of reconstruction via imaging with sorption experiments and MFDFT is a promising approach to understanding the nature of fluid distributions for fluids confined in mesoporous materials with a complex, three-dimensional morphology. We will pursue this methodology, in particular, to compare the hysteresis revealed here for the random mesoporous silica with the behavior of ordered mesoporous silicas (e.g., SBA-15 and KIT-6) in view of their salient morphological features.[7]

Acknowledgements

This study is based on work supported by the Deutsche Forschungsgemeinschaft under grant TA 268/9-1 and by the U.S. National Science Foundation under grant CBET-1403542

[7] S.-J. Reich et al. *J. Phys. Chem. C*, 122, 12350–12361, 2018.

Chapter 4

Modeling the impact of mesoporous silica microstructures on the adsorption hysteresis loop

Authors:

Artur Svidrytski, Dzmitry Hlushkou, Matthias Thommes, Peter A. Monson, and Ulrich Tallarek*

State of publication:

Published on September 22, 2020 in The Journal of Physical Chemistry, Vol. 124, pp 21646–21655

DOI: 10.1021/acs.jpcc.0c07571

Abstract

We present a mean-field density functional theory (MFDFT) study of adsorption and desorption for nitrogen at $77\,\mathrm{K}$ in three-dimensional (3D) geometrical models of ordered and random mesoporous silicas obtained by electron tomography. Parameters of the lattice MFDFT model, such as reduced temperature, the ratio between the energies of fluid–solid and fluid–fluid interactions, and the lattice unit size, were investigated to achieve best qualitative agreement with experimental isotherms in the hysteresis region. Equilibrium and metastable equilibrium states were analyzed for 500 pressure values in the range of $0 < p/p_0 \leq 1$ for both adsorption and desorption, which allowed us to resolve subtle features of the isotherms. Calculated and experimental isotherms show good agreement in the hysteresis region, identifying type IV(a) isotherms with a H1 hysteresis loop for ordered silicas (SBA-15, KIT-6) and H2(a) hysteresis loop for random silica. Hysteresis loops are particularly narrow and hysteresis branches parallel and almost vertical for the ordered silicas. This indicates homogeneous microstructures of uniform, cylindrical pores and confirms that the SBA-15 silica has a highly interconnected 3D mesopore network, as targeted with its preparation, mimicking the pristine 3D mesopore structure of KIT-6 silica. For the random silica, characterized by a heterogeneous microstructure with many narrow and highly constricted pores, the available phase distributions allowed us to distinguish between pore blocking and cavitation along the desorption branch and to monitor the dependence of

cavitation bubble size on relative pressure using image analysis. Complementary calculated desorption scanning isotherms reflect pore evaporation in the ordered silicas as expected from an independent pore model, whereas the representative behavior of dependent pores in the random silica involves pore blocking/percolation.

4.1 Introduction

Several theoretical and numerical models have been developed to study both the density distribution and thermodynamics of fluids in porous materials as well as to describe the sorption hysteresis.[32,98,101,102,104,106,115–117,119,120,185,187–192] In particular, mean-field density functional theory (MFDFT) applied to lattice fluid models of mesoporous systems provides a coarse grained approach to modeling sorption on length scale approaching experimental conditions.[107,118,186] Developments in electron tomography permit the complementary reconstruction of the morphology of mesoporous materials, offering unprecedented insight into the material structure at nanoscopic length scales.[18,123,124,181] In a recent paper, we applied MFDFT for calculating nitrogen adsorption–desorption isotherms for a mesoporous silica sample from the skeleton of a hierarchical, macro–mesoporous silica monolith.[34] The reconstructed image of the sample obtained by electron tomography was used directly to build the pore structure used in the MFDFT. Calculated isotherms demonstrated good qualitative agreement with experimental nitrogen sorption isotherms at 77 K. In particular, for the hysteresis region the calculations reproduced the classical scenarios of delayed condensation (adsorption branch) and pore blocking (desorption

[32] B. Coasne. *New J. Chem.*, 40, 4078–4094, 2016.
[98] K. Morishige. *Langmuir*, 29, 11915–11923, 2013.
[101] B. Coasne, K. E. Gubbins, and R. J.-M. Pellenq. *Phys. Rev. B*, 72, 024304, 2005.
[102] K. Morishige. *J. Phys. Chem. C*, 121, 5099–5107, 2017.
[104] J. Landers, G. Y. Gor, and A. V. Neimark. *Colloid Surface A*, 437, 3–32, 2013.
[106] K. Morishige and N. Tarui. *J. Phys. Chem. C*, 111, 280–285, 2007.
[115] R. Evans. *J. Phys.: Condens. Mat.*, 2, 8989–9007, 1990.
[116] L. D. Gelb et al. *Reports Prog. Phys.*, 62, 1573–1659, 1999.
[117] A. V. Neimark, P. I. Ravikovitch, and A. Vishnyakov. *J. Phys.: Condens. Mat.*, 15, 347–365, 2003.
[119] J. D. Evans et al. *Chem. Mater.*, 29, 199–212, 2017.
[120] W. P. Krekelberg et al. *J. Phys. Chem. C*, 121, 16316–16327, 2017.
[185] M. D. Donohue and G. L. Aranovich. *J. Colloid Interface Sci.*, 205, 121–130, 1998.
[187] D. W. Siderius and L. D. Gelb. *Langmuir*, 25, 1296–1299, 2009.
[188] G. Y. Gor, C. J. Rasmussen, and A. V. Neimark. *Langmuir*, 28, 12100–12107, 2012.
[189] D. Schneider, R. Valiullin, and P. A. Monson. *Langmuir*, 31, 188–198, 2015.
[190] L. Deliere et al. *Micropor. Mesopor. Mat.*, 229, 145–154, 2016.
[191] D. W. Siderius et al. *Langmuir*, 33, 14252–14262, 2017.
[192] D. Schneider and R. Valiullin. *J. Phys. Chem. C*, 123, 16239–16249, 2019.
[107] H.-J. Woo, L. Sarkisov, and P. A. Monson. *Langmuir*, 17, 7472–7475, 2001.
[118] P. A. Monson. *Micropor. Mesopor. Mat.*, 160, 47–66, 2012.
[186] E. Kierlik et al. *Phys. Rev. Lett.*, 87, 055701, 2001.
[18] R. Leary, P. A. Midgley, and J. M. Thomas. *Acc. Chem. Res.*, 45, 1782–1791, 2012.
[123] Z. Liu et al. *Microscopy*, 62, 109–146, 2013.
[124] D. S. Su, B. Zhang, and R. Schlögl. *Chem. Rev.*, 115, 2818–2882, 2015.
[181] P. Ercius et al. *Adv. Mater.*, 27, 5638–5663, 2015.
[34] A. Svidrytski et al. *Langmuir*, 34, 9936–9945, 2018.

branch). Moreover, the density distributions from the MFDFT revealed the nature of the fluid morphologies encountered in the hysteresis region.

In this work, we extend that simulation approach to electron tomography-based reconstructions of three mesoporous silica materials with characteristic pore architectures. Two of the materials are large-pore ordered mesoporous silicas SBA-15 and KIT-6. The primary pore system of SBA-15 silica consists of hexagonally arranged, cylindrical pores,[193] whereas the primary pore system of KIT-6 silica is a pair of interpenetrating, bicontinuous, three-dimensional (3D), cylindrical pore networks.[194] The primary pore system in both materials is complemented by a secondary system of random pores in the amorphous silica walls around the primary pores. The third material is a random mesoporous silica from the mesoporous shell of a solid core–porous shell particle. These particles are prepared by immobilization of sol nanoparticles in a layer-by-layer assembly around a solid core followed by thermal consolidation of the sol particles into a porous shell structure.[195] Preparation and the resulting morphology differ substantially from the mesoporous silica in the hierarchical silica monolith used earlier,[34] which has been prepared by sol–gel processing. We employed the reconstructions of the three materials to conduct MFDFT calculations of the molecular density distribution and thermodynamics during gas adsorption experiments. Based on the results, we demonstrate correlations between the shape of the hysteresis loop and the local morphology of the pore networks in these ordered and random mesoporous silicas.

4.2 Materials and methods

4.2.1 Mesoporous silica materials

Mesoporous Silica Materials. Details of the preparation, nitrogen physisorption analysis, and 3D physical reconstruction by electron tomography of the three mesoporous silica materials studied in this work have been reported before.[25,26] In those papers, the reconstructions were used as geometrical models in pore-scale simulations of hindered diffusion of finite-size solutes. The goal was to establish quantitative hindrance factor expressions that characterize the hindrance to diffusion originating from steric and hydrodynamic interactions between the finite-size solutes and the pore space confinement. The derived geometrical models are depicted in Figure 4.1 and relevant properties of these reconstructions and the corresponding powder samples are summarized in Table 4.1. The materials are purely mesoporous and characterized by the pore size distributions shown in Figure 4.7 (Supporting Information).

In view of the structural characteristics of the three materials, which are central to the discussion of their adsorption hysteresis loops, the involved material preparation steps and the morphological outcome are briefly reviewed. The synthesis of the ordered silicas relies on experience

[193] D. Zhao et al. , 279, 548–552, 1998.
[194] F. Kleitz, S. H. Choi, and R. Ryoo. *Chem. Commun.*, 0, 2136–2137, 2003.
[195] R. Hayes et al. *J. Chromatogr. A*, 1357, 36–52, 2014.
[25] S.-J. Reich et al. *Micropor. Mesopor. Mat.*, 282, 188–196, 2019.
[26] J. Hochstrasser et al. *Phys. Chem. Chem. Phys.*, 22, 11314–11326, 2020.

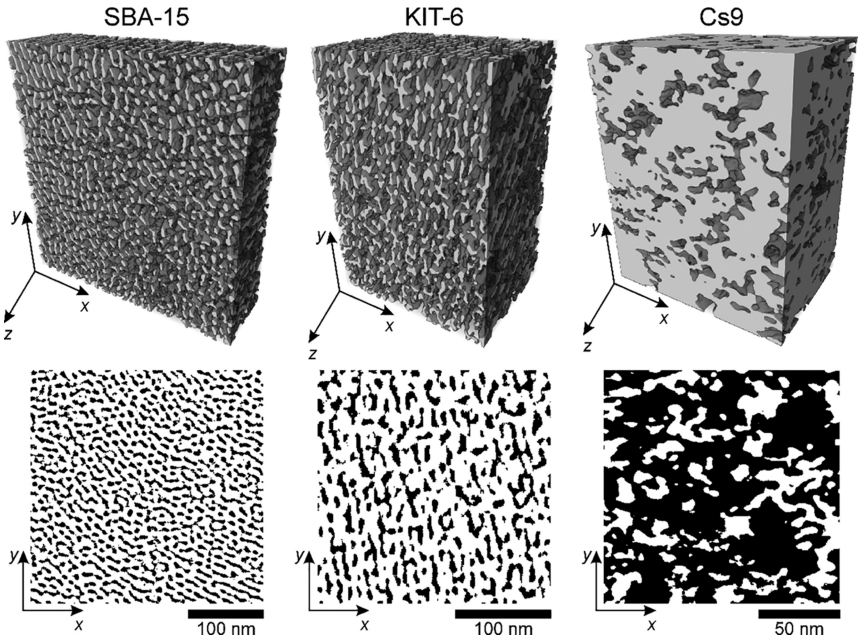

Figure 4.1: (Top row) 3D reconstructions obtained by electron tomography of the mesopore space morphologies considered in this work. SBA-15 and KIT-6 are large-pore ordered mesoporous silicas, whereas sample Cs9 is a random mesoporous silica from the shell of a core–shell particle. (Bottom row) 2D slices from the reconstructions (black–solid, white–void). Note the much lower porosity of sample Cs9 compared with the ordered silicas (cf. Table 4.1).

with systematically varied preparation conditions to induce desired morphological changes.[196,197] This is achieved by adding an organic silica source at a controlled temperature to a dilute, acidic, aqueous, micellar solution of an amphiphilic, nonionic, triblock copolymer (Pluronic P123, for SBA-15) or a blend of Pluronic P123 and n-butanol (for KIT-6) functioning as the structure-directing agent. This mixture is kept for $\sim$24 h at the starting temperature before hydrothermal treatment at higher temperature occurs. Afterward, the structure-directing agent is removed by extraction and the synthesis is finished by calcination. Because of the interaction between the

Table 4.1: Properties of the Reconstructions and Powder Samples.

	SBA-15	KIT-6	Cs9
reconstruction size ($x \times y \times z$) [nm^3]	$337 \times 319 \times 97$	$356 \times 245 \times 181$	$147 \times 183 \times 104$
reconstruction volume [nm^3]	10.4×10^6	15.9×10^6	2.8×10^6
voxel size [nm]	0.94	0.94	0.46
porosity [–][a]	0.69	0.70	0.29
S_{BET} [m^2 g^{-1}][b]	632	524	110
V_{total} [cm^3 g^{-1}][b]	1.22	1.37	0.25
mean pore size [nm][b]	9.1	10.5	9.4

[a]Void volume fraction (mesoporosity) extracted directly from the 3D physical reconstructions shown in Figure 4.1.
[b]Specific surface area (S_{BET}), total pore volume (V_{total}), and mean mesopore diameter (mode) from nitrogen physisorption analysis.

[196] F. Kleitz et al. *J. Phys. Chem. C*, 114, 9344–9355, 2010.
[197] R. Guillet-Nicolas et al. *J. Phys. Chem. C*, 121, 24505–24526, 2017.

hydrophilic poly(ethylene oxide) chains of Pluronic P123 and the polymerizing silica species, some chains are finally trapped in the silica walls. Therefore, after removal of the copolymer, the materials contain intrawall pores (with size and volume depending on the temperature and duration of the hydrothermal treatment).[198]

Preparation conditions for SBA-15 and KIT-6 silicas in previous work have been optimized to widen the intrawall pores toward the size of the primary mesopores.[26] This is indicated in Figure 4.7, which reveals narrow mesopore size distributions for both materials with only $\sim 10\,\%$ relative standard deviation and negligible tailing. (If not properly widened, smaller intrawall mesopores cause a low-amplitude tailing of the pore size distribution to the left.[7]) The primary mesopore system in KIT-6 silica consists of two continuous, interwoven, 3D subnetworks separated by an amorphous silica wall believed to follow the infinite periodic minimal surface.[194] As shown in our previous work,[26] the primary pore system in the KIT-6 silica sample is relatively open, uniform, and unobstructed and connections between the two 3D subnetworks are established by intrawall mesopores. In contrast, for the SBA-15 silica sample, widening of the intrawall pores toward the size of the hexagonally arranged primary mesopores (forming a pseudo-one-dimensional pore system) was essential to create a highly interconnected, 3D mesopore network.[26]

The reconstructions of these two ordered silicas are complemented by a random mesoporous silica from the mesoporous shell of a core–shell particle (Figure 4.1).[25] This material is denoted as Cs9 in recognition of its mean pore diameter (cf. Table 4.1). Core–shell silica particles have gained popularity as packing materials for high-performance liquid chromatography columns.[199] The basic particle architecture is a solid (impermeable) silica core surrounded by a mesoporous silica shell. The latter is based on a layer-by-layer assembly of nanoparticles onto the core.[195] Particles are made by first binding an organic polyelectrolyte to the solid core and the coated core particles are then immersed in a dispersion of nanoparticles with opposite charge as the polyelectrolyte. These steps are repeated until the targeted shell thickness is reached. Afterward, particles are heated to remove the polyelectrolyte and fuse the shell onto the core. Thus, the shell morphology is strongly influenced by the consolidation processes occurring during the fusion step. On the one hand, consolidation is important to improve the integrity and strength of the particles so that they can withstand subsequent surface modification and column packing procedures.[200] On the other hand, since the shell forms by consolidation of individual layers of sol particles, its morphology reflects structural features of compacted and sintered packings with narrow and highly constricted pores as well as a wide range of pore sizes. For example, the 3D reconstruction for sample Cs9 has revealed an increased number of small pores connecting larger ones with configurations similar to an ink-bottle geometry.[25] The resulting structural heterogeneity is evidenced by the much wider pore size distribution ($\sim 40\,\%$ relative standard deviation, Figure 4.7) compared with the ordered silicas. This striking difference regarding pore

[198] T. Kjellman and V. Alfredsson. *Chem. Soc. Rev.*, 42, 3777–3791, 2013.
[7] S.-J. Reich et al. *J. Phys. Chem. C*, 122, 12350–12361, 2018.
[199] G. Guiochon and F. Gritti. *J. Chromatogr. A*, 1218, 1915–1938, 2011.
[200] L. E. Blue and J. W. Jorgenson. *J. Chromatogr. A*, 1218, 7989–7995, 2011.

size distributions becomes immediately visible in the 2D slices shown in Figure 4.1.

4.2.2 Lattice model and MFDFT

The three geometrical models shown in Figure 4.1 were adapted for pore-scale MFDFT calculations of adsorption and desorption. For that purpose, we employed a single occupancy, nearest-neighbor lattice gas model for which, in mean field theory, the grand free energy is given by[118,186]

$$\Omega = k_{\mathrm{B}}T \sum_i \left[(\rho_i \ln \rho_i) + (1-\rho_i)\ln(1-\rho_i)\right] - \epsilon_{\mathrm{ff}} {\sum_{i<j}}' \rho_i \rho_j + \sum_i \rho_i(\phi_i - \mu) \tag{4.1}$$

where T is the absolute temperature, k_{B} is the Boltzmann constant, ρ_i is the average fluid density at site i, $-\epsilon_{\mathrm{ff}}$ is the attraction energy between fluid molecules on nearest-neighbor sites, ϕ_i is the external field associated with the fluid–solid interaction and is a nearest-neighbor attraction with energy $\epsilon_{\mathrm{fs}} = -\alpha\epsilon_{\mathrm{ff}}$, and μ is the chemical potential of the fluid. The primed sum denotes restriction to pairs of sites that are nearest neighbors and which are not occupied by the solid. The parameter α represents the relative interaction strength for a fluid molecule with the solid surface and generally accounts for both the nearest-neighbor interactions and the longer-ranged interactions integrated across the width and depth of the solid.

The necessary condition for a minimum in Ω is obtained by setting its partial derivatives with respect to ρ_i's to zero, leading to the following set of nonlinear equations:

$$k_{\mathrm{B}}T \ln\left[\frac{\rho_i}{(1-\rho_i)}\right] - \epsilon_{\mathrm{ff}} {\sum_{j}}' \rho_j + \phi_i - \mu = 0 \quad \forall i \tag{4.2}$$

These equations were solved by fixed-point iteration starting from an initial estimate of the density distribution. To study an adsorption isotherm of average density versus relative pressure (p/p_0), we start from a low-pressure (low chemical potential) state corresponding to a low-adsorption vapor-like state in the porous material (initial state, $p/p_0 \to 0$). We then solve for increasing values of chemical potential up to the value for the bulk saturated vapor ($\mu_0 = -3k_{\mathrm{B}}T$ for a simple cubic lattice), using the solution from the previous state as initial estimate for the next solution. For a desorption isotherm, we start from the final state on the adsorption branch and follow a sequence of states of decreasing chemical potential until the original low chemical potential state is achieved.

Implementation of the described lattice MFDFT approach with the geometrical models of the samples shown in Figure 4.1 is similar to our previous work.[34] To optimize agreement with the experiment, we constructed spatial grids with coarse-grained lattice units (details in the next section). The three geometrical models required individual lattice-constant sizes, probably because of the structural differences between the silica surfaces, which affect fluid–solid inter-

action. MFDFT calculations were implemented using the parallel programming platform CUDA, similar to the work described by Schneider and Valiullin.[192] Before solving the equations, we surrounded each lattice porous system by a bulk layer of 10 voxels to provide a realistic description of the desorption branch. As a criterion for equilibrium achieved with the iterative approach, we compared maximal density fluctuations of the corresponding voxels between iterations with a chosen threshold (10^{-6} in our case). When the calculation for a given pressure was finished, we removed the entire bulk layer enveloping a reconstruction as well as an outer layer of the porous structure (15 voxels wide) to reduce boundary effects. Only then was the density distribution used to calculate the corresponding point of the adsorption or desorption isotherm at that pressure. For a quantitative comparison, we normalized densities so that upper closure points of the hysteresis loops for the calculations and experiment coincided.

4.2.3 Choice of modeling parameters

It should be noted that MFDFT is approximate and the lattice model is coarse grained. Direct quantitative agreement with the experiment should therefore not be expected. However, if the shape of the hysteresis loop is similar to that from the experiment, the fluid morphologies from MFDFT will signify the phenomena occurring in the real systems. No other theory or simulation is feasible for these complex 3D systems. The following parameters were adjusted to achieve best qualitative agreement in the hysteresis region between the adsorption–desorption isotherms generated by MFDFT and experimental physisorption data: (i) the reduced temperature $T* = k_{\mathrm{B}}T/\epsilon_{\mathrm{ff}}$, (ii) the ratio α between the energies of fluid–solid and fluid–fluid interactions, and (iii) the lattice unit size.

Lattice unit size.

We used ImageJ[201] to adjust lattice dimensions and prepare image stacks with different lattice-unit sizes by reducing the number of voxels in all three dimensions by factors in a range from 0.5 to 1 (step size, 0.05). During that process, the same structure is represented with fewer lattice units and each lattice unit therefore represents a greater length in metric units than a voxel in the reconstruction. Rescaling was conducted using a bicubic interpolation implemented in ImageJ. Afterward, a grayscale image stack was obtained for which a threshold was applied in order to reach a porosity as close as possible to the original reconstruction. Calculating isotherms with increasing lattice unit size caused the lower closure point to move upward and to the left, so that the hysteresis experienced a clockwise rotation (with fixed upper closure point) and a slight shift to lower pressures.

Reduced temperature.

We explored reduced temperatures T^* in a range from 0.5 to 1.3. This parameter leaves the isotherm shape almost unaffected at low pressures but has a pronounced influence on the hysteresis. Changing the temperature has a similar effect on hysteresis as it does on the bulk va-

[201] C. A. Schneider, W. S. Rasband, and K. W. Eliceiri. *Nat. Methods*, 9, 671–675, 2012.

Table 4.2: Parameters Used in the Lattice MFDFT Model

	SBA-15	KIT-6	Cs9
$\epsilon_{fs}/\epsilon_{ff}$ [–]	1.9	1.2	1.3
T^* [–]	0.87	0.87	0.87
lattice unit size [nm]	1.04	1.34	0.71

por–liquid coexistence, particularly with regard to the difference between binodal and spinodal lines which merge at the critical temperature. A decrease in temperature causes a widening of the hysteresis region and a slight shift to lower pressures. With increasing temperature, a gradual disappearance of the hysteresis loop was noticed. It can be explained by the fact that with increasing temperature the barriers associated with nucleation of the liquid phase (leading to metastable states of the pore fluid) decrease, thus narrowing the hysteresis region. In addition, at high temperatures, the capillary condensed fluid is lower in density and the vapor-like fluid is higher in density, causing a decrease in the change of adsorbed amount associated with condensation/evaporation, which further affects the hysteresis region. There is no phase transition-like behavior at low pressures for temperatures studied here. The pore condensation/evaporation step in the isotherms will become less steep as temperature increases, but the effect is smaller than the effects in the hysteresis region. The loop also moves to higher pressures and its lower closure point rises. The ratio between $77\,\mathrm{K}$ and the critical temperature of nitrogen ($126.2\,\mathrm{K}$) is ~ 0.6. Therefore, taking into account that the critical temperature for our lattice model is $T_c^* = 1.5$, we focused on reduced temperatures around $T^* = 0.9$ and obtained the best agreement between the calculated and experimental physisorption isotherms for all three structures with $T^* = 0.87$.

Fluid–wall to fluid–fluid interaction ratio.

We applied values of α ranging from 1.1 to 5.0. This parameter has an impact mainly on the density values at lower pressure and regulates the steepness of the part of the isotherm associated with monolayer formation. The fluid–solid interaction has the most effect on the fluid near the pore walls and the local density there. Increasing α causes a growth of density at relative pressures below the lower closure point, leaving the hysteresis region unaffected. The hysteresis is associated with condensation/evaporation, which is controlled primarily by the confinement (local pore size) in the system.

These considerations illustrate that the three parameters influence physisorption differently. On the other hand, the parameters are not completely independent from each other regarding their impact on the adsorption–desorption isotherms. For this work, we explored parameters on a grid and chose the set of parameters that provided the best visual agreement between simulated and experimental isotherms in the hysteresis region. The resulting parameter values are summarized in Table 4.2 and we return to their discussion below. Figure 4.8 (Supporting Information) illustrates the response of the computed isotherms to the variation of the three model parameters.

4.3 Results and discussion

We used the single occupancy lattice gas model with nearest-neighbor interactions introduced in Section 4.2 to simulate adsorption and desorption in the three reconstructions shown in Figure 4.1. To carry out calculations for one reconstruction, we first gradually increased relative pressure from a value close to zero ($p/p_0 = 0.0018$) with an increment of $p/p_0 = 0.002$ up to unity and then decreased it with the same increment down to the initial value. For each relative pressure value, we ran iterative calculations until equilibrium or metastable equilibrium states were achieved, and 500 pressure values were analyzed in the range of $0 < p/p_0 \leq 1$ for both adsorption and desorption. This large number of data points allows us to resolve subtle features of the calculated isotherms. Each data point required iterative calculations, which result in an equilibrium distribution of liquid in the mesopore space according to a given pressure. Initially, the entire void space of a reconstruction is free of liquid. After every calculation, the void space becomes filled with additional liquid. Each lattice unit of the void space is characterized by a liquid density in the range between 0 and 1. Further analysis requires introducing a criterion to distinguish lattice units filled with either gas phase or liquid phase. For this purpose, we considered normalized density as a probability of occupying a lattice unit with liquid and set a threshold of 0.5, i.e., a lattice unit with normalized density below 0.5 becomes a lattice unit filled with gas phase ("gas lattice unit") and a "liquid lattice unit" otherwise. Figure 4.9 (Supporting Information) shows that this threshold value allows a clear differentiation between lattice units associated with either gas phase or liquid phase.

In previous work,[34] we have demonstrated good qualitative agreement between experimental isotherms for a mesoporous silica sample prepared by sol–gel processing and isotherms obtained by the described approach using lattice MFDFT implemented with the 3D reconstruction of the pore space morphology. However, we did not further examine the parameters of the lattice-gas model for their optimal values and the relation to their physical nature. Through the availability of more than one silica reconstruction along with the results of the physisorption experiments conducted under identical conditions (for nitrogen at $77\,\mathrm{K}$), it now becomes possible to gain a deeper insight.

With reference to the experimental isotherms, we have conducted a screening for the parameters T^* and $\epsilon_{\mathrm{fs}}/\epsilon_{\mathrm{ff}}$. Best agreement between experimental and calculated isotherms in the hysteresis region (Figure 4.2) was obtained for a reduced temperature of 0.87 (all reconstructions) and a ratio of $\alpha = \epsilon_{\mathrm{fs}}/\epsilon_{\mathrm{ff}}$ of 1.9, 1.2 and 1.3 for SBA-15, KIT-6, and Cs9, respectively (Table 4.2). Calculated isotherms show good agreement with their experimental references in the hysteresis region (bottom row in Figure 4.2). These results consistently identify type IV(a) isotherms with H1 hysteresis loops for the ordered silicas and H2(a) hysteresis loop for the random silica.[92] The isotherms reveal steep capillary condensation and evaporation steps at high relative pressures, in a p/p_0-range of about 0.7–0.8. Hysteresis loops are particularly narrow and hysteresis branches parallel and almost vertical for the ordered materials. This indicates

[92] M. Thommes et al. *Pure Appl. Chem.*, 87, 1051–1069, 2015.

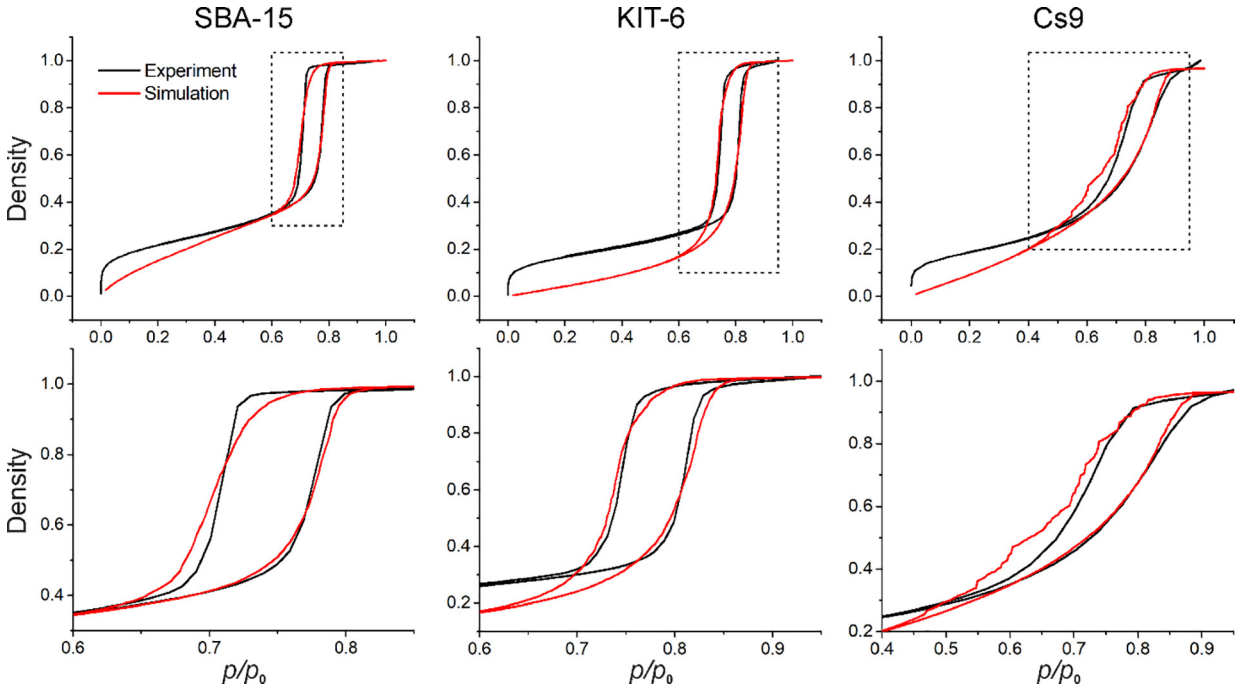

Figure 4.2: (Top row) Experimental (black lines) and simulated sorption isotherms (red lines) for the three reconstructed mesoporous silica materials (cf. Figure 4.1). Dashed rectangles indicate the hysteresis regions shown enlarged in the bottom row.

homogeneous pore structures with large, well defined mesopores and confirms that the SBA-15 silica sample is characterized by a highly interconnected 3D mesopore network, mimicking the pristine 3D mesopore structure of the KIT-6 silica in this regard.[26,197]

A constant reduced temperature T^* in MFDFT with all three materials is related to the identical physical temperature of 77 K encountered in the physisorption experiments. At the same time, the differentiation of α-values is not unexpected, because the fluid–solid interaction energies ϵ_{fs} depend on structural details of the silica surfaces, which naturally vary for different materials with individual preparation and post-treatment histories. We point out that the α-values giving best agreement between experimental and calculated isotherms in the hysteresis region are comparable to theoretical estimates summarized in Table 4.3.[202–207]

While calculated isotherms shown in Figure 4.2 demonstrate good agreement with experimental data in the hysteresis region, they underestimate densities at pressures below the lower closure point of the hysteresis loop. As discussed previously,[34] better agreement at lower pressures can be achieved by a variation of the model parameters, however, this is accompanied by a loss

[202] M. W. Maddox, J. P. Olivier, and K. E. Gubbins. *Langmuir*, 13, 1737–1745, 1997.
[203] A. Brodka and T. W. Zerda. *J. Chem. Phys.*, 95, 3710–3718, 1991.
[204] M. Miyahara et al. *Langmuir*, 16, 4293–4299, 2000.
[205] F. Cuadros, I. Cachadiña, and W. Ahumada. *Mol. Eng.*, 6, 319–325, 1996.
[206] M. S. Ananth, K. E. Gubbins, and C. G. Gray. *Mol. Phys.*, 28, 1005–1030, 1974.
[207] P. I. Ravikovitch et al. *Langmuir*, 16, 2311–2320, 2000.

Table 4.3: Estimated values for $\alpha = \epsilon_{fs}/\epsilon_{ff}$[a]

	$\epsilon_{OO}/k_B = 164.13\,K$[202]	$\epsilon_{OO}/k_B = 230.0\,K$[203]
$\epsilon_{NN}/k_B = 95.2\,K$[202]	1.31	1.55
$\epsilon_{NN}/k_B = 95.0\,K$[204]	1.31	1.56
$\epsilon_{NN}/k_B = 91.85\,K$[205]	1.37	1.58
$\epsilon_{NN}/k_B = 99.5\,K$[206]	1.28	1.52
$\epsilon_{NN}/k_B = 94.45\,K$[207]	1.32	1.56

[a]Calculated with the Berthelot combining rule using interaction energies between the two nitrogen atoms of the adsorptive nitrogen (ϵ_{NN}) and between two oxygen atoms of the adsorbent silica (ϵ_{OO}), assuming Lennard-Jones potentials.

of accuracy in the hysteresis region. An explanation for this discrepancy between experimental and calculated isotherms may be found in the simplifications of the lattice-gas model. We applied an interaction potential that is only based on nearest-neighbor interactions instead of adapting more accurate (but also more complex) models of molecular interactions.

We note two peculiarities of the calculated desorption branch for the core–shell material. First, an upward deviation of the liquid density with respect to the experimental data for pressures in a range of $p/p_0 = 0.50$–0.75, and second, the presence of irregular density jumps in the hysteresis region. The density deviation may be caused by the small volume of the crumb used in the reconstruction process compared to the relatively large amount of material in the physisorption experiment. With increasing size of the reconstructed core–shell silica sample (or number of reconstructed crumbs), the calculated (averaged) isotherms should approach the experimental data. This issue is discussed further below. In contrast, for the ordered silicas with regular mesopore space morphologies, the small crumbs suffice to reproduce relevant morphological features of the bulk powder samples, resulting in the good agreement between calculated and experimental data in the hysteresis region (seen in the bottom row of Figure 4.2).

To reveal the nature of the second peculiarity for sample Cs9, we analyzed the differences in the available density distributions for neighboring points (pressure values) that characterize the density jumps in the desorption isotherm. This is illustrated in Figure 4.3, where we select three pairs of neighboring points representing different jump heights (amplitudes of density changes). Associated changes in the liquid-phase distributions are visualized in the three boxes shown in Figure 4.3, which highlight pore volumes in the structure that become emptied upon the respective pressure decrement. The largest density jump occurs for a change in relative pressure from 0.7393 to 0.7372 (right box). Here, the major amount of liquid leaving the reconstruction (forming new volume filled with the gas phase) is located in a single, large region. In contrast, the smoother transition associated with the change from $p/p_0 = 0.6513$ to 0.6492 is characterized by a large number of smaller newly formed gas volumes (central box). The third transition highlighted in Figure 4.3 (change from $p/p0 = 0.4687$ to 0.4667) basically results in two moderately large gas-filled volumes (left box), which together cause a noticeable density jump. Analysis of the liquid-phase distributions for the transitions revealed that the newly formed gas volumes were always connected to the external faces of the geometrical model, so that the abrupt changes in the liquidphase distributions do not represent cavitation but pore-blocking induced evaporation.

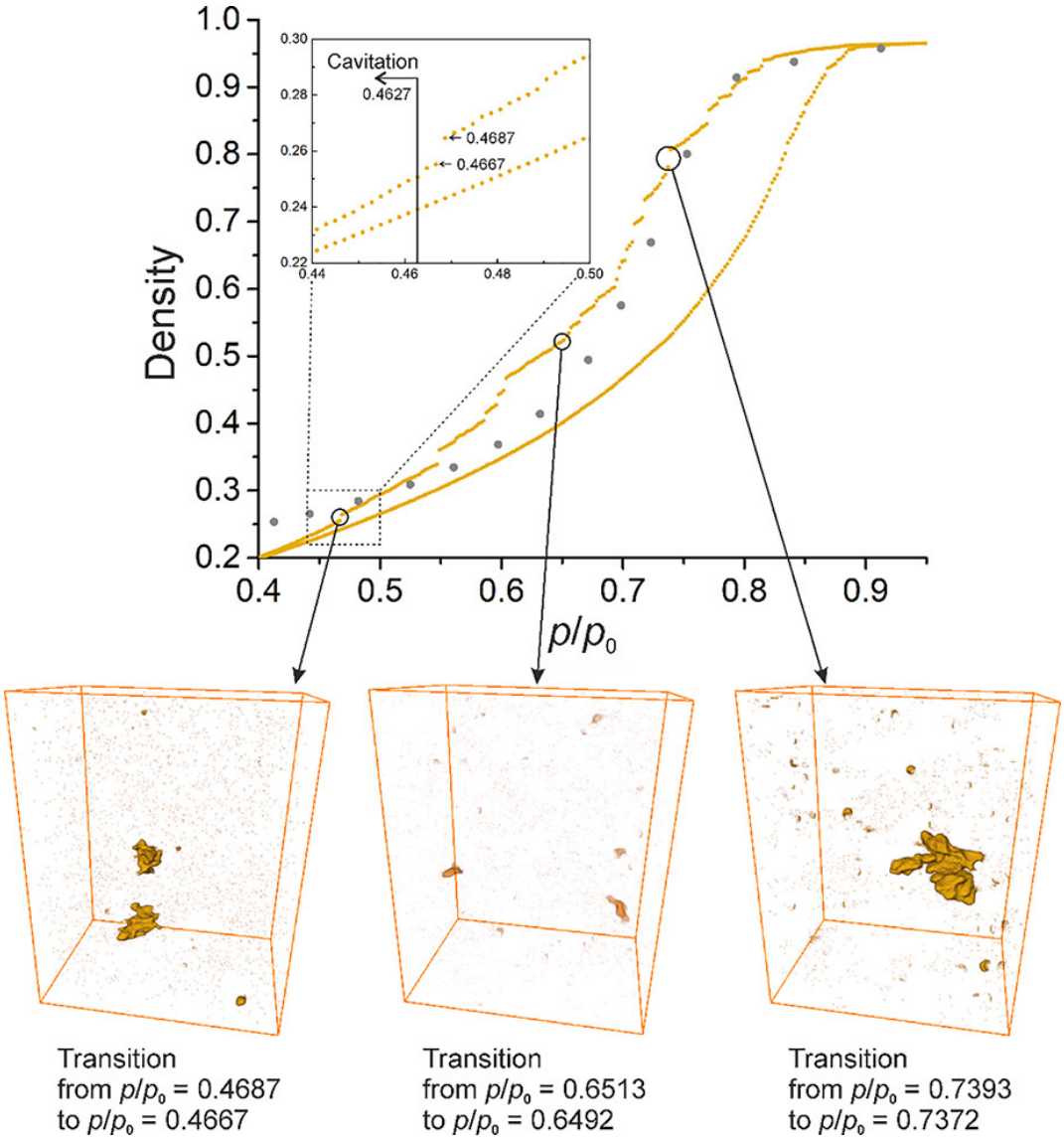

Figure 4.3: Calculated hysteresis loop for sample Cs9 (orange dots) and experimental data of the desorption isotherm (grey points). The inset is a magnified image of the region where cavitation begins. The three boxes (bottom row) highlight the pore volumes that are emptied during desorption, reflecting the density jumps that accompany the indicated changes in relative pressure. These newly formed voids are connected to the external faces of the Cs9 reconstruction and therefore do not represent cavitation.

The lack of smoothness of the MFDFT desorption isotherm for sample Cs9, which can be related to sudden passages between metastable states (the associated jumps are cooperative processes referred to as avalanches);[208] is resolved in detail here because of the large number of calculated points that allow quasi-continuous screening of the system states as a function of relative pressure. In experiments, by contrast, the number of data points is typically much lower, as illustrated with the grey points included in Figure 4.3 (experimental data of the desorption isotherm). Therefore, the lack of smoothness may remain undetected in practice. For example, by removing major parts of the points from the calculated desorption isotherm, the remaining points also suggest a smooth curve shape. The ability to observe this behavior may also reflect the much smaller size of the reconstructed sample (Table 4.1) compared to sample volumes typically encountered in physisorption experiments. As a consequence, the resulting finite-size effects allow us to resolve phenomena originating in the local morphology (disorder) of a material. In this way, the avalanches noticed for the desorption isotherm shown in Figure 4.3 can be related to the heterogeneous pore structure of sample Cs9.

The heterogeneous pore structure of sample Cs9 contrasts with the homogeneous SBA-15 and KIT-6 materials (Figure 4.1);[26] which are characterized by well-defined mesopores of relatively uniform size (Figure 4.7). With increasing sample volume, we expect the structural heterogeneity of the core–shell material and the associated submacroscopic avalanches (cf. Figure 4.3) to become effectively averaged, so that ultimately smooth isotherms are obtained. At the same time, the averaging will obscure the insightful analysis of structural features and phenomena prevailing in finite-size systems, such as avalanches remaining at a mesoscopic scale and their dependence on both material properties (porosity, disorder, and wettability) and reduced temperature.

Importantly, cavitation (discussed in more depth below) does not occur at pressures for which we observed the jumpy pattern of the desorption isotherm shown in Figure 4.3. The first cavitation event is detected at $p/p_0 = 0.4627$, that is, after the last sharp density jump from $p/p_0 = 0.4687$ to 0.4667 (inset in Figure 4.3). This value for the onset of cavitation agrees with a theoretical estimate of the upper bound for the pressure range in which cavitation should be observed with nitrogen at $77\,\mathrm{K}$.[113] Beginning with $p/p0 = 0.4627$ and moving toward the lower closure point of the hysteresis loop, we determined the volume of each cavity (gas volume confined by liquid) that formed in the geometrical model of sample Cs9. We then characterized these gas volumes, which generally had an irregular shape, by their equivalent sphere diameters and used this transformation to estimate the average distance from the center of each cavity to the local pore boundaries. In our calculations, gas cavities were separated from the solid silica walls usually by a single "lattice unit" layer of liquid. To receive an estimate of the size of the pore in which a cavity is formed, we therefore added to the corresponding equivalent sphere diameter twice the voxel (lattice unit) size for sample Cs9 ($1.42\,\mathrm{nm}$).

With this approach, we analyzed the relationship between relative pressure and the size of

[208] F. Detcheverry et al. *Adsorption*, 11, 115–119, 2005.
[113] M. Thommes et al. *Langmuir*, 22, 756–764, 2006.

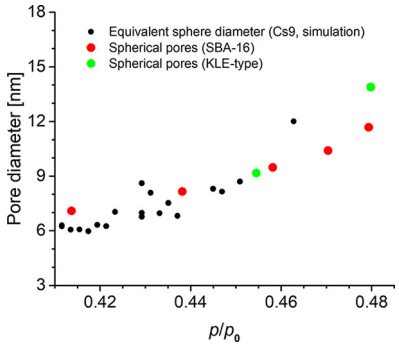

Figure 4.4: Dependence of the cavitation pore diameter on relative pressure. Black circles represent the results based on the simulations for sample Cs9, and red and green circles are experimental data obtained for different silicas with spherical pores.[209]

the pores in which cavitation occurred during desorption. The results of this analysis are shown in Figure 4.4 (black circles) and a comparison is made with the work of Rasmussen et al.[209] Our data show excellent agreement with that of the experimental analysis for model materials containing well-defined spherical pores. This is encouraging because an important difference between the experimental analysis and our simulation based results is that each experiment represents a powder sample with a large number of similar pore geometries disposed to cavitation. Then, a clear macroscopic jump is observed in the experiment during desorption because many pores experience cavitation within a narrow pressure range. The data shown in Figure 4.4 based on the simulations, on the other hand, were determined for a small geometrical model with relatively few pores and a heterogeneous microstructure. A uniform cavitation jump in the calculated desorption isotherm is therefore not observed. However, with the digital snapshots of the liquid-phase distributions at hand, we could still record the locally occurring cavitation bubbles as a function of relative pressure along the desorption branch (Figure 4.4) by image analysis.

To take a closer look at cavitation locally in the microstructure, we focused on the largest pore associated with the data shown in Figure 4.4. This pore has one bottleneck, which presents the only transport pathway into and out of the pore body. The dimensions of the bottleneck (cross-sectional size, $1.42\,\mathrm{nm}$) and pore body (equivalent sphere diameter, $\sim 12\,\mathrm{nm}$) are consistent with geometries underlying cavitation found in the literature.[113] As highlighted in Figure 4.5, the pore is located deep inside the reconstruction and has no direct connection to the external bulk region (see 3D representation in the top left box). We then extracted the entire pore configuration with the bottleneck and conducted a simulation of physical adsorption for this geometry. Pore emptying (gas formation) occurred at a relative pressure of 0.4627 for the pore configuration within the reconstruction as well as for the extracted geometry. The bottleneck remained saturated with liquid in both cases. State 1 and the green isotherms shown in Figure 4.5 represent this cavitation event in the extracted pore-bottleneck geometry. In the next step, we removed the bottleneck and repeated the calculations (state 2 and red isotherms). We now observed a significant narrowing of the hysteresis loop and also noticed that the new pore entrance

[209] C. J. Rasmussen et al. *Langmuir*, 26, 10147–10157, 2010.

remained free of liquid after the pore has been emptied. Though the bottleneck was removed, some constriction with respect to the size of the pore body still occurred and we therefore refer to that situation as pore blocking. After this scenario, five more (one-voxel-thick) slices were removed from the actual pore geometry to widen the pore entrance further toward the size of the pore body (state 3 in Figure 4.5). Calculations for this geometry (blue isotherms) reveal that the desorption branch is getting close to the adsorption branch and that the hysteresis region is about to collapse. Continued widening of the pore entrance may yield a single, completely reversible type IV(b) isotherm as expected for conical and cylindrical mesopores closed at the tapered end.[92]

After we analyzed the hysteresis loops (Figure 4.2) and interpreted the results in view of the different mesoporous silica microstructures, we complemented the boundary isotherms of all materials by calculated desorption scans to further resolve the impact of the different morphologies. Desorption scanning means that after calculation of the initial adsorption–desorption isotherms, the adsorption is calculated only up to a relative pressure associated with a partial filling of the pores. Therefore, only a portion of the pore network in a material was filled with liquid before we started calculating the desorption isotherm, as illustrated in the top row of Figure 4.6 (black lines). The shape of the desorption scanning curves for the ordered silicas (SBA-15, KIT-6), which are characterized by mostly uniform, cylindrical pores and H1 hysteresis loop, essentially reflects pore evaporation as expected from an independent pore model, where the pores empty independently from each other.[8,93] The curve shape resembles the boundary desorption isotherms and the scans do not meet at the lower closure point but at the opposite boundary curve. When we complete desoption scans by an exemplary adsorption scan (bottom row in Figure 4.6), calculated by increasing the pressure from the desorption branch into the hysteresis loop again, ending at the adsorption boundary curve, then closed scanning loops are obtained for the ordered silicas. Experimental scanning adsorption and desorption isotherms reported for SBA-15 and KIT-6 silicas[8] are very similar to the calculated isotherms. Conversely, desorption scanning curves for the random silica Cs9 with many narrow, highly constricted pores and a H2 hysteresis loop converge at the lower closure point of the main hysteresis loop (Figure 4.6, top panel). They exhibit the behavior of dependent pores, involving pore blocking/percolation (cf. Figure 4.3). In a similar manner, the exemplarily calculated adsorption scan converges at the upper closure point of the main hysteresis loop (bottom panel in Figure 4.6), so that the scanning isotherms for the random silica do not form a closed hysteresis loop as observed for the ordered silicas.

4.4 Conclusions

A lattice MFDFT modeling approach has been successfully adapted to pore-scale simulations of adsorption and desorption of nitrogen at 77 K in geometrical models of three mesoporous silicas obtained by electron tomography. Optimization of model parameters (reduced temper-

[8] R. Cimino et al. *Colloid Surface A*, 437, 76–89, 2013.
[93] K. A. Cychosz et al. *Chem. Soc. Rev.*, 46, 389–414, 2017.

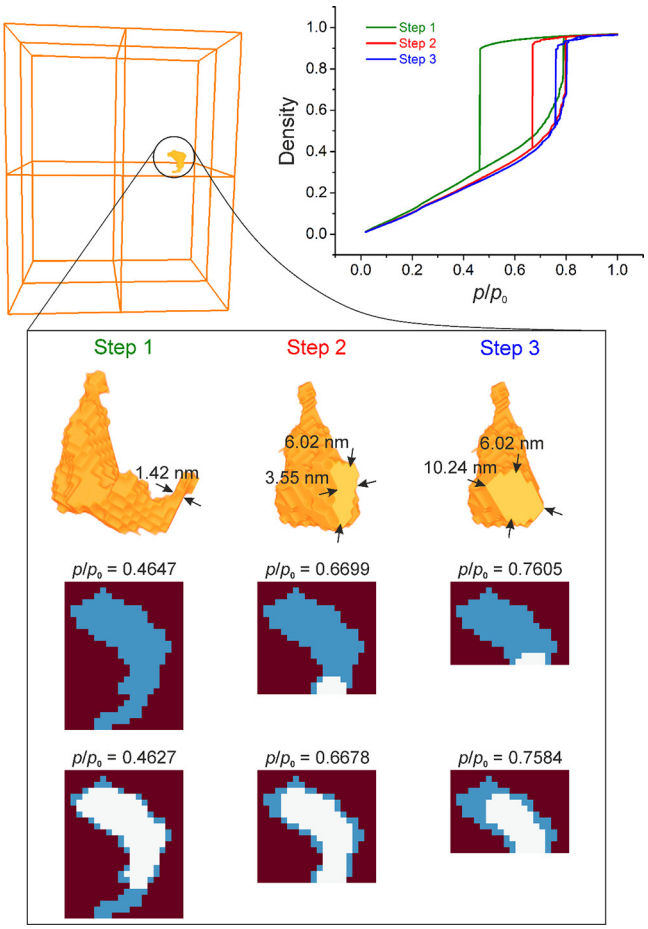

Figure 4.5: Dependence of hysteresis loop and phase distribution on the pore shape for the largest pore geometry with cavitation in the reconstructed Cs9 sample (occurring at $p/p_0 = 0.4627$, cf. Figure 4.4). The pore and its location in the reconstruction are indicated in the top left panel. This pore with the bottleneck was extracted from the reconstruction and sorption isotherms were then calculated for the original geometry (with bottleneck, step 1) as well as for modifications without the bottleneck and widened pore entrances (steps 2 and 3). The resulting three geometries are illustrated in the central row (orange) and the top right panel compares associated hysteresis loops. Bottom rows visualize phase distributions in a 2D slice from the three pore geometries at the indicated relative pressures (black–solid, blue–liquid, and white–gas).

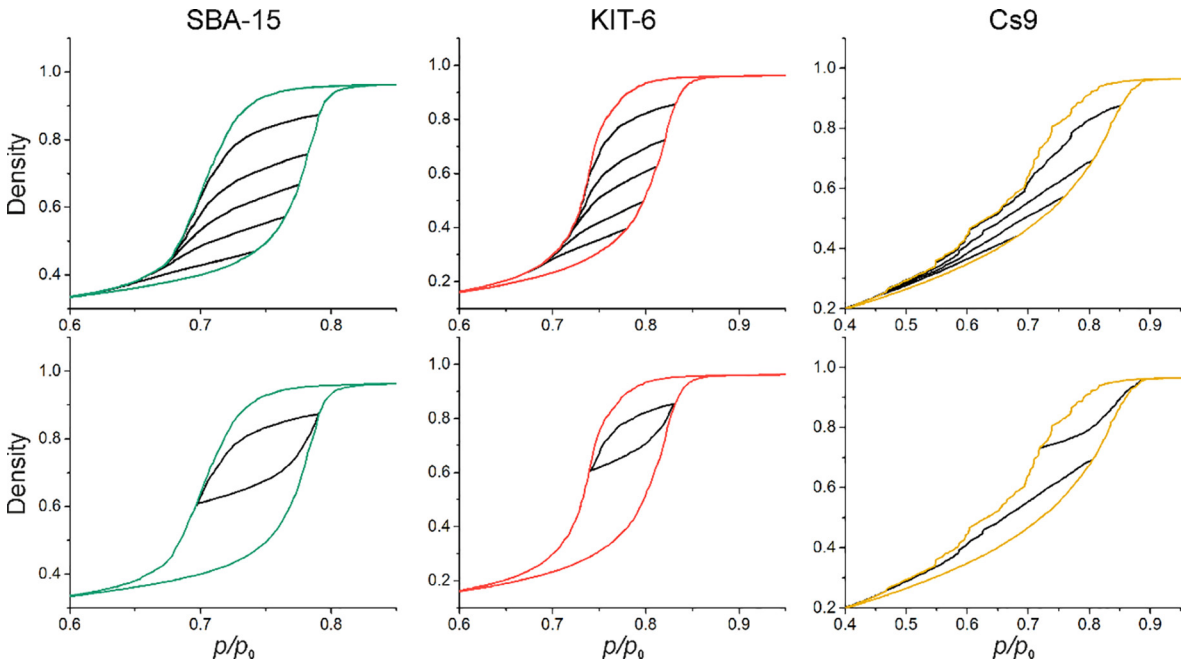

Figure 4.6: (Top row) Desorption scanning curves (black lines) calculated for the reconstructions shown in Figure 4.1. (Bottom row) Scanning adsorption–desorption isotherms (black lines), revealing closed loops for materials with H1 hysteresis (SBA-15, KIT-6). By contrast, scanning isotherms approach upper and lower closure points of the main hysteresis loop of type H2 (Cs9).

ature, ratio between the energies of fluid–solid and fluid–fluid interactions, and lattice unit size) allowed us to achieve good qualitative agreement between calculated and experimental isotherms, with focus on the hysteresis region. This consistently revealed type IV(a) isotherms with a H1 hysteresis loop for the two ordered silicas (SBA-15, KIT-6) and a H2(a) hysteresis loop for the random silica. Boundary isotherms were complemented by calculated adsorption and desorption scanning curves. They demonstrate behavior of independent pores for the ordered silicas, resulting in closed scanning hysteresis loops, and behavior of dependent pores for the random silica, where adsorption and desorption scans converge at the upper and lower closure points, respectively, of the main hysteresis loop. Observations based on the lattice MFDFT calculations and conclusions about the microstructure of the mesoporous silicas are consistent with the independent morphological analysis of the three materials. We identified homogeneous microstructures for the SBA-15 and KIT-6 silica samples, characterized by highly interconnected 3D mesopore networks of uniform, cylindrical pores with narrow pore size distributions ($\sim$10 % relative standard deviation).[26] The random silica revealed a heterogeneous microstructure, exhibiting features of compacted and sintered packings with narrow and highly constricted pores (with ink-bottle geometry) as well as a wide range of pore sizes reflected in a much wider pore size distribution with $\sim$40 % relative standard deviation.[25]

In addition to the isotherms, the lattice MFDFT model provides 3D distributions of the gas phase and liquid phase in a material for each calculated state. This information was used

to analyze pore blocking and cavitation occurring locally in the heterogeneous structure of the random silica along the desorption boundary curve and to quantify the dependence of the cavitation bubble size on relative pressure by direct image analysis. In the future, similar studies relying on the presented reconstruction–simulation approach are expected to improve the diagnostic value of scanning isotherms by resolving the interplay between thermodynamics and the microstructure in a variety of materials and establishing relationships between morphological properties of the pore networks and details of the hysteresis behavior.

Acknowledgments The authors thank Dr. D. Schneider and Professor R. Valiullin (Universität Leipzig) for having distributed the numerical code used for work reported in ref.[192]

4.5 Supporting information

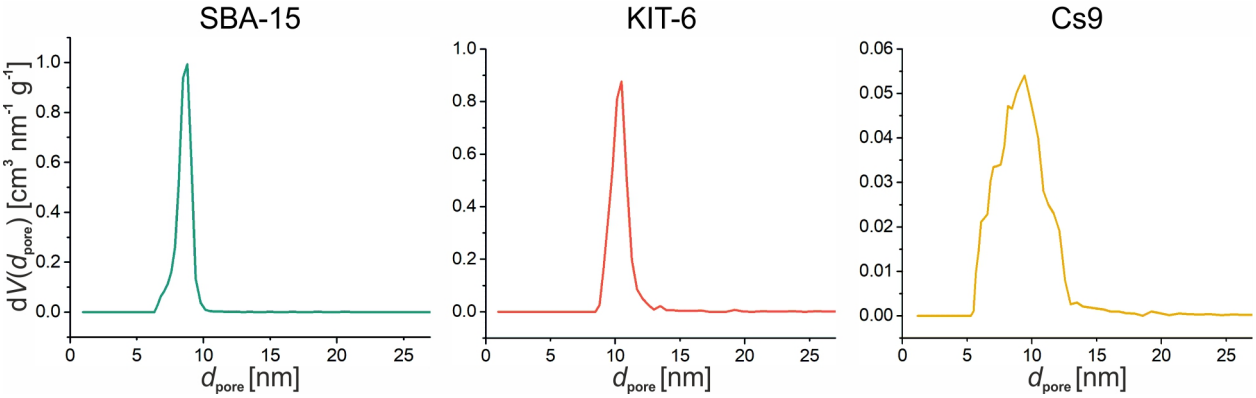

Figure 4.7: Experimental pore size distributions of the three mesoporous silica materials derived from NLDFT analysis of the adsorption isotherms.[25,26]

These SBA-15 and KIT-6 silica samples are home-made and have been adopted from our previous work,[26] while core–shell (Fused-Core®) particles with a nominal mesopore diameter of $9\,\mathrm{nm}$ used in previous work[25] have been purchased from Advanced Materials Technology (Wilmington, DE). The pore size distributions in Figure 4.7 are based on nitrogen physisorption data recorded at $-196\,^{\circ}\mathrm{C}$ on an Autosorb-iQ2 sorption analyzer (Quantachrome Instruments, Boynton Beach, FL) in case of the SBA-15 and KIT-6 samples[26] and on a Thermo Scientific Surfer gas adsorption porosimeter (Thermo Fisher Scientific, Waltham, MA) for the core–shell particles.[25] Prior to the measurements the powder samples were outgassed under vacuum at $150\,^{\circ}\mathrm{C}$ for $12\,\mathrm{h}$ (SBA-15 and KIT-6 silicas) and at $250\,^{\circ}\mathrm{C}$ for $10\,\mathrm{h}$ (core–shell particles). Total pore volumes were obtained with the Gurvich rule at a relative pressure of $p/p_0 = 0.95$. Specific surface areas were determined by means of the Brunauer–Emmet–Teller equation in a range of $0.05 \leq p/p_0 \leq 0.3$.

A key point is that the lattice gas has a bulk coexistence curve that is symmetric about a fractional occupancy of 0.5 and that is why we chose this as the threshold value. As a practical matter, the vapor-like regions in the system have a much lower density than this while the liquid-like regions have a much higher value. This is illustrated by Figure 4.9. Each panel shows the frequency of lattice units with a given value of the fluid density as a function of the relative pressure p/p_0. Here, darker color corresponds to higher frequency. For each value of p/p_0, the frequency was normalized by its largest value at this pressure. For the three analyzed mesoporous samples, the majority of lattice units are characterized by fluid densities below 0.1 or above 0.9 over the whole range of $0 < p/p_0 \leq 1$. Thus, there exists a clear differentiation between lattice units that should be identified as filled with gas phase or liquid phase. Therefore, any choice of the threshold value close to the middle of the interval $[0.1,\ 0.9]$ does not affect noticeably the subsequent analysis. In our study, we used the value of 0.5.

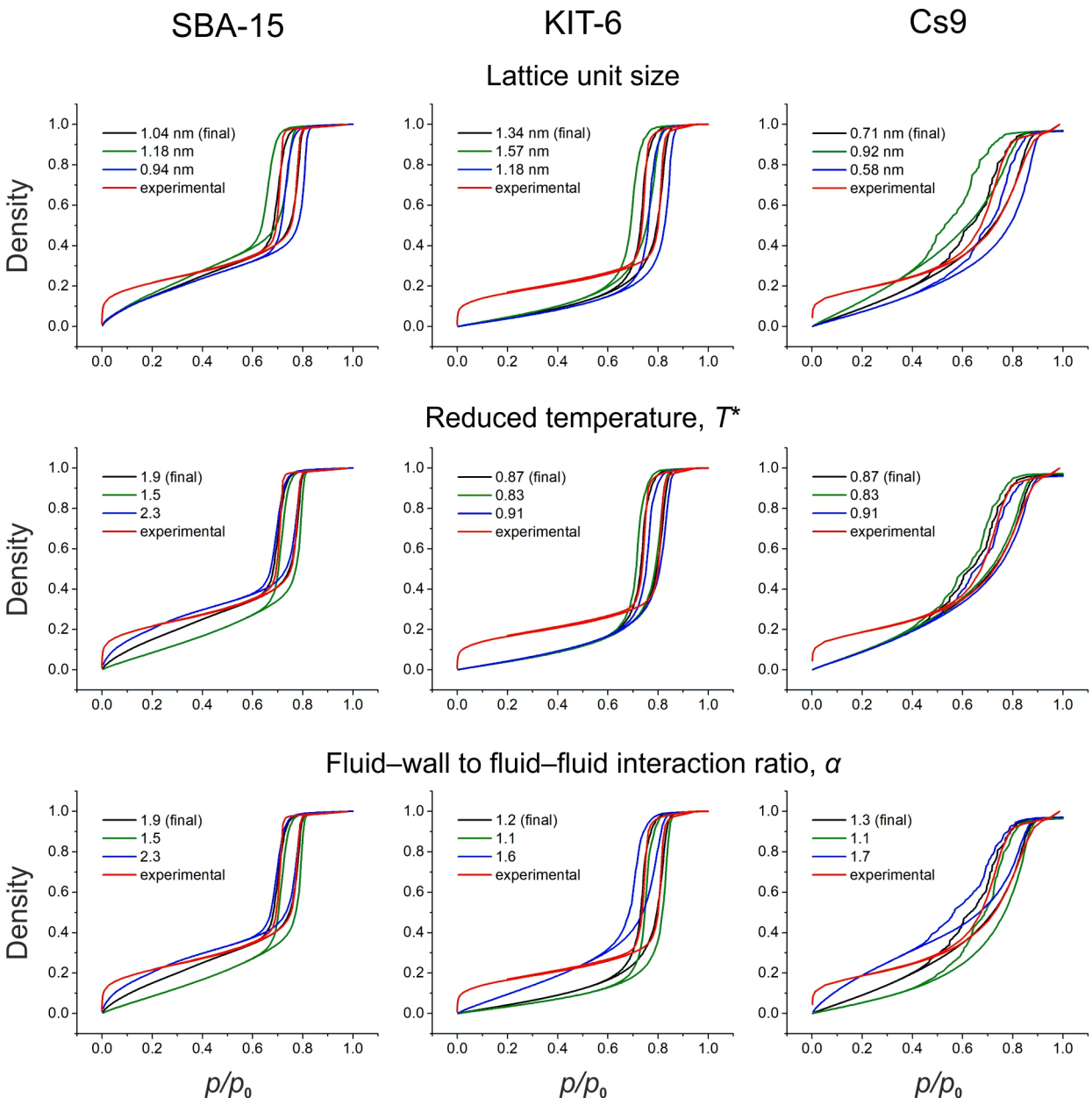

Figure 4.8: Impact of the variation of the three model parameters on the calculated isotherms. The calculated isotherms providing the best agreement with the experimental isotherms (red curves) in the hysteresis region are shown in black (final values).

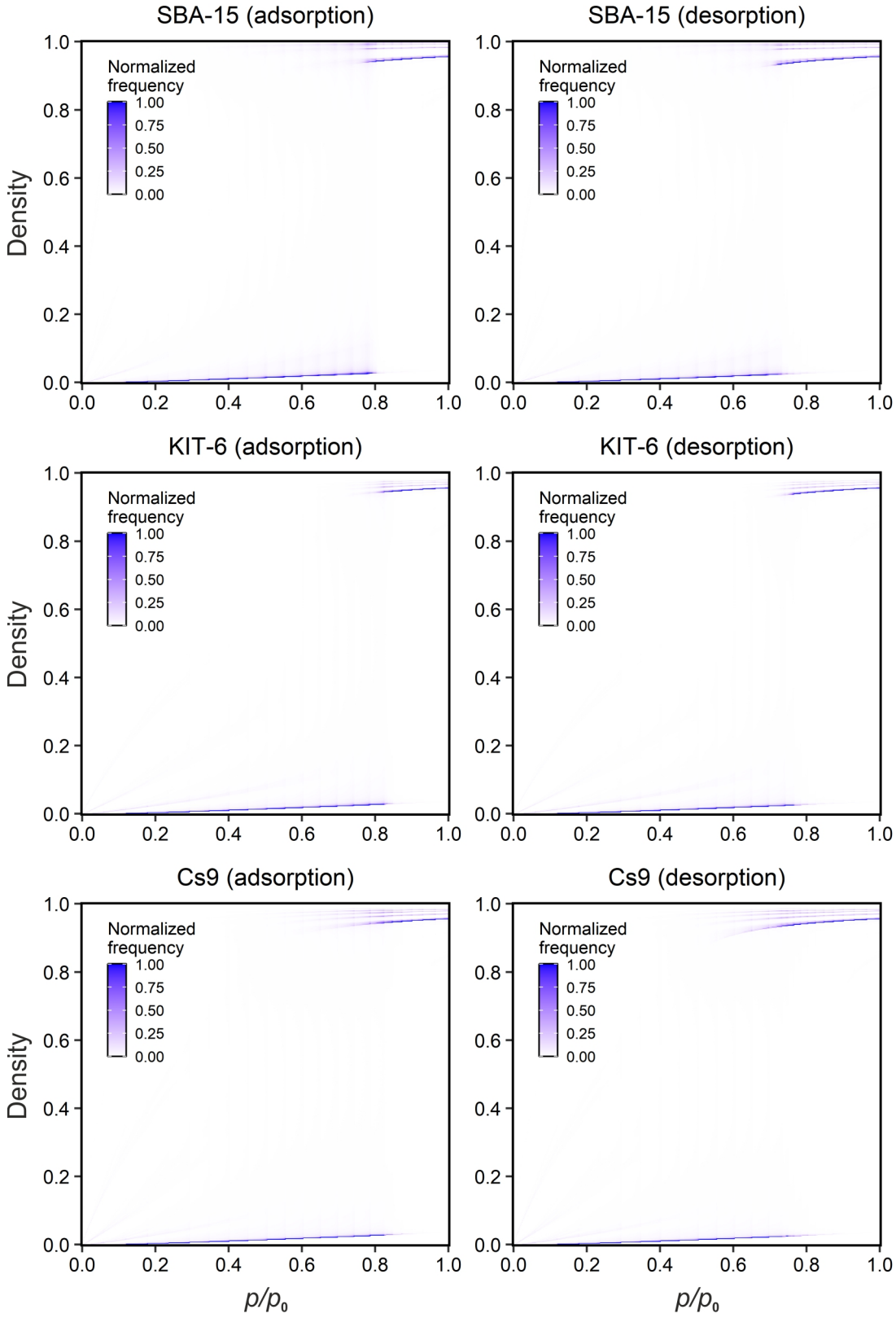

Figure 4.9: Normalized frequency of lattice units with a given fluid density as a function of the relative pressure p/p_0 for the three analyzed mesoporous samples during adsorption (left column) and desorption (right column). Normalization at each p/p_0-value was performed by dividing the frequency by its largest value at this pressure.

Bibliography

[1] L. J. Gibson and M. F. Ashby. *Cellular Solids: Structure and Properties*. Cambridge University Press, July 22, 1999. 536 pp. (see p. 1)

[2] P. S. Liu and K. M. Liang. "Review Functional materials of porous metals made by P/M, electroplating and some other techniques". *Journal of Materials Science* 36, 5059–5072, 2001. (see p. 1)

[3] F. Gritti, J. Hochstrasser, A. Svidrytski, D. Hlushkou, and U. Tallarek. "Morphology-transport relationships in liquid chromatography: Application to method development in size exclusion chromatography". *Journal of Chromatography A* 1620, 460991, 2020. (see p. 1)

[4] E. S. P. Bouvier. "Chromatography: Liquid | Monolithic Columns" in: *Encyclopedia of Separation Science* ed. by I. D. Wilson. Oxford: Academic Press, Jan. 1, 2007. 1–7 (see p. 1)

[5] D. Enke, R. Gläser, and U. Tallarek. "Sol-Gel and Porous Glass-Based Silica Monoliths with Hierarchical Pore Structure for Solid-Liquid Catalysis". *Chemie Ingenieur Technik* 88, 1561–1585, 2016. (see pp. 1, 2, 8, 31)

[6] K. Hormann, V. Baranau, D. Hlushkou, A. Höltzel, and U. Tallarek. "Topological analysis of non-granular, disordered porous media: determination of pore connectivity, pore coordination, and geometric tortuosity in physically reconstructed silica monoliths". *New Journal of Chemistry* 40, 4187–4199, 2016. (see pp. 2, 3, 34)

[7] S.-J. Reich, A. Svidrytski, A. Höltzel, J. Florek, F. Kleitz, W. Wang, C. Kübel, D. Hlushkou, and U. Tallarek. "Hindered Diffusion in Ordered Mesoporous Silicas: Insights from Pore-Scale Simulations in Physical Reconstructions of SBA-15 and KIT-6 Silica". *The Journal of Physical Chemistry C* 122, 12350–12361, 2018. (see pp. 2, 3, 7, 70, 75)

[8] R. Cimino, K. A. Cychosz, M. Thommes, and A. V. Neimark. "Experimental and theoretical studies of scanning adsorption–desorption isotherms". *Colloids and Surfaces A: Physicochemical and Engineering Aspects* 437, 76–89, 2013. (see pp. 2, 85)

[9] D. Schneider, D. Kondrashova, and R. Valiullin. "Phase transitions in disordered mesoporous solids". *Scientific Reports* 7, 7216, 2017. (see p. 2)

[10] H. R.N. B. Enninful, D. Schneider, R. Kohns, D. Enke, and R. Valiullin. "A novel approach for advanced thermoporometry characterization of mesoporous solids: Transition kernels and the serially connected pore model". *Microporous and Mesoporous Materials* 309, 110534, 2020. (see pp. 2, 10, 11)

[11] A. Svidrytski, D. Hlushkou, M. Thommes, P. A. Monson, and U. Tallarek. "Modeling the Impact of Mesoporous Silica Microstructures on the Adsorption Hysteresis Loop". *The Journal of Physical Chemistry C* 124, 21646–21655, 2020. (see pp. 2–4)

[12] G. Sdanghi, R. L. S. Canevesi, A. Celzard, M. Thommes, and V. Fierro. "Characterization of Carbon Materials for Hydrogen Storage and Compression". *Journal of Carbon Research* 6, 46, 2020. (see p. 2)

[13] R. Guillet-Nicolas, M. Wainer, L. Marcoux, M. Thommes, and F. Kleitz. "Exploring the confinement of polymer nanolayers into ordered mesoporous silica using advanced gas physisorption". *Journal of Colloid and Interface Science* 579, 489–507, 2020. (see p. 2)

[14] D. Stoeckel, C. Kübel, K. Hormann, A. Höltzel, B. M. Smarsly, and U. Tallarek. "Morphological Analysis of Disordered Macroporous–Mesoporous Solids Based on Physical Reconstruction by Nanoscale Tomography". *Langmuir* 30, 9022–9027, 2014. (see pp. 3, 32, 48, 56)

[15] S. Mitchell, A. B. Pinar, J. Kenvin, P. Crivelli, J. Kärger, and J. Pérez-Ramírez. "Structural analysis of hierarchically organized zeolites". *Nature Communications* 6, 8633, 2015. (see p. 3)

[16] J. Berthonneau, A. Obliger, P.-L. Valdenaire, O. Grauby, D. Ferry, D. Chaudanson, P. Levitz, J. J. Kim, F.-J. Ulm, and R. J.-M. Pellenq. "Mesoscale structure, mechanics, and transport properties of source rocks' organic pore networks". *Proceedings of the National Academy of Sciences* 115, 12365–12370, 2018. (see p. 3)

[17] Y. Yao, K. J. Czymmek, R. Pazhianur, and A. M. Lenhoff. "Three-Dimensional Pore Structure of Chromatographic Adsorbents from Electron Tomography". *Langmuir* 22, 11148–11157, 2006. (see p. 3)

[18] R. Leary, P. A. Midgley, and J. M. Thomas. "Recent Advances in the Application of Electron Tomography to Materials Chemistry". *Accounts of Chemical Research* 45, 1782–1791, 2012. (see pp. 3, 11, 56, 72)

[19] J. Zečević, K. P. DE Jong, and P. E. DE Jongh. "Progress in electron tomography to assess the 3D nanostructure of catalysts". *Current Opinion in Solid State and Materials Science* 17, 115–125, 2013. (see p. 3)

[20] S. Bruns, T. Hara, B. M. Smarsly, and U. Tallarek. "Morphological analysis of physically reconstructed capillary hybrid silica monoliths and correlation with separation efficiency". *Journal of Chromatography A* 1218, 5187–5194, 2011. (see pp. 3, 5, 16, 19)

[21] S. Bruns, D. Stoeckel, B. M. Smarsly, and U. Tallarek. "Influence of particle properties on the wall region in packed capillaries". *Journal of Chromatography A* 1268, 53–63, 2012. (see pp. 3, 5, 15, 16, 18, 19)

[22] D. Stoeckel, C. Kübel, M. O. Loeh, B. M. Smarsly, and U. Tallarek. "Morphological Analysis of Physically Reconstructed Silica Monoliths with Submicrometer Macropores: Effect of Decreasing Domain Size on Structural Homogeneity". *Langmuir* 31, 7391–7400, 2015. (see pp. 3, 5, 16, 19)

[23] W. Wang, A. Svidrytski, D. Wang, A. Villa, H. Hahn, U. Tallarek, and C. Kübel. "Quantifying Morphology and Diffusion Properties of Mesoporous Carbon From High-Fidelity 3D Reconstructions". *Microscopy and Microanalysis* 25, 891–902, 2019. (see p. 3)

[24] S.-J. Reich, A. Svidrytski, D. Hlushkou, D. Stoeckel, C. Kübel, A. Höltzel, and U. Tallarek. "Hindrance Factor Expression for Diffusion in Random Mesoporous Adsorbents Obtained from Pore-Scale Simulations in Physical Reconstructions". *Industrial & Engineering Chemistry Research* 57, 3031–3042, 2018. (see pp. 3, 7, 57, 58, 62)

[25] S.-J. Reich, A. Svidrytski, A. Höltzel, W. Wang, C. Kübel, D. Hlushkou, and U. Tallarek. "Transport under confinement: Hindrance factors for diffusion in core-shell and fully porous particles with different mesopore space morphologies". *Microporous and Mesoporous Materials* 282, 188–196, 2019. (see pp. 3, 7, 73, 75, 87, 89)

[26] J. Hochstrasser, A. Svidrytski, A. Höltzel, T. Priamushko, F. Kleitz, W. Wang, C. Kübel, and U. Tallarek. "Morphology–transport relationships for SBA-15 and KIT-6 ordered mesoporous silicas". *Physical Chemistry Chemical Physics* 22, 11314–11326, 2020. (see pp. 3, 7, 73, 75, 80, 83, 87, 89)

[27] A. E. Reising, J. M. Godinho, J. W. Jorgenson, and U. Tallarek. "Bed morphological features associated with an optimal slurry concentration for reproducible preparation of efficient capillary

ultrahigh pressure liquid chromatography columns". *Journal of Chromatography A* 1504, 71–82, 2017. (see pp. 3, 5, 15, 16, 18)

[28] T. Müllner, K. K. Unger, and U. Tallarek. "Characterization of microscopic disorder in reconstructed porous materials and assessment of mass transport-relevant structural descriptors". *New Journal of Chemistry* 40, 3993–4015, 2016. (see pp. 3, 5, 14–16, 20, 30, 32, 33, 39, 43, 57, 62)

[29] H. Liasneuski, D. Hlushkou, S. Khirevich, A. Höltzel, U. Tallarek, and S. Torquato. "Impact of microstructure on the effective diffusivity in random packings of hard spheres". *Journal of Applied Physics* 116, 034904, 2014. (see pp. 3, 35)

[30] S. Khirevich, A. Daneyko, A. Höltzel, A. Seidel-Morgenstern, and U. Tallarek. "Statistical analysis of packed beds, the origin of short-range disorder, and its impact on eddy dispersion". *Journal of Chromatography A* 1217, 4713–4722, 2010. (see pp. 3, 4, 6, 14, 17, 20)

[31] P. Levitz. "Toolbox for 3D imaging and modeling of porous media: Relationship with transport properties". *Cement and Concrete Research* 37, 351–359, 2007. (see pp. 3, 15, 30, 32)

[32] B. Coasne. "Multiscale adsorption and transport in hierarchical porous materials". *New Journal of Chemistry* 40, 4078–4094, 2016. (see pp. 3, 8, 10, 30, 56, 72)

[33] D. Hlushkou, A. Svidrytski, and U. Tallarek. "Tracer-Size-Dependent Pore Space Accessibility and Long-Time Diffusion Coefficient in Amorphous, Mesoporous Silica". *The Journal of Physical Chemistry C* 121, 8416–8426, 2017. (see pp. 4, 30, 34, 36, 41)

[34] A. Svidrytski, A. Rathi, D. Hlushkou, D. M. Ford, P. A. Monson, and U. Tallarek. "Morphology of Fluids Confined in Physically Reconstructed Mesoporous Silica: Experiment and Mean Field Density Functional Theory". *Langmuir* 34, 9936–9945, 2018. (see pp. 4, 72, 73, 76, 79, 80)

[35] F. Gritti and G. Guiochon. "Mass transfer kinetics, band broadening and column efficiency". *Journal of Chromatography A* 1221, 2–40, 2012. (see pp. 4, 14, 15)

[36] F. Gritti and G. Guiochon. "Perspectives on the Evolution of the Column Efficiency in Liquid Chromatography". *Analytical Chemistry* 85, 3017–3035, 2013. (see pp. 4, 14, 15)

[37] Torquato and Haslach. "Random Heterogeneous Materials: Microstructure and Macroscopic Properties". *Applied Mechanics Reviews* 55, B62–B63, 2002. (see pp. 4, 14)

[38] G. Guiochon, A. Felinger, and D. G. G. Shirazi. *Fundamentals of Preparative and Nonlinear Chromatography*. 2nd ed. Academic Press, 2006. (see pp. 4, 14)

[39] J. Kärger, D. M. Ruthven, and D. N. Theodorou. *Diffusion in Nanoporous Materials, 2 Volume Set*. John Wiley & Sons, 2012. 932 pp. (see pp. 4, 14)

[40] A. Okabe, B. Boots, K. Sugihara, and S. N. Chiu. "Spatial Tessellations: Concepts and Applications of Voronoi Diagrams" in: *Int. Encycl. Geogr. People, Earth, Environ. Technol.* Chichester, England: John Wiley & Sons Ltd., 2000. 1–11 (see pp. 4, 14)

[41] S. Khirevich, A. Höltzel, A. Seidel-Morgenstern, and U. Tallarek. "Geometrical and topological measures for hydrodynamic dispersion in confined sphere packings at low column-to-particle diameter ratios". *Journal of Chromatography A* 1262, 77–91, 2012. (see pp. 4, 14)

[42] N. N. Medvedev, V. P. Voloshin, V. A. Luchnikov, and M. L. Gavrilova. "An algorithm for three-dimensional Voronoi S-network". *Journal of Computational Chemistry* 27, 1676–1692, 2006. (see pp. 5, 15)

[43] K. Lochmann, L. Oger, and D. Stoyan. "Statistical analysis of random sphere packings with variable radius distribution". *Solid State Sciences* 8, 1397–1413, 2006. (see pp. 5, 15)

[44] M. Danisch, Y. Jin, and H. A. Makse. “Model of random packings of different size balls”. *Physical Review E* 81, 051303, 2010. (see pp. 5, 15)

[45] F. M. Schaller, S. C. Kapfer, M. E. Evans, M. J. F. Hoffmann, T. Aste, M. Saadatfar, K. Mecke, G. W. Delaney, and G. E. Schröder-Turk. “Set Voronoi diagrams of 3D assemblies of aspherical particles”. *Philosophical Magazine* 93, 3993–4017, 2013. (see pp. 5, 15)

[46] K. Hormann and U. Tallarek. “Analytical silica monoliths with submicron macropores: Current limitations to a direct morphology–column efficiency scaling”. *Journal of Chromatography A* 1312, 26–36, 2013. (see pp. 5, 16, 19)

[47] T. Müllner, A. Zankel, Y. Lv, F. Svec, A. Höltzel, and U. Tallarek. “Assessing Structural Correlations and Heterogeneity Length Scales in Functional Porous Polymers from Physical Reconstructions”. *Advanced Materials* 27, 6009–6013, 2015. (see pp. 5, 19)

[48] T. Müllner, A. Zankel, A. Höltzel, F. Svec, and U. Tallarek. “Morphological Properties of Methacrylate-Based Polymer Monoliths: From Gel Porosity to Macroscopic Inhomogeneities”. *Langmuir* 33, 2205–2214, 2017. (see pp. 5, 19)

[49] J. Kärger and D. M. Ruthven. “Diffusion in nanoporous materials: fundamental principles, insights and challenges”. *New Journal of Chemistry* 40, 4027–4048, 2016. (see pp. 6, 28)

[50] A. T. Florence. ““Targeting” nanoparticles: The constraints of physical laws and physical barriers”. *Journal of Controlled Release* 164, 115–124, 2012. (see pp. 6, 28)

[51] Y. S. Polyakov and A. L. Zydney. “Ultrafiltration membrane performance: Effects of pore blockage/constriction”. *Journal of Membrane Science* 434, 106–120, 2013. (see pp. 6, 28)

[52] H. Al-Obaidi and A. T. Florence. “Nanoparticle delivery and particle diffusion in confined and complex environments”. *Journal of Drug Delivery Science and Technology* 30, 266–277, 2015. (see pp. 6, 28)

[53] C. Sievers, Y. Noda, L. Qi, E. M. Albuquerque, R. M. Rioux, and S. L. Scott. “Phenomena Affecting Catalytic Reactions at Solid–Liquid Interfaces”. *ACS Catalysis* 6, 8286–8307, 2016. (see pp. 6, 28)

[54] J. M. Angelo and A. M. Lenhoff. “Determinants of protein elution rates from preparative ion-exchange adsorbents”. *Journal of Chromatography A* 1440, 94–104, 2016. (see pp. 6, 28)

[55] V. I. Syngouna and C. V. Chrysikopoulos. “Cotransport of clay colloids and viruses through water-saturated vertically oriented columns packed with glass beads: Gravity effects”. *Science of The Total Environment* 545-546, 210–218, 2016. (see pp. 6, 28)

[56] M. J. Skaug, L. Wang, Y. Ding, and D. K. Schwartz. “Hindered Nanoparticle Diffusion and Void Accessibility in a Three-Dimensional Porous Medium”. *ACS Nano* 9, 2148–2156, 2015. (see pp. 6, 7, 28, 30)

[57] F. Babayekhorasani, D. E. Dunstan, R. Krishnamoorti, and J. C. Conrad. “Nanoparticle diffusion in crowded and confined media”. *Soft Matter* 12, 8407–8416, 2016. (see pp. 6, 7, 28, 30)

[58] P. Dechadilok and W. M. Deen. “Hindrance Factors for Diffusion and Convection in Pores”. *Industrial & Engineering Chemistry Research* 45, 6953–6959, 2006. (see pp. 6, 7, 28, 29)

[59] R. H. Li, D. H. Altreuter, and F. T. Gentile. “Transport characterization of hydrogel matrices for cell encapsulation”. *Biotechnology and Bioengineering* 50, 365–373, 1996. (see p. 7)

[60] E. M. Renkin. “Filtration, diffusion, and molecular sieving through porous cellulose membranes”. *The Journal of General Physiology* 38, 225–243, 1954. (see p. 7)

[61] P. M. Bungay and H. Brenner. “The motion of a closely-fitting sphere in a fluid-filled tube”. *International Journal of Multiphase Flow* 1, 25–56, 1973. (see pp. 7, 29)

[62] W. M. Deen. “Hindered transport of large molecules in liquid-filled pores”. *AIChE Journal* 33, 1409–1425, 1987. (see pp. 7, 29, 42)

[63] V. Wernert, R. Bouchet, and R. Denoyel. “Influence of Molecule Size on Its Transport Properties through a Porous Medium”. *Analytical Chemistry* 82, 2668–2679, 2010. (see pp. 7, 29, 42, 43, 46)

[64] J. Kärger and R. Valiullin. “Mass transfer in mesoporous materials: the benefit of microscopic diffusion measurement”. *Chemical Society Reviews* 42, 4172–4197, 2013. (see pp. 7, 30)

[65] T. Titze, A. Lauerer, L. Heinke, C. Chmelik, N. E. R. Zimmermann, F. J. Keil, D. M. Ruthven, and J. Kärger. “Transport in Nanoporous Materials Including MOFs: The Applicability of Fick’s Laws”. *Angewandte Chemie International Edition* 54, 14580–14583, 2015. (see pp. 7, 30)

[66] A. Galarneau, F. Guenneau, A. Gedeon, D. Mereib, J. Rodriguez, F. Fajula, and B. Coasne. “Probing Interconnectivity in Hierarchical Microporous/Mesoporous Materials Using Adsorption and Nuclear Magnetic Resonance Diffusion”. *The Journal of Physical Chemistry C* 120, 1562–1569, 2016. (see pp. 7, 30)

[67] F. Elwinger, P. Pourmand, and I. Furó. “Diffusive Transport in Pores. Tortuosity and Molecular Interaction with the Pore Wall”. *The Journal of Physical Chemistry C* 121, 13757–13764, 2017. (see pp. 7, 30, 40, 45)

[68] J. Kärger, C. Chmelik, L. Heinke, and R. Valiullin. “A new view of diffusion in nanoporous materials”. *Chemie Ingenieur Technik* 82, 779–804, 2010. (see pp. 7, 30)

[69] J. Kärger, T. Binder, C. Chmelik, F. Hibbe, H. Krautscheid, R. Krishna, and J. Weitkamp. “Microimaging of transient guest profiles to monitor mass transfer in nanoporous materials”. *Nature Materials* 13, 333–343, 2014. (see pp. 7, 30)

[70] M. J. Skaug and D. K. Schwartz. “Tracking Nanoparticle Diffusion in Porous Filtration Media”. *Industrial & Engineering Chemistry Research* 54, 4414–4419, 2015. (see pp. 7, 30)

[71] K. K. Unger, R. Skudas, and M. M. Schulte. “Particle packed columns and monolithic columns in high-performance liquid chromatography-comparison and critical appraisal”. *Journal of Chromatography A* 1184, 393–415, 2008. (see pp. 8, 16, 31, 56)

[72] A. Galarneau, A. Sachse, B. Said, C.-H. Pelisson, P. Boscaro, N. Brun, L. Courtheoux, N. Olivi-Tran, B. Coasne, and F. Fajula. “Hierarchical porous silica monoliths: A novel class of microreactors for process intensification in catalysis and adsorption”. *Comptes Rendus Chimie* 19, 231–247, 2016. (see pp. 8, 16, 31, 56)

[73] E. Aznar, M. Oroval, L. Pascual, J. R. Murguía, R. Martínez-Máñez, and F. Sancenón. “Gated Materials for On-Command Release of Guest Molecules”. *Chemical Reviews* 116, 561–718, 2016. (see pp. 8, 31)

[74] F. Gritti and G. Guiochon. “The current revolution in column technology: How it began, where is it going?” *Journal of Chromatography A* 1228, 2–19, 2012. (see p. 8)

[75] J. Zhang and C. Ming Li. “Nanoporous metals: fabrication strategies and advanced electrochemical applications in catalysis, sensing and energy systems”. *Chemical Society Reviews* 41, 7016–7031, 2012. (see p. 8)

[76] D. I. Fried, F. J. Brieler, and M. Fröba. “Designing Inorganic Porous Materials for Enzyme Adsorption and Applications in Biocatalysis”. *ChemCatChem* 5, 862–884, 2013. (see p. 8)

[77] S. Lwin and I. E. Wachs. “Olefin Metathesis by Supported Metal Oxide Catalysts”. *ACS Catalysis* 4, 2505–2520, 2014. (see p. 8)

[78] L. Vilcocq, P. C. Castilho, F. Carvalheiro, and L. C. Duarte. “Hydrolysis of Oligosaccharides Over Solid Acid Catalysts: A Review”. *ChemSusChem* 7, 1010–1019, 2014. (see p. 8)

[79] R. Munirathinam, J. Huskens, and W. Verboom. “Supported Catalysis in Continuous-Flow Microreactors”. *Advanced Synthesis & Catalysis* 357, 1093–1123, 2015. (see p. 8)

[80] D. J. Wales, J. Grand, V. P. Ting, R. D. Burke, K. J. Edler, C. R. Bowen, S. Mintova, and A. D. Burrows. “Gas sensing using porous materials for automotive applications”. *Chemical Society Reviews* 44, 4290–4321, 2015. (see p. 8)

[81] W. J. Roth, B. Gil, W. Makowski, B. Marszalek, and P. Eliášová. “Layer like porous materials with hierarchical structure”. *Chemical Society Reviews* 45, 3400–3438, 2016. (see p. 8)

[82] R. Millini and G. Bellussi. “Hybrid organic–inorganic zeolites: status and perspectives”. *Catalysis Science & Technology* 6, 2502–2527, 2016. (see p. 8)

[83] K. Ganesan, A. Dennstedt, A. Barowski, and L. Ratke. “Design of aerogels, cryogels and xerogels of cellulose with hierarchical porous structures”. *Materials & Design* 92, 345–355, 2016. (see p. 8)

[84] M. Hartmann and W. Schwieger. “Hierarchically-structured porous materials: from basic understanding to applications”. *Chemical Society Reviews* 45, 3311–3312, 2016. (see p. 8)

[85] K. Zhang and M. L. Ostraat. “Innovations in hierarchical zeolite synthesis”. *Catalysis Today* 264, 3–15, 2016. (see p. 8)

[86] L. Xu and P. Wu. “Diversity of layered zeolites: from synthesis to structural modifications”. *New Journal of Chemistry* 40, 3968–3981, 2016. (see p. 8)

[87] J. Florek, R. Caillard, and F. Kleitz. “Evaluation of mesoporous silica nanoparticles for oral drug delivery – current status and perspective of MSNs drug carriers”. *Nanoscale* 9, 15252–15277, 2017. (see p. 8)

[88] D. M. Schlipf, S. Zhou, M. A. Khan, S. E. Rankin, and B. L. Knutson. “Effects of Pore Size and Tethering on the Diffusivity of Lipids Confined in Mesoporous Silica”. *Advanced Materials Interfaces* 4, 1601103, 2017. (see p. 8)

[89] R. Diab, N. Canilho, I. A. Pavel, F. B. Haffner, M. Girardon, and A. Pasc. “Silica-based systems for oral delivery of drugs, macromolecules and cells”. *Advances in Colloid and Interface Science* 249, 346–362, 2017. (see p. 8)

[90] H. Singh and R. S. Myong. “Critical Review of Fluid Flow Physics at Micro- to Nano-scale Porous Media Applications in the Energy Sector”. *Advances in Material Science and Engineering*, 9565240, 2018. (see p. 8)

[91] J. Rouquerol, D. Avnir, C. W. Fairbridge, D. H. Everett, J. M. Haynes, N. Pernicone, J. D. F. Ramsay, K. S. W. Sing, and K. K. Unger. “Recommendations for the characterization of porous solids (Technical Report)”. *Pure and Applied Chemistry* 66, 1739–1758, 1994. (see p. 8)

[92] M. Thommes, K. Kaneko, A. V. Neimark, J. P. Olivier, F. Rodriguez-Reinoso, J. Rouquerol, and K. S. W. Sing. “Physisorption of gases, with special reference to the evaluation of surface area and pore size distribution (IUPAC Technical Report)”. *Pure and Applied Chemistry* 87, 1051–1069, 2015. (see pp. 9, 79, 85)

[93] K. A. Cychosz, R. Guillet-Nicolas, J. García-Martínez, and M. Thommes. “Recent advances in the textural characterization of hierarchically structured nanoporous materials”. *Chemical Society Reviews* 46, 389–414, 2017. (see pp. 9, 10, 49, 56–58, 61, 65, 85)

[94] J. Rouquerol, F. Rouquerol, P. Llewellyn, G. Maurin, and K. S. W. Sing. *Adsorption by Powders and Porous Solids: Principles, Methodology and Applications*. Academic Press, Sept. 6, 2013. 647 pp. (see p. 9)

[95] S. J. Gregg, K. S. W. Sing, and H. W. Salzberg. “Adsorption Surface Area and Porosity”. *Journal of The Electrochemical Society* 114, 279C, 1967. (see p. 9)

[96] T. Horikawa, D. D. Do, and D. Nicholson. “Capillary condensation of adsorbates in porous materials”. *Advances in Colloid and Interface Science* 169, 40–58, 2011. (see p. 9)

[97] B. Coasne, A. Galarneau, R. J. M. Pellenq, and F. D. Renzo. “Adsorption, intrusion and freezing in porous silica : the view from the nanoscale”. *Chemical Society Reviews* 42, 4141–4171, 2013. (see p. 9)

[98] K. Morishige. “Effects of Carbon Coating and Pore Corrugation on Capillary Condensation of Nitrogen in SBA-15 Mesoporous Silica”. *Langmuir* 29, 11915–11923, 2013. (see pp. 9, 72)

[99] J. Li, Y. Liu, G. Jiang, and X. Zhang. “Vapour-to-liquid nucleation in cone pores”. *Molecular Simulation* 42, 1–8, 2016. (see p. 9)

[100] A. G. Foster. “The sorption of condensible vapours by porous solids. Part I. The applicability of the capillary theory”. *Transactions of the Faraday Society* 28, 645, 1932. (see p. 9)

[101] B. Coasne, K. E. Gubbins, and R. J.-M. Pellenq. “Domain theory for capillary condensation hysteresis”. *Physical Review B* 72, 024304, 2005. (see pp. 9, 72)

[102] K. Morishige. “Dependent Domain Model of Cylindrical Pores”. *The Journal of Physical Chemistry C* 121, 5099–5107, 2017. (see pp. 9, 72)

[103] N. Klomkliang, D. D. Do, and D. Nicholson. “Effects of temperature, pore dimensions and adsorbate on the transition from pore blocking to cavitation in an ink-bottle pore”. *Chemical Engineering Journal* 239, 274–283, 2014. (see p. 9)

[104] J. Landers, G. Y. Gor, and A. V. Neimark. “Density functional theory methods for characterization of porous materials”. *Colloids and Surfaces A: Physicochemical and Engineering Aspects* 437, 3–32, 2013. (see pp. 9, 10, 56, 72)

[105] P. A. Monson. “Contact Angles, Pore Condensation, and Hysteresis: Insights from a Simple Molecular Model”. *Langmuir* 24, 12295–12302, 2008. (see p. 9)

[106] K. Morishige and N. Tarui. “Capillary Condensation of Nitrogen in Ordered Mesoporous Silica with Bicontinuous Gyroid Structure”. *The Journal of Physical Chemistry C* 111, 280–285, 2007. (see pp. 10, 72)

[107] H.-J. Woo, L. Sarkisov, and P. A. Monson. “Mean-Field Theory of Fluid Adsorption in a Porous Glass”. *Langmuir* 17, 7472–7475, 2001. (see pp. 10, 72)

[108] L. Sarkisov and P. A. Monson. “Modeling of Adsorption and Desorption in Pores of Simple Geometry Using Molecular Dynamics”. *Langmuir* 17, 7600–7604, 2001. (see p. 10)

[109] P. I. Ravikovitch and A. V. Neimark. “Density Functional Theory of Adsorption in Spherical Cavities and Pore Size Characterization of Templated Nanoporous Silicas with Cubic and Three-Dimensional Hexagonal Structures”. *Langmuir* 18, 1550–1560, 2002. (see p. 10)

[110] P. I. Ravikovitch and A. V. Neimark. “Experimental Confirmation of Different Mechanisms of Evaporation from Ink-Bottle Type Pores: Equilibrium, Pore Blocking, and Cavitation”. *Langmuir* 18, 9830–9837, 2002. (see pp. 10, 67, 70)

[111] A. Vishnyakov and A. V. Neimark. “Monte Carlo Simulation Test of Pore Blocking Effects”. *Langmuir* 19, 3240–3247, 2003. (see p. 10)

[112] B. Libby and P. A. Monson. “Adsorption/Desorption Hysteresis in Inkbottle Pores: A Density Functional Theory and Monte Carlo Simulation Study”. *Langmuir* 20, 4289–4294, 2004. (see p. 10)

[113] M. Thommes, B. Smarsly, M. Groenewolt, P. I. Ravikovitch, and A. V. Neimark. “Adsorption Hysteresis of Nitrogen and Argon in Pore Networks and Characterization of Novel Micro- and Mesoporous Silicas”. *Langmuir* 22, 756–764, 2006. (see pp. 10, 83, 84)

[114] K. Morishige, M. Tateishi, F. Hirose, and K. Aramaki. “Change in Desorption Mechanism from Pore Blocking to Cavitation with Temperature for Nitrogen in Ordered Silica with Cagelike Pores”. *Langmuir* 22, 9220–9224, 2006. (see p. 10)

[115] R. Evans. “Fluids adsorbed in narrow pores: phase equilibria and structure”. *Journal of Physics: Condensed Matter* 2, 8989–9007, 1990. (see pp. 10, 56, 72)

[116] L. D. Gelb, K. E. Gubbins, R. Radhakrishnan, and M. Sliwinska-Bartkowiak. “Phase separation in confined systems”. *Reports on Progress in Physics* 62, 1573–1659, 1999. (see pp. 10, 56, 72)

[117] A. V. Neimark, P. I. Ravikovitch, and A. Vishnyakov. “Bridging scales from molecular simulations to classical thermodynamics: density functional theory of capillary condensation in nanopores”. *Journal of Physics: Condensed Matter* 15, 347–365, 2003. (see pp. 10, 56, 72)

[118] P. A. Monson. “Understanding adsorption/desorption hysteresis for fluids in mesoporous materials using simple molecular models and classical density functional theory”. *Microporous and Mesoporous Materials* 160, 47–66, 2012. (see pp. 10, 11, 56, 57, 59, 72, 76)

[119] J. D. Evans, G. Fraux, R. Gaillac, D. Kohen, F. Trousselet, J.-M. Vanson, and F.-X. Coudert. “Computational Chemistry Methods for Nanoporous Materials”. *Chemistry of Materials* 29, 199–212, 2017. (see pp. 10, 56, 72)

[120] W. P. Krekelberg, D. W. Siderius, V. K. Shen, T. M. Truskett, and J. R. Errington. “Connection Between Thermodynamics and Dynamics of Simple Fluids in Pores: Impact of Fluid–Fluid Interaction Range and Fluid–Solid Interaction Strength”. *The Journal of Physical Chemistry C* 121, 16316–16327, 2017. (see pp. 10, 56, 72)

[121] M. Thommes, R. Skudas, K. K. Unger, and D. Lubda. “Textural characterization of native and n-alky-bonded silica monoliths by mercury intrusion/extrusion, inverse size exclusion chromatography and nitrogen adsorption”. *Journal of Chromatography A* 1191, 57–66, 2008. (see pp. 10, 57)

[122] S. Naumov, A. Khokhlov, R. Valiullin, J. Kärger, and P. A. Monson. “Understanding capillary condensation and hysteresis in porous silicon: Network effects within independent pores”. *Physical Review E* 78, 060601, 2008. (see p. 11)

[123] Z. Liu, N. Fujita, K. Miyasaka, L. Han, S. M. Stevens, M. Suga, S. Asahina, B. Slater, C. Xiao, Y. Sakamoto, M. W. Anderson, R. Ryoo, and O. Terasaki. “A review of fine structures of nanoporous materials as evidenced by microscopic methods”. *Microscopy* 62, 109–146, 2013. (see pp. 11, 56, 72)

[124] D. S. Su, B. Zhang, and R. Schlögl. “Electron Microscopy of Solid Catalysts—Transforming from a Challenge to a Toolbox”. *Chemical Reviews* 115, 2818–2882, 2015. (see pp. 11, 56, 72)

[125] M. R. Schure and R. S. Maier. “How does column packing microstructure affect column efficiency in liquid chromatography?” *Journal of Chromatography A* 1126, 58–69, 2006. (see p. 14)

[126] M. F. Wahab, D. C. Patel, R. M. Wimalasinghe, and D. W. Armstrong. “Fundamental and Practical Insights on the Packing of Modern High-Efficiency Analytical and Capillary Columns”. *Analytical Chemistry* 89, 8177–8191, 2017. (see p. 14)

[127] L. E. Blue, E. G. Franklin, J. M. Godinho, J. P. Grinias, K. M. Grinias, D. B. Lunn, and S. M. Moore. “Recent advances in capillary ultrahigh pressure liquid chromatography”. *Journal of Chromatography A* 1523, 17–39, 2017. (see p. 14)

[128] J. Giddings. *Dynamics of Chromatography. Part. 1: Principles and Theory*. New York, NY: Marcel Dekker, 1965. (see p. 15)

[129] S. Khirevich, A. Höltzel, A. Seidel-Morgenstern, and U. Tallarek. “Time and Length Scales of Eddy Dispersion in Chromatographic Beds”. *Analytical Chemistry* 81, 7057–7066, 2009. (see pp. 15, 20)

[130] P. Levitz and D. Tchoubar. “Disordered porous solids : from chord distributions to small angle scattering”. *Journal de Physique I* 2, 771–790, 1992. (see pp. 15, 18, 37)

[131] S. Torquato and B. Lu. “Chord-length distribution function for two-phase random media”. *Physical Review E* 47, 2950–2953, 1993. (see pp. 15, 18)

[132] S. Torquato. “Statistical Description of Microstructures”. *Annual Review of Materials Research* 32, 77–111, 2002. (see p. 15)

[133] A. E. Reising, S. Schlabach, V. Baranau, D. Stoeckel, and U. Tallarek. “Analysis of packing microstructure and wall effects in a narrow-bore ultrahigh pressure liquid chromatography column using focused ion-beam scanning electron microscopy”. *Journal of Chromatography A* 1513, 172–182, 2017. (see pp. 16, 18)

[134] S. Khirevich, A. Höltzel, and U. Tallarek. “Validation of Pore-Scale Simulations of Hydrodynamic Dispersion in Random Sphere Packings”. *Communications in Computational Physics* 13, 801–822, 2013. (see pp. 17, 20)

[135] W. S. Jodrey and E. M. Tory. “Computer simulation of close random packing of equal spheres”. *Physical Review A* 32, 2347–2351, 1985. (see p. 17)

[136] A. Bezrukov, M. Bargieł, and D. Stoyan. “Statistical Analysis of Simulated Random Packings of Spheres”. *Particle & Particle Systems Characterization* 19, 111–118, 2002. (see p. 17)

[137] D. Hlushkou and U. Tallarek. “Analysis of microstructure–effective diffusivity relationships for the interparticle pore space in physically reconstructed packed beds”. *Journal of Chromatography A* 1581-1582, 173–179, 2018. (see pp. 18, 22)

[138] R. S. Maier, D. M. Kroll, R. S. Bernard, S. E. Howington, J. F. Peters, and H. T. Davis. “Pore-scale simulation of dispersion”. *Physics of Fluids* 12, 2065–2079, 2000. (see p. 20)

[139] M. R. Schure, R. S. Maier, D. M. Kroll, and H. T. Davis. “Simulation of Packed-Bed Chromatography Utilizing High-Resolution Flow Fields: Comparison with Models”. *Analytical Chemistry* 74, 6006–6016, 2002. (see p. 20)

[140] S. Khirevich, A. Höltzel, D. Hlushkou, and U. Tallarek. “Impact of Conduit Geometry and Bed Porosity on Flow and Dispersion in Noncylindrical Sphere Packings”. *Analytical Chemistry* 79, 9340–9349, 2007. (see p. 20)

[141] A. Daneyko, A. Höltzel, S. Khirevich, and U. Tallarek. “Influence of the Particle Size Distribution on Hydraulic Permeability and Eddy Dispersion in Bulk Packings”. *Analytical Chemistry* 83, 3903–3910, 2011. (see pp. 20, 22)

[142] D. Hlushkou, F. Gritti, A. Daneyko, G. Guiochon, and U. Tallarek. “How Microscopic Characteristics of the Adsorption Kinetics Impact Macroscale Transport in Chromatographic Beds”. *The Journal of Physical Chemistry C* 117, 22974–22985, 2013. (see p. 20)

[143] A. Daneyko, D. Hlushkou, V. Baranau, S. Khirevich, A. Seidel-Morgenstern, and U. Tallarek. “Computational investigation of longitudinal diffusion, eddy dispersion, and trans-particle mass transfer in bulk, random packings of core–shell particles with varied shell thickness and shell diffusion coefficient”. *Journal of Chromatography A* 1407, 139–156, 2015. (see pp. 20, 35, 47)

[144] H. Koku, R. S. Maier, M. R. Schure, and A. M. Lenhoff. “Modeling of dispersion in a polymeric chromatographic monolith”. *Journal of Chromatography A* 1237, 55–63, 2012. (see pp. 20, 35)

[145] D. Hlushkou, K. Hormann, A. Höltzel, S. Khirevich, A. Seidel-Morgenstern, and U. Tallarek. “Comparison of first and second generation analytical silica monoliths by pore-scale simulations of eddy dispersion in the bulk region”. *Journal of Chromatography A* 1303, 28–38, 2013. (see p. 20)

[146] D. L. Koch and J. F. Brady. “Dispersion in fixed beds”. *Journal of Fluid Mechanics* 154, 399–427, 1985. (see p. 22)

[147] M. Sahimi. *Flow and Transport in Porous Media and Fractured Rock: From Classical Methods to Modern Approaches*. 2n ed. Weinheim: Wiley-VCH, 2011. (see p. 22)

[148] J. J. L. Higdon and G. P. Muldowney. “Resistance functions for spherical particles, droplets and bubbles in cylindrical tubes”. *Journal of Fluid Mechanics* 298, 193–210, 1995. (see p. 29)

[149] G. M. Mavrovouniotis and H. Brenner. “Hindered sedimentation, diffusion, and dispersion coefficients for brownian spheres in circular cylindrical pores”. *Journal of Colloid and Interface Science* 124, 269–283, 1988. (see p. 29)

[150] J. F. Langford, M. R. Schure, Y. Yao, S. F. Maloney, and A. M. Lenhoff. “Effects of pore structure and molecular size on diffusion in chromatographic adsorbents”. *Journal of Chromatography A* 1126, 95–106, 2006. (see p. 30)

[151] D. Müter, H. O. Sørensen, H. Bock, and S. L. S. Stipp. “Particle Diffusion in Complex Nanoscale Pore Networks”. *The Journal of Physical Chemistry C* 119, 10329–10335, 2015. (see p. 30)

[152] S. Altmaier and K. Cabrera. “Structure and performance of silica-based monolithic HPLC columns”. *Journal of Separation Science* 31, 2551–2559, 2008. (see pp. 31, 58)

[153] K. Hormann and U. Tallarek. “Mass transport properties of second-generation silica monoliths with mean mesopore size from 5 to 25 nm”. *Journal of Chromatography A* 1365, 94–105, 2014. (see p. 31)

[154] P. A. Midgley and M. Weyland. “3D electron microscopy in the physical sciences: the development of Z-contrast and EFTEM tomography”. *Ultramicroscopy* 96, 413–431, 2003. (see p. 31)

[155] C. Kübel, A. Voigt, R. Schoenmakers, M. Otten, D. Su, T.-C. Lee, A. Carlsson, and J. Bradley. “Recent Advances in Electron Tomography: TEM and HAADF-STEM Tomography for Materials

Science and Semiconductor Applications". *Microscopy and Microanalysis* 11, 378–400, 2005. (see p. 31)

[156] J. R. Kremer, D. N. Mastronarde, and J. R. McIntosh. "Computer Visualization of Three-Dimensional Image Data Using IMOD". *Journal of Structural Biology* 116, 71–76, 1996. (see p. 32)

[157] P. Gilbert. "Iterative methods for the three-dimensional reconstruction of an object from projections". *Journal of Theoretical Biology* 36, 105–117, 1972. (see p. 32)

[158] F. Delay, P. Ackerer, and C. Danquigny. "Simulating Solute Transport in Porous or Fractured Formations Using Random Walk Particle Tracking: A Review". *Vadose Zone Journal* 4, 360–379, 2005. (see p. 34)

[159] J. Salles, J. Thovert, R. Delannay, L. Prevors, J. Auriault, and P. M. Adler. "Taylor dispersion in porous media. Determination of the dispersion tensor". *Physics of Fluids A: Fluid Dynamics* 5, 2348–2376, 1993. (see p. 34)

[160] L. M. Schwartz, E. J. Garboczi, and D. P. Bentz. "Interfacial transport in porous media: Application to dc electrical conductivity of mortars". *Journal of Applied Physics* 78, 5898–5908, 1995. (see p. 35)

[161] L. M. Schwartz and J. R. Banavar. "Transport properties of disordered continuum systems". *Physical Review B* 39, 11965–11970, 1989. (see p. 35)

[162] M. E. Kainourgiakis, E. S. Kikkinides, A. Galani, G. C. Charalambopoulou, and A. K. Stubos. "Digitally Reconstructed Porous Media: Transport and Sorption Properties". *Transport in Porous Media* 58, 43–62, 2005. (see p. 35)

[163] M. H. Blees and J. C. Leyte. "The Effective Translational Self-Diffusion Coefficient of Small Molecules in Colloidal Crystals of Spherical Particles". *Journal of Colloid and Interface Science* 166, 118–127, 1994. (see p. 35)

[164] S. Torquato. "Trapping of finite-sized Brownian particles in porous media". *The Journal of Chemical Physics* 95, 2838–2841, 1991. (see p. 35)

[165] I. C. Kim and S. Torquato. "Diffusion of finite-sized Brownian particles in porous media". *The Journal of Chemical Physics* 96, 1498–1503, 1992. (see p. 35)

[166] T. Müllner, A. Zankel, F. Svec, and U. Tallarek. "Finite-size effects in the 3D reconstruction and morphological analysis of porous polymers". *Materials Today* 17, 404–411, 2014. (see p. 36)

[167] W. Gille, D. Enke, and F. Janowski. "Stereological Macropore Analysis of a Controlled Pore Glass by use of Small-Angle Scattering". *Journal of Porous Materials* 8, 179–191, 2001. (see p. 37)

[168] G. Gaiselmann, M. Neumann, V. Schmidt, O. Pecho, T. Hocker, and L. Holzer. "Quantitative relationships between microstructure and effective transport properties based on virtual materials testing". *AIChE Journal* 60, 1983–1999, 2014. (see p. 40)

[169] D. Wiedenmann, L. Keller, L. Holzer, J. Stojadinović, B. Münch, L. Suarez, B. Fumey, H. Hagendorfer, R. Brönnimann, P. Modregger, M. Gorbar, U. F. Vogt, A. Züttel, F. L. Mantia, R. Wepf, and B. Grobéty. "Three-dimensional pore structure and ion conductivity of porous ceramic diaphragms". *AIChE Journal* 59, 1446–1457, 2013. (see p. 40)

[170] P. Levitz, G. Ehret, S. K. Sinha, and J. M. Drake. "Porous vycor glass: The microstructure as probed by electron microscopy, direct energy transfer, small-angle scattering, and molecular adsorption". *J. Chem. Phys.* 95, 6151–6161, 1991. (see p. 40)

[171] H. L. Weissberg. “Effective Diffusion Coefficient in Porous Media”. *Journal of Applied Physics* 34, 2636–2639, 1963. (see p. 44)

[172] P. Y. Lanfrey, Z. V. Kuzeljevic, and M. P. Dudukovic. “Tortuosity model for fixed beds randomly packed with identical particles”. *Chemical Engineering Science* 65, 1891–1896, 2010. (see p. 44)

[173] M. Barrande, R. Bouchet, and R. Denoyel. “Tortuosity of Porous Particles”. *Analytical Chemistry* 79, 9115–9121, 2007. (see p. 44)

[174] S. Khirevich, A. Höltzel, A. Daneyko, A. Seidel-Morgenstern, and U. Tallarek. “Structure–transport correlation for the diffusive tortuosity of bulk, monodisperse, random sphere packings”. *Journal of Chromatography A* 1218, 6489–6497, 2011. (see p. 44)

[175] M. T. Bishop, K. H. Langley, and F. E. Karasz. “Dynamic light-scattering studies of polymer diffusion in porous materials: linear polystyrene in porous glass”. *Macromolecules* 22, 1220–1231, 1989. (see p. 45)

[176] S. G.J. M. Kluijtmans, J. K. G. Dhont, and A. P. Philipse. “Dynamics of Uncharged Colloidal Silica Spheres Confined in Bicontinuous Porous Glass Media”. *Langmuir* 13, 4982–4987, 1997. (see pp. 45, 47)

[177] Y. Guo, K. H. Langley, and F. E. Karasz. “Nonanomalous diffusion in Vycor porous glass”. *Physical Review B* 50, 3400–3403, 1994. (see pp. 45, 47)

[178] M. E. Kainourgiakis, E. S. Kikkinides, A. K. Stubos, and N. K. Kanellopoulos. “Simulation of self-diffusion of point-like and finite-size tracers in stochastically reconstructed Vycor porous glasses”. *The Journal of Chemical Physics* 111, 2735–2743, 1999. (see p. 45)

[179] S. G.J. M. Kluijtmans and A. P. Philipse. “First in Situ Determination of Confined Brownian Tracer Motion in Dense Random Sphere Packings”. *Langmuir* 15, 1896–1898, 1999. (see p. 45)

[180] D. Hlushkou, F. Gritti, G. Guiochon, A. Seidel-Morgenstern, and U. Tallarek. “Effect of Adsorption on Solute Dispersion: A Microscopic Stochastic Approach”. *Analytical Chemistry* 86, 4463–4470, 2014. (see p. 47)

[181] P. Ercius, O. Alaidi, M. J. Rames, and G. Ren. “Electron Tomography: A Three-Dimensional Analytic Tool for Hard and Soft Materials Research”. *Advanced Materials* 27, 5638–5663, 2015. (see pp. 56, 72)

[182] K. Nakanishi and N. Tanaka. “Sol–Gel with Phase Separation. Hierarchically Porous Materials Optimized for High-Performance Liquid Chromatography Separations”. *Accounts of Chemical Research* 40, 863–873, 2007. (see pp. 56, 58)

[183] G. Guiochon. “Monolithic columns in high-performance liquid chromatography”. *Journal of Chromatography A* 1168, 101–168, 2007. (see pp. 56, 58)

[184] C. P. Haas, T. Müllner, R. Kohns, D. Enke, and U. Tallarek. “High-performance monoliths in heterogeneous catalysis with single-phase liquid flow”. *Reaction Chemistry & Engineering* 2, 498–511, 2017. (see p. 56)

[185] M. D. Donohue and G. L. Aranovich. “Adsorption Hysteresis in Porous Solids”. *Journal of Colloid and Interface Science* 205, 121–130, 1998. (see pp. 57, 72)

[186] E. Kierlik, P. A. Monson, M. L. Rosinberg, L. Sarkisov, and G. Tarjus. “Capillary Condensation in Disordered Porous Materials: Hysteresis versus Equilibrium Behavior”. *Physical Review Letters* 87, 055701, 2001. (see pp. 57, 59, 72, 76)

[187] D. W. Siderius and L. D. Gelb. “Predicting Gas Adsorption in Complex Microporous and Mesoporous Materials Using a New Density Functional Theory of Finely Discretized Lattice Fluids”. *Langmuir* 25, 1296–1299, 2009. (see pp. 57, 72)

[188] G. Y. Gor, C. J. Rasmussen, and A. V. Neimark. “Capillary Condensation Hysteresis in Overlapping Spherical Pores:A Monte Carlo Simulation Study”. *Langmuir* 28, 12100–12107, 2012. (see p. 72)

[189] D. Schneider, R. Valiullin, and P. A. Monson. “Modeling the Influence of Side Stream and Ink Bottle Structures on Adsorption/Desorption Dynamics of Fluids in Long Pores”. *Langmuir* 31, 188–198, 2015. (see p. 72)

[190] L. Deliere, F. Villemot, D. Farrusseng, A. Galarneau, S. Topin, and B. Coasne. “Adsorption in heterogeneous porous media: Hierarchical and composite solids”. *Microporous and Mesoporous Materials* 229, 145–154, 2016. (see p. 72)

[191] D. W. Siderius, W. P. Krekelberg, W.-S. Chiang, V. K. Shen, and Y. Liu. “Quasi-Two-Dimensional Phase Transition of Methane Adsorbed in Cylindrical Silica Mesopores”. *Langmuir* 33, 14252–14262, 2017. (see p. 72)

[192] D. Schneider and R. Valiullin. “Capillary Condensation and Evaporation in Irregular Channels: Sorption Isotherm for Serially Connected Pore Model”. *The Journal of Physical Chemistry C* 123, 16239–16249, 2019. (see pp. 72, 77, 88)

[193] D. Zhao, J. Feng, Q. Huo, N. Melosh, G. H. Fredrickson, B. F. Chmelka, and G. D. Stucky. “Triblock Copolymer Syntheses of Mesoporous Silica with Periodic 50 to 300 Angstrom Pores”. *Science* 279, 548–552, 1998. (see p. 73)

[194] F. Kleitz, S. H. Choi, and R. Ryoo. “Cubic *Ia3d* large mesoporous silica : synthesis and replication to platinum nanowires , carbon nanorods and carbon nanotubes”. *Chemical Communications* 0, 2136–2137, 2003. (see pp. 73, 75)

[195] R. Hayes, A. Ahmed, T. Edge, and H. Zhang. “Core–shell particles: Preparation, fundamentals and applications in high performance liquid chromatography”. *Journal of Chromatography A* 1357, 36–52, 2014. (see pp. 73, 75)

[196] F. Kleitz, F. Bérubé, R. Guillet-Nicolas, C.-M. Yang, and M. Thommes. “Probing Adsorption, Pore Condensation, and Hysteresis Behavior of Pure Fluids in Three-Dimensional Cubic Mesoporous KIT-6 Silica”. *The Journal of Physical Chemistry C* 114, 9344–9355, 2010. (see p. 74)

[197] R. Guillet-Nicolas, F. Bérubé, M. Thommes, M. T. Janicke, and F. Kleitz. “Selectively Tuned Pore Condensation and Hysteresis Behavior in Mesoporous SBA-15 Silica: Correlating Material Synthesis to Advanced Gas Adsorption Analysis”. *The Journal of Physical Chemistry C* 121, 24505–24526, 2017. (see pp. 74, 80)

[198] T. Kjellman and V. Alfredsson. “The use of in situ and ex situ techniques for the study of the formation mechanism of mesoporous silica formed with non-ionic triblock copolymers”. *Chemical Society Reviews* 42, 3777–3791, 2013. (see p. 75)

[199] G. Guiochon and F. Gritti. “Shell particles, trials, tribulations and triumphs”. *Journal of Chromatography A* 1218, 1915–1938, 2011. (see p. 75)

[200] L. E. Blue and J. W. Jorgenson. “1.1 um superficially porous particles for liquid chromatography. Part I: Synthesis and particle structure characterization”. *Journal of Chromatography A* 1218, 7989–7995, 2011. (see p. 75)

[201] C. A. Schneider, W. S. Rasband, and K. W. Eliceiri. “NIH Image to ImageJ: 25 years of image analysis”. *Nature Methods* 9, 671–675, 2012. (see p. 77)

[202] M. W. Maddox, J. P. Olivier, and K. E. Gubbins. “Characterization of MCM-41 Using Molecular Simulation: Heterogeneity Effects”. *Langmuir* 13, 1737–1745, 1997. (see pp. 80, 81)

[203] A. Brodka and T. W. Zerda. “Molecular dynamics of SF6 in porous silica”. *The Journal of Chemical Physics* 95, 3710–3718, 1991. (see pp. 80, 81)

[204] M. Miyahara, H. Kanda, T. Yoshioka, and M. Okazaki. “Modeling Capillary Condensation in Cylindrical Nanopores: A Molecular Dynamics Study”. *Langmuir* 16, 4293–4299, 2000. (see pp. 80, 81)

[205] F. Cuadros, I. Cachadiña, and W. Ahumada. “Determination of Lennard-Jones interaction parameters using a new procedure”. *Molecular Engineering* 6, 319–325, 1996. (see pp. 80, 81)

[206] M. S. Ananth, K. E. Gubbins, and C. G. Gray. “Perturbation theory for equilibrium properties of molecular fluids”. *Molecular Physics* 28, 1005–1030, 1974. (see pp. 80, 81)

[207] P. I. Ravikovitch, A. Vishnyakov, R. Russo, and A. V. Neimark. “Unified Approach to Pore Size Characterization of Microporous Carbonaceous Materials from N_2 , Ar, and CO_2 Adsorption Isotherms”. *Langmuir* 16, 2311–2320, 2000. (see pp. 80, 81)

[208] F. Detcheverry, E. Kierlik, M. L. Rosinberg, and G. Tarjus. “The Physics of Capillary Condensation in Disordered Mesoporous Materials: A Unifying Theoretical Description”. *Adsorption* 11, 115–119, 2005. (see p. 83)

[209] C. J. Rasmussen, A. Vishnyakov, M. Thommes, B. M. Smarsly, F. Kleitz, and A. V. Neimark. “Cavitation in Metastable Liquid Nitrogen Confined to Nanoscale Pores”. *Langmuir* 26, 10147–10157, 2010. (see p. 84)

Contribution of authors

This work is a product of collective effort of several authors, whose contribution is explained below:

- Chapter 1
  Restoration of computer-generated packings, data processing and implementation of chord length distribution method were performed by me. Hydrodynamic dispersion simulations were performed by Dr. Dzmitry Hlushkou and me. Text preparation was performed by Prof. Dr. Ulrich Tallarek and subsequently edited by Dr. Dzmitry Hlushkou. The manuscript was submitted by Prof. Dr. Ulrich Tallarek.
- Chapter 2
  CLD analysis, finite-size analysis, geometric tortuorsity analysis were performed by Stefan-Johannes Reich. Simulations, branch tortuosity analysis, MMA analysis, data processing and implementation of skeleton dilation were performed by me. Dr. Daniela Stoeckel performed physical reconstruction and physisorption analysis. Dr. Christian Kübel assisted Dr. Daniela Stoeckel in preparation of physical reconstructions. The manuscript was written by Prof. Dr. Ulrich Tallarek and subsequently edited by Stefan-Johannes Reich, Dr. Dzmitry Hlushkou, Dr. Christian Kübel, Dr. Alexandra Höltzel and me. The manuscript was submitted by Prof. Dr. Ulrich Tallarek.
- Chapter 3
  Simulations were performed by Dr. Ashutosh Rathi. Initial data processing, statistical morphological analysis and image processing were performed by me. Local morphological analysis was performed by Dr. Dzmitry Hlushkou. Text preparation was performed by Prof. Dr. Ulrich Tallarek. The manuscript was subsequently edited by Dr. Dzmitry Hlushkou, Dr. Ashutosh Rathi, Prof. Dr. Peter A. Monson, Prof. Dr. David M. Ford and me. The manuscript was submitted by Prof. Dr. Ulrich Tallarek.
- Chapter 4
  Software for physisoprtion simulations and program for cavitation detection were developed by me. Simulations, data analysis, and initial text preparation were performed by me. Introduction was prepared by Dr. Dzmitry Hlushkou and Prof. Dr. Ulrich Tallarek. The manuscript was subsequently edited by Dr. Dzmitry Hlushkou, Prof. Dr. Ulrich Tallarek, Prof. Dr. Matthias Thommes, Prof. Dr. Peter A. Monson and me. The manuscript was submitted by Prof. Dr. Ulrich Tallarek.

Place, Date, Signature of Author _____

Place, Date, Signature of First Supervisor _____

Erklärung

Ich erkläre, dass eine Promotion noch an keiner anderen Hochschule als der Philipps-Universität Marburg, Fachbereich Chemie, versucht wurde.

Hiermit versichere ich, dass ich die vorliegende Dissertation

"Study of random porous morphologies by means of statistical analysis and computer simulations of fluid dynamics"

selbstständig, ohne unerlaubte Hilfe Dritter angefertigt und andere als die in der Dissertation angegebenen Hilfsmittel nicht benutzt habe. Alle Stellen, die wörtlich oder sinngemäß aus veröffentlichten oder unveröffentlichten Schriften entnommen sind, habe ich als solche kenntlich gemacht. Dritte waren an der inhaltlich-materiellen Erstellung der Dissertation nicht beteiligt; insbesondere habe ich hierfür nicht die Hilfe eines Promotionsberaters in Anspruch genommen. Kein Teil dieser Arbeit ist in einem anderen Promotions- oder Habilitationsverfahren verwendet worden. Mit dem Einsatz von Software zur Erkennung von Plagiaten bin ich einverstanden.

Ort, Datum, Unterschrift _____

Curriculum Vitae

Diese Seite enthält persönliche Daten.